Dissertation, Karlsruher Institut für Technologie (KIT)

Elementare Ermüdungsmechanismen in Metallen zur Lebensdauervorhersage mittels Versetzungsdynamiksimulation

Zur Erlangung des akademischen Grades
Doktor der Ingenieurwissenschaften
von der KIT-Fakultät für Maschinenbau
des Karlsruher Instituts für Technologie (KIT)

genehmigte
Dissertation
von

M.Sc. Taymour El-Achkar

Tag der mündlichen Prüfung: 27.05.2020
Hauptreferent: Prof. Dr. rer. nat. Peter Gumbsch
Korreferent: Prof. Dr. rer. nat. Christoph Eberl
Korreferent: Prof. Dr. mont. Christoph Kirchlechner

Acknowledgments

This thesis is the result of my work at the Institute for Applied Materials - Computational Materials Science at the Karlsruhe Institute of Technology (KIT) and was funded by the German Research Council (DFG) through its priority program '1466$^{\infty}$-*infinite life for cyclically loaded high performance materials*' under the contract numbers WE3544/3-2. This work would not have been possible without the support of many people, whom i would like to deeply thank.

Firstly, I would like to express my sincere gratitude to Prof. Dr. rer. nat. Peter Gumbsch for giving me the opportunity to pursue my doctoral studies at his department and for his support and invaluable discussions. His passion for material physics and eagerness to keenly understand the subject have been a source of inspiration and motivation throughout my thesis.

I would like to thank Prof. Dr. rer. nat. Chistoph Eberl and Prof. Dr. mont. Christoph Kirchlechner for agreeing to be referees of the doctoral examination committee.

My sincere thanks goes to Dr. Daniel Weygand for his guidance and continuous support of my research. His patience, motivation and feedback helped me in all the time of research and writing of this thesis. Discussions with him on the scientific and personal level have changed my ways of thinking.

I am grateful to Dr. Katrin Schulz and Dr. Severin Schmitt who introduced me to the institute and supervised my master's thesis.

A special thanks to colleagues who contributed to the thesis through ideas and discussions: Dr. Adam Hinkle, Dr. Johanna Gagel, Dr. Markus Stricker, Andreas Trenkle, Dr. Sirithanakorn and Patrick Ziemke.

I am very thankful to my office colleagues Dr. Adrien Gola, Dominik Horny, Daniel Kümmel, Dr. Markus Sudmanns and Kolja Zoller for a warm working atmosphere. Special thanks to Dr. Paul Schreiber for "climbing the ladder" together in afterwork sessions.

I would like to thank Julia Lehmann, Antje Dollmann and Christian Haug for discussions on experimental techniques.

I would also like to thank the system administrator Yiyue Li for her technical support. Many thanks to our secretary Andrea Doer for the administrative work.

I am grateful to my partner Agnieszka Fatyga for the support and patience she has provided during stressful times.

Finally, my thanks should be given to my parents Tanya and Ghazi El-Achkar for their emotional support throughout all my years abroad.

Karlsruhe, May 2020 Taymour El-Achkar

Abstract

The comprehension of mechanical fatigue in metals is crucial for the design of reliable and secure engineering components. The physical origin of fatigue crack initiation is mainly related to irreversible dislocation behavior. For the purpose of understanding the underlying physical mechanisms during fatigue, three-dimensional discrete dislocation dynamics simulations are performed during cyclic loading for *fcc*- and *bcc* metals.

In *fcc* surface grains, the grain geometry as well as crystallographic orientation are shown to play a major role in determining the nature and degree of microstructural irreversibility. Slip system activity is found to be determined by the Schmid-factor and the orientation of the crystal with respect to the free surface. In multislip loading conditions, pattern formation is shown to be controlled by sessile Lomer junctions that ensure the stability of the structure.
Upon decreasing the loading amplitude one order of magnitude below the persistent slip band threshold, a qualitatively distinct dislocation microstructure is observed though geometrical properties of dislocation dipoles and prismatic loops stay the same.

Bcc metals with a non-metallic inclusion are examined to determine the influence of different inclusion properties on the fatigue behavior. The effect of individual properties shows that the stress field due to the misfitting inclusion plays an important role in stabilizing the structure and involving all possible glide planes of a Burgers vector. The stress field due to the difference in elastic properties between the matrix and inclusion determines cross-slip and structure formation. When both properties are combined, then the relative magnitude of these stress fields locally controls the dislocation behavior.
Simulations of polycrystals reveal the effect of coarse-graining on dislocation density evolution and increase in irreversibility during cycling.

Kurzfassung

Für die Konstruktion von zuverlässigen und sicheren technischen Komponenten ist das Verständnis der mechanischen Ermüdung von Metallen von entscheidender Bedeutung. Der physikalische Ursprung der Ermüdungsrissinitiierung hängt hauptsächlich mit irreversiblem Versetzungsverhalten zusammen. Um die fundamentalen physikalischen Ermüdungsmechanismen zu verstehen, werden dreidimensionale diskrete Versetzungsdynamiksimulationen für *kfz*- und *krz*-Metalle unter zyklischer Belastung durchgeführt.

Bei der Bestimmung der Art und des Grades der mikrostrukturellen Irreversibilität spielen sowohl die Korngeometrie, als auch die kristallographische Orientierung der *kfz*-Oberflächenkörner eine wichtige Rolle. Es zeigt sich, dass die Aktivität des Gleitsystems durch den Schmid-Faktor und die Orientierung des Kristalls bezüglich der freien Oberfläche bestimmt wird. Bei hochsymmetrischen Belastungsbedingungen fällt auf, dass die Strukturbildung durch sesshafte Lomer-Reaktionen, die die Stabilität der Struktur gewährleisten, kontrolliert wird.
Nach Senkung der Belastungsamplitude um eine Größenordnung unter die Schwelle für die Bildung von persistenten Gleitbändern, wird eine qualitativ unterschiedlich ausgeprägte Versetzungsmikrostruktur beobachtet. Die geometrischen Eigenschaften von Versetzungsdipolen und prismatischen Versetzungsringen bleiben jedoch gleich.

Bei *krz*-Metallen mit einem nichtmetallischen Einschluss wird der Einfluss verschiedener Einschlusseigenschaften auf das Ermüdungsverhalten untersucht. Die Analysen zeigen, dass das Spannungsfeld aufgrund der Fehlpassung des Einschlusses eine wichtige Rolle bei der Stabilisierung der Struktur und der Einbeziehung aller möglichen Gleitebenen eines Burgersvektors spielt. Das Spannungsfeld aufgrund der unterschiedlichen elastischen Eigenschaften zwischen Matrix und Einschluss bestimmt das Quergleitverhalten und die Strukturbildung. Wenn beide Eigenschaften kombiniert werden, steuert die relative Größe dieser Spannungsfelder lokal das Versetzungsverhalten.
Simulationen von Polykristallen zeigen den Einfluss der Grobkörnung auf die Entwicklung der Versetzungsdichte und die Zunahme der Irreversibilität.

Publications

T. El-Achkar and D. Weygand. Discrete dislocation dynamics study of dislocation microstructure during cyclic loading. In H.-J. Christ, editor, *Fatigue of Materials at Very High Numbers of Loading Cycles*. Springer Verlag, 2018.

T. El-Achkar and D. Weygand. Analysis of dislocation microstructure characteristics of surface grains under cyclic loading by discrete dislocation dynamics. *Modelling and Simulation in Materials Science and Engineering*, 27(5):055004, 2019.

Contents

Symbols and Abbreviations

The following notation for vector quantities will be used: a vector $\boldsymbol{v}$ is defined as $\boldsymbol{v} = v\boldsymbol{e}_{\boldsymbol{v}}$, where v is the norm of the vector and $\boldsymbol{e}_{\boldsymbol{v}}$ is the unit direction vector. The only exceptions are normal vectors $\boldsymbol{n}$ which are normalized unit vectors.

Abbreviations

bcc	Body centered cubic
BVP	Boundary value problem
DDD	Discrete Dislocation Dynamics
EBSD	Electron backscatter diffraction
EGM	Essmann-Gösele-Mughrabi Model
fcc	Face centered cubic
FGA	Fine Granular Area
FR	Frank-Read
HCF	High Cycle Fatigue
LCF	Low Cycle Fatigue
MD	Molecular Dynamics
MEMS	Microelectromechanical systems
PSB	Persistent slip band
RMS	Root Mean Square
TEM	Transmission Electron Microscope
VHCF	Very High Cycle Fatigue

Symbols

$\boldsymbol{Q}$	Point cloud matrix of a component
A	Empirical parameter used for cell size
A_{enclosed}	Enclosed area of prismatic loop
A_{shell}	Area of shells used for correlation function
A_{swept}	Swept area of a dislocation
α_{cs}	Angle to determine if a segment is of screw type while testing for cross-slip
α_M	Parameter in $\sqrt{area}$ fatigue life prediction formula
$\boldsymbol{\alpha}$	Average position of point cloud
b_q	Fatigue strength exponent
K_p	Bulk modulus of the precipitate
$\boldsymbol{b}$	Burgers vector
c	Fatigue ductility exponent
c_1	Fitting coefficient in exponential distribution
c_2	Fitting coefficient in exponential distribution
C_{M_1}	Parameter in $\sqrt{area}$ fatigue life prediction formula
C_{M_2}	Parameter in maximum stress intensity factor
$\boldsymbol{x}_{\text{centroid}}$	Grain centroid position
χ_c	Closed component of graph
χ	Graph component
$\boldsymbol{R}$	Correlation matrix
g_{2d}	Two-point correlaction function
$\boldsymbol{L}_{AB}$	Coupling matrix
$\boldsymbol{C}$	Covariance matrix
d_{centroid_i}	Distance from grain boundary i to grain centroid

d_{gbs}	Minimum safe distance from grain boundary
d_{grain}	Grain diameter
d_{out}	Projection distance along $\boldsymbol{t}$ out of the precipitate
d_{sph}	Minimum safe distance from precipitate
$\boldsymbol{u}$	Displacement vector
D	Drag coefficient
e^*	Misfit strain
e_C^*	Eshelby misfit strain
ϵ	Very small number that is negligible compared to unity
$\varepsilon_{\mathrm{pl,cum}}$	Cumulative plastic strain
$\varepsilon_{\mathrm{pl,irre}}$	Irreversible plastic strain
$\Delta\varepsilon_{\mathrm{pl,loc}}/2$	Local axial plastic strain amplitude
$\varepsilon_{\mathrm{pl}}$	Plastic strain
$\Delta\varepsilon_{\mathrm{pl}}/2$	Plastic strain amplitude
$\varepsilon_{\mathrm{pl,vM}}$	Von Mises plastic strain
ε_f'	Fatigue ductility coefficient
$\boldsymbol{f}_{\mathrm{pk}}$	Peach-Köhler force
$\boldsymbol{f}_{\mathrm{pk}}^{\boldsymbol{g}}$	Glide component of the Peach-Köhler force
$\boldsymbol{f}_{\mathrm{tot}}$	Sum of nodal forces of a segment
$\gamma_{\mathrm{pl,loc}}$	Resolved shear strain amplitude
$\boldsymbol{n}_{\mathrm{gp}}$	Glide plane normal vector
G	Graph
U	Edge in graph
V	Node in graph
h	Dislocation dipole height
h_{crit}	Critical height to destabilize a dislocation dipole

$\tilde{h}$	Distance along which surface roughness is measured
H	Heaviside function
R_H	Hole radius
$K_{\max}$	Maximum stress intensity factor
K_{th}	Threshold stress intensity factor
$L_{\min}$	Minimum length of a dislocation dipole
$L_{\min,\text{cs}}$	Minimum length of cross-slip sector
$l_{\min,\text{seg}}$	Minimum segment length
L_{sector}	Length of the screw sector used for cross-slip
l_{segment}	Segment length
λ	Parameter of a straight line equation
λ_s	Linear intercept cell size
$\boldsymbol{t}$	dislocation line vector
m_0	Mass per unit length of a dislocation
$\boldsymbol{M}_{AB}$	Mass matrix
$\boldsymbol{\sigma}^{\mathbf{el}}$	Modulus-induced stress field
N	Number of elements in a list
N_A	Number of total discretization nodes
N_B	Number of neighboring nodes
N_{cycles}	Number of cycles
N_f	Number of load cycles to failure
N_{inter}	Number of intersection points of cuts used for correlation function
N_L	Number of Lomer junctions
$\boldsymbol{V}$	Nodal velocity
$\boldsymbol{P'}$	Intersection point of lines
p	Irreversibility factor

$\boldsymbol{P}$	Intersection point of grain boundaries
p_{shape}	Shape factor of prismatic loop
T	Period
$\boldsymbol{x^n}$	Position vector at time step n
$\boldsymbol{x^{n+1}}$	Position vector at time step $n+1$
x_{ref_i}	Reference position on plane i
R_p	Precipitate radius
$\boldsymbol{r}_{\text{gp}}$	Projection of $\boldsymbol{r}$ along the glide plane
R_σ	Stress ratio
$\boldsymbol{r}$	Distance vector from precipitate center
$\boldsymbol{b_{\text{react}}}$	A reaction's Burgers vector
ρ_{around}	Dislocation density around Lomer junctions
ρ_{corr}	Normalization density of correlation function
$\boldsymbol{s}$	Vector perpendicular to the line direction and glide plane normal
M	Sachs factor
S	Schmid factor
S'	Modified Schmid factor
$\mathcal{N}$	Shape function
μ	Shear modulus
$\boldsymbol{\sigma^{\text{ana}}}$	Analytical stress field
$\boldsymbol{\sigma^*}$	Misfit stress
σ_w	Fatigue limit
$\boldsymbol{\sigma}$	Cauchy stress tensor
σ_s	Back stress
σ'_f	Fatigue strength coefficient
$\hat{\boldsymbol{\sigma}}$	Correction stress field of a dislocation due to boundary conditions

σ_s	Saturation stress
$\tilde{\boldsymbol{\sigma}}$	Analytical stress field of a dislocation in an infinite medium
Υ	Standard deviation
$\boldsymbol{K}_{AB}$	Stiffness matrix
$\boldsymbol{n}_{\text{surf}}$	Surface normal vector
τ	Resolved shear stress
τ_{cs}	Resolved shear stress on the cross-slip plane
τ'	Friction stress applied to screw segments
τ_{primary}	Resolved shear stress on the primary plane
τ_{tot}	Resolved shear stress from both nodes of a segment
t	Time
n	Time step
$\boldsymbol{T}$	Traction vector
U_{perim}	Perimeter of prismatic loop
V_{av}	Averaging volume for plastic strain
$\boldsymbol{v}$	Velocity
w_{screw}	Weighting function for screw dislocations
w_{ij}	Distance-dependent weighting function
$\boldsymbol{x}_{\text{center}}$	Position of the precipitate center
y_s	Annihilation distance of screw dislocations
E	Young's modulus

1. Fatigue of metals: A brief introduction

Numerous engineering components present in everyday applications such as automobiles, aircraft, conveyor systems, microelectromechanical systems (MEMS), etc. are subjected to alternating load on quotidian basis. Depending on the area of application, they are required to reliably perform over time scales of several days or even hundreds of years. If the loads experienced during operating exceed foreseen thresholds, then the material may '*tire*' and suffer so-called fatigue failure. Although the number of fatigue failures relative to successfully operating components is very small, the associated material cost is immense (Stephens et al., 2000). Indeed, fatigue failures are the most frequent of all mechanical failures (at least 50%) and occur mainly unexpectedly (Stephens et al., 2000).

Unfortunately, incentives to understand fatigue failure have been mainly driven throughout history by tragic events. For instance, one of the earliest accidents in 1842 was a front axle failure of a locomotive near Versailles, France leading to many fatalities (Suresh, 1998). Even after almost one hundred years, several fatigue-related, catastrophic failures occurred in *Comet* passenger airplanes due to rivet holes (stress concentration) in the cabins, which were frequently pressurized and depressurized upon operation (Suresh, 1998).

Therefore, the comprehension of physical mechanisms responsible for fatigue failure is crucial for the reliability of components and the safety of mankind. The following two sections describe the development of the fatigue research field[1].

1.1 Low- and High Cycle Fatigue

Experimental findings The fatigue research field has been an active area of scientific and engineering investigation for over 150 years, albeit mostly experimental. The

[1] For a broader overview, the following literature is recommended Suresh (1998), Mughrabi (2009) and Hong und Sun (2017).

first systematic work was conducted by Wöhler (1870) who recognized that fatigue strength is lower than static strength and also introduced the concept of an endurance limit. The latter concept refers to a stress amplitude for a number of cycles, traditionally 10^7, below which a material can have infinite lifetime. Accordingly, the most frequently used diagram in fatigue analysis is the S-N- or Wöhler curve, which represents the number of cycles to failure N_f versus the stress amplitude. It is divided into two regimes: Low Cycle Fatigue (LCF) for $N_f < 10^4$ and High Cycle Fatigue (HCF) for $10^4 < N_f < 10^7$.

Not until Ewing und Rosenhain (1900) and Ewing und Humfrey (1903), fatigue cracks were firstly associated with slip bands along active slip planes. It became clear that fatigue damage at the surface is a consequence of irreversible plastic strain. Basquin (1910) showed that in a log-log S-N curve a linear relationship between the stress amplitude and number of cycles to fail exists. A similar approach, however for the plastic strain, was proposed by Manson (1954) and Coffin Jr (1954) who developed an empirical relationship between the plastic strain amplitude and the number of load reversals to failure. The importance of plastic strain was, hence, recognized. Morrow (1965) demonstrated that the total fatigue lifetime is a combination of the Manson-Coffin law in LCF and Basquin relationship in HCF: The total strain amplitude $\Delta\varepsilon_{\mathrm{tot}}/2$ in a total strain controlled test is the sum of elastic- and plastic strain amplitudes $\Delta\varepsilon_{\mathrm{el}}/2$ and $\Delta\varepsilon_{\mathrm{pl}}/2$ respectively,

$$\begin{aligned}\frac{\Delta\varepsilon_{\mathrm{tot}}}{2} &= \frac{\Delta\varepsilon_{\mathrm{el}}}{2} + \frac{\Delta\varepsilon_{\mathrm{pl}}}{2} \\ &= \underbrace{\frac{\sigma'_f}{E}(2N_f)^{b_q}}_{\text{Basquin}} + \underbrace{\varepsilon'_f(2N_f)^c}_{\text{Manson-Coffin}}\end{aligned} \tag{1.1}$$

where b_q and σ'_f are the fatigue strength exponent and coefficient respectively, c and ε'_f are the fatigue ductility exponent and coefficient respectively and $2N_f$ the number of load reversals to failure. The idea is that the total fatigue life is controlled by ductility in the LCF regime (Manson-Coffin) and rupture strength in the HCF regime (Basquin). The transition life $(2N_f)_t = (\varepsilon'_f E/\sigma'_f)^{1/(b_q-c)}$ is the intersection of both parts. The above models are simple, nevertheless still fundamental to design reliable components.

With the invention of electron microscopy, investigations of microstructural evolution, especially for well-annealed face centered cubic (*fcc*) single crystals (most extensively copper), during cycling loading became common practice. Thompson et al. (1956)

introduced the term '*persistent slip bands*' (PSBs) after showing that slip bands reappeared at the same position even after material removal. Figure 1.1(a) is a schematic cyclic saturation stress-strain curve, which is representative of a single crystal behavior under cyclic loading. Each point represents the saturation resolved shear stress τ_s for an independent plastic strain controlled experiment. Depending

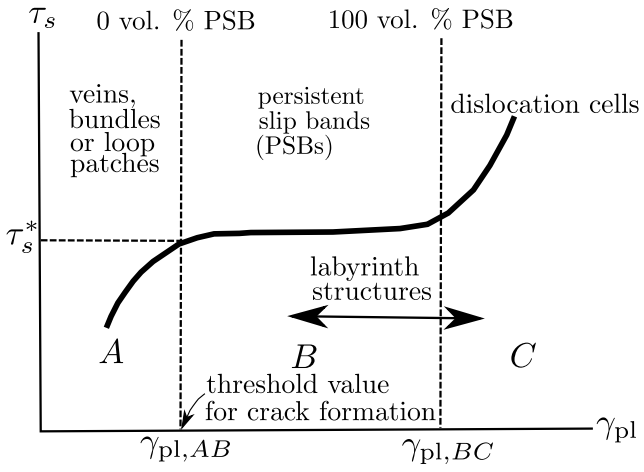

(a)

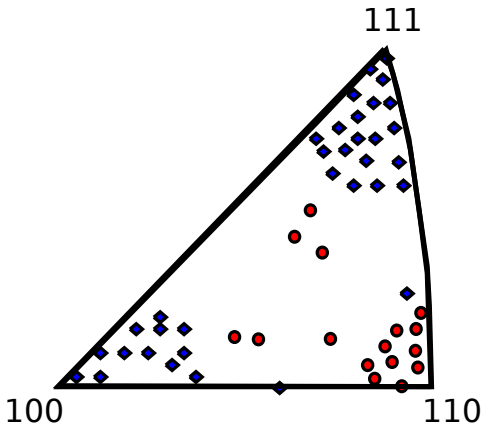

(b)

Figure 1.1: (a) A schematic cyclic stress-strain curve partitioned into different regions with the representative dislocation structures (Suresh, 1998). (b) Inverse pole figure of Ni indicating dislocation pattern dependence on the tensile-axis orientation (after Sauzay et al. (2010)). Blue rhombuses represent cells/labyrinths and red circles PSBs. Reprinted with permission.

on the plastic strain amplitude $\gamma_{\mathrm{pl}} = \Delta\varepsilon_{\mathrm{pl}}/2$, the curve can be partitioned into different regimes, in which dislocation microstructures vary. At small plastic strain amplitudes ($\gamma_{\mathrm{pl}} < \gamma_{\mathrm{pl},AB} \approx 10^{-4}$), a hardening behavior associated with primary dislocations which form so-called veins is observed (figures 1.2(a) and 1.2(b)). The vein structure consists of edge dislocation bundles of opposite signs, which have a

zero net Burgers vector and thus produce no long-range internal stresses (Mughrabi, 1979).

The veins consist primarily of prismatic loops, which were found to be formed by cross-glide processes (Fourie und Murphy, 1962, Gilman, 1964). The early saturation in zone A is attributed to a reversible *flip-flop* mechanism of prismatic loops (Feltner, 1965). For a larger plastic strain amplitude $\gamma_{\mathrm{pl},AB} < \gamma_{\mathrm{pl}} < \gamma_{\mathrm{pl},BC}$, the vein structures cannot accommodate the strain, so the microstructure commences to form PSBs. In the primary slip planes, PSBs show a wall- and channel-like structure, whereas in {112} cross sections prominent ladder-like dislocations are seen (figures 1.2(c) and 1.2(d)). Holzwarth und Essmann (1993) demonstrated how the PSB structure arises from the dislocation-weak zones of the matrix to form ladders. Winter (1980) developed a two-phase model that suggests that plastic strain accommodation increases linearly within the PSB to reach 100% for $\gamma_{\mathrm{pl},BC}$. The argument is in agreement with previous observations showing that the PSB-phase is softer than the matrix (veins) and that deformation in the plateau regime is carried mainly by PSBs (Broom und Ham, 1959). The plateau regime has been attributed to an equilibrium between the multiplication and annihilation of dislocations (Essmann und Mughrabi, 1979). Mughrabi (1983) used a *composite* model to justify the plateau nature of this domain, which shows that stresses in the walls are higher than the applied stress and vice versa in the channels.

For higher strain amplitudes, activation of secondary slip leads to the formation of labyrinth or cell structures (figures 1.2(e) and 1.2(f)). The cell structure seen in figure 1.2(f) is a consequence of a transformation of the PSB ladders into cells. Such structure is not to be confused with cells developing in the primary glide plane, for instance as in Lukáš et al. (1968).

The structures shown above are found in materials, in which dislocations can easily cross-slip. On the other hand, materials, such as alloys with high yield stresses or short range order due to strong solid solution hardening, may exhibit a difficulty in cross-slip and result in rather planar structures (Mughrabi, 2010).

The behavior of polycrystalline materials is more complex and is summarized in Suresh (1998). Due to defects in polycrystals such as inclusions, grain boundaries, etc. the overall behavior may significantly differ from that of single crystals. The incompatibility of strains between neighboring grains yields multislip loading conditions. Thus favorably oriented grains for multislip in fine-grained polycrystals can be directly compared to their corresponding single crystals. For such loading conditions, figure 1.1(b) shows the orientation dependence of dislocation structures in Ni in an

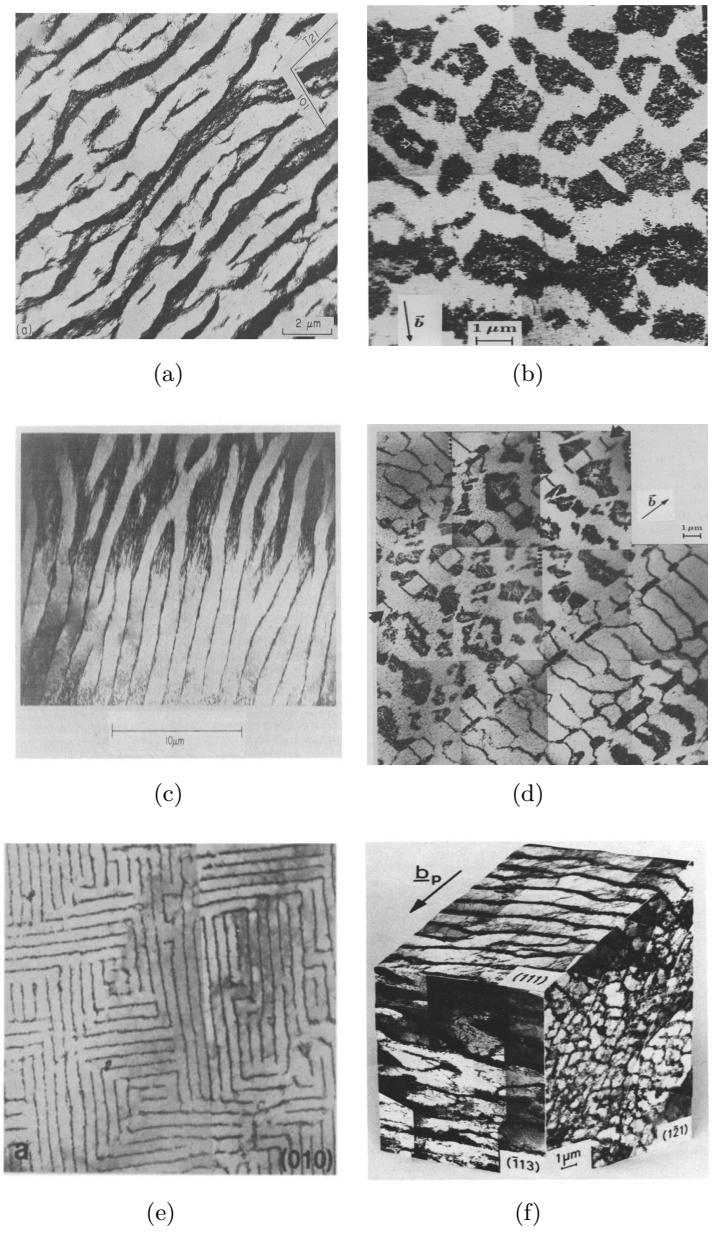

(a) (b)

(c) (d)

(e) (f)

Figure 1.2: TEM images from different stages of fatigued dislocation microstructure of single crystal copper: (a) primary {111}-type slip plane showing vein-structure (matrix) fatigued to saturation (Basinski et al., 1980). (b) A {112}-type section in saturation state showing loop patches with centers free of dislocations (Holzwarth und Essmann, 1993). (c) Primary slip plane showing PSB wall structure in the lower part (Winter, 1980). (d) Ladder structures ({112}-type cross section) observed at $\Delta\varepsilon_{\mathrm{pl}}/2 = 0.4\%$ showing PSBs appearing in vein-centers with small dislocation densities (Holzwarth und Essmann, 1993). (e) (010) cross section showing a labyrinth structure with (100)- and (001) walls for $\Delta\varepsilon_{\mathrm{pl}}/2 = 0.4\%$ (Jin und Winter, 1984b). (f) Three-dimensional assembled TEM images showing cell structure at $\Delta\varepsilon_{\mathrm{pl}}/2 = 1.45\%$ (Laird et al., 1986). All figures are reprinted with permission.

inverse pole figure. The figure shows that grain orientations around [100] and [111] exhibit cellular or labyrinth structures, whereas [110] orientations predominantly exhibit ladder structures. The PSBs are similar to the ones observed in single crystals and have been reported to also be found in the bulk of the material.

The surface damage mechanism, which is related to the formation of surface extrusions and intrusions, has been described by several authors. The most prominent is the Essmann-Gösele-Mughrabi (EGM) Model (Essmann et al., 1981, Mughrabi et al., 1983, Differt et al., 1986), which relies on the idea that vacancy dipoles' annihilation is the source of plastic irreversibility. The predominance of vacancy dipoles during fatigue has been reported by Polák (1970) and Antonopoulos et al. (1976). If located at a smaller distance than ≈ 50 nm, vacancy dipoles can annihilate and generate vacancy point defects, thus a net extrusion appearance is expected (Mughrabi, 2009). Thus, the remaining interstitial dipoles that form at the PSB-interface can glide out and leave static extrusions (Mughrabi et al., 1983). The random irreversible forward and backward motion of screw dislocations causes a superposed gradual roughening of the developed static extrusions. Thus, the surface topology contains several stress raisers in form of peaks and valleys that can lead to a surface crack.

Micromechanical fatigue simulations The persistent desire to miniaturize components necessitates controlling microstructural properties, especially when sample sizes are on the level of micromechanical defects (Arzt, 1998). Prolonged fatigue life in high strength steels has been observed when specimen sizes decrease (Furuya, 2008). Because of the small component length scales, physical simulation tools and models, which are computationally expensive for large volumes, can be effectively deployed to aid the understanding of fatigue mechanics.

Since dislocation structure formation is controlled by geometrical dislocation arrangements due to elastic interactions between dislocations, the meso-scale simulation method known as Discrete Dislocation Dynamics (DDD) is able to provide detailed insight into the structure formation mechanisms. The role of microstructural parameters, e.g. grain shape and orientation, on structure correlations is accessible. Several groups have used DDD under cyclic loading to explore the mechanisms leading to irreversible dislocation structure formation[2]. A detailed analysis of single- and double slip loading conditions was given in Déprés et al. (2004, 2006). It was shown that an initial single Frank–Read source can yield, due to annihilation and cross-slip processes, a dipolar dislocation microstructure which shows good agreement with experiments. It was found that slip band spacing was inversely proportional to the

[2] The above mentioned vacancy generation mechanism due to climb is ignored in these simulations

square of the slip band thickness. The authors stressed the role of cross-slip for strain localization and showed that double slip conditions lead to more damage than single slip. Based on statistical distribution of dipole heights, Déprés et al. (2008) derived a model which accurately reproduces precisely an experimental hysteresis loop. Recently it was found that dislocations arising from a single source and trapped within a stress gradient can lead to irreversible macroscopic plastic deformation under cyclic bending with very little dislocation storage (Stricker et al., 2017). Prismatic loop generation and interaction mechanisms were studied in Erel et al. (2017). The authors presented two different transport mechanisms of prismatic loops. If the loops are small in size, then they are driven by stress gradients, whereas long dipoles, e.g. in PSBs, move primarily due to a strong attraction of mobile screw dislocations. For multislip orientations, the effects of the initial dislocation density and crystal size on surface roughness and dislocation cell size were investigated in Hussein und El-Awady (2016a,b). The cell size and wall thickness showed an increase upon increasing the crystal size, whereas early surface slip localization was observed for rather small crystals. Several measures such as the Hausdorff dimension for surface analysis and information entropy for pattern analysis were also used. The role of double cross-slip in the development and evolution of slip bands was emphasized.

Another approach is dislocation-based models, which are widely used by experimentalists. A prominent example is the Tanaka und Mura (1981) model, where the development of extrusions and intrusions is confined within two parallel layers of glide planes representing a PSB. The source of irreversibility in this model is the different back stress level caused by one layer on another enabling an increase of dislocation pileups during cycling.

1.2 Very High Cycle Fatigue

The PSB threshold has simply been considered hitherto as the fatigue limit. However, unexpected failures, such as the railway accident of Eschede (Esslinger et al., 2004), for amplitudes below the traditional endurance limit put the latter concept into doubt. Since many modern applications (bearings, train-axles, etc.) are reliably required to endure up to 10^{10} cycles, a surge of interest in the Very High Cycle Fatigue (VHCF) (or Ultra High Cycle Fatigue (Mughrabi, 1999)) behavior for cycles above 10^8 emerged. In particular, the development of modern fatigue testing machinery which run at ultrasonic frequencies (up to 20 KHz) enables VHCF-experiments

to be completed in less than a day (Willertz, 1980, Bathias, 1999, Eberl, 2005, Stanzl-Tschegg et al., 2007, Straub et al., 2015, Straub, 2016).

In the VHCF-regime, crack initiation rather than crack propagation has been shown to be the life controlling mechanism (Mughrabi, 1999, Hong und Sun, 2017) and governs 95-99% of the fatigue lifetime (Murakami et al., 2000a, Tanaka und Akiniwa, 2002, Hong et al., 2014). Since the loading amplitudes are not enough to form PSBs, the dislocation microstructure is primarily that of stage I, i.e. dislocation bundles and veins.

Mughrabi (1999) makes the distinction between the behavior of single-phase ductile *fcc* metals (type I materials) and high strength steels containing inclusions (type II materials), which will be briefly outlined below.

Type I materials A multi-stage S-N curve for type I materials in the VHCF is postulated by Mughrabi (1999). The first range is the LCF-regime described by the Manson-Coffin law, followed by a plateau related to the PSB threshold in the HCF-regime ($\Delta\varepsilon_{\mathrm{pl}}/2 = 2.5 \times 10^{-5}$ for copper). Below the latter amplitude and at higher cycles is the transition zone to VHCF. Since Lukáš et al. (1974) showed that the Manson-Coffin law is applicable to HCF by mutual transformation of stress- and plastic strain amplitude, Mughrabi (1999) developed a similar law for VHCF which reads

$$N_f^{c+1} p = \frac{\varepsilon_{\mathrm{pl,irre,f}}}{4\varepsilon_f' 2^c} = \mathrm{const} \tag{1.2}$$

where $\varepsilon_{\mathrm{pl,irre,f}}$ is the cumulative irreversible plastic strain at failure and p a factor describing the degree of irreversibility of a system (Essmann, 1982). The fourth range in the S-N curve is the irreversibility threshold ($\Delta\varepsilon_{\mathrm{pl}}/2 \approx 10^{-5}$ for copper).

A suggested mechanism behind crack initiation is related to the accumulation of small irreversible plastic slip that leads gradually to an increase in surface roughness. After reaching a certain threshold, evolved surface valleys may act as stress raiser and give rise to embryonic PSBs. With increasing number of cycles, strain becomes localized in the PSBs, and the latter extends deeper into the volume yielding stage I crack initiation (Mughrabi, 2006). Indeed, polycrystalline copper subjected to 10^{10} cycles with amplitudes somewhat below conventional PSB threshold show slip bands at the surface accompanied with stage I shear cracks (Weidner et al., 2010).

Type II materials Most of the early studies in the VHCF-regime were performed on high strength steels with inclusions (Murakami, 1994, Murakami et al., 1998, Bathias, 1999). It was shown that the S-N curve exhibits a two-fold behavior (Nishijima und Kanazawa, 1999, Sakai et al., 2000), where surface fatigue failures govern LCF- and HCF domains and internal failures at subsurface inclusions the VHCF-regime. The fracture surfaces all show a similar morphology: Around the inclusion is a relatively small, rough and bright area of several microns, called the Fine Granular Area (FGA) (Sakai et al., 2000), surrounded by a large (hundreds of microns) and flat region labeled as the '*fish-eye*' region (Murakami, 1994). The term FGA is given different names in the literature such as Optical Dark Area (Murakami et al., 2000a,b) or Granular Bright Facet (Shiozawa et al., 2001). As a matter of fact, several groups have shown using selected area electron diffraction that in the FGA, a local grain refinement takes place (Grad et al., 2012, Hong et al., 2016). The size of the FGA has been studied and shown to be inversely proportional to the applied stress (Hong und Sun, 2017). The overall crack initiation time is found to be mostly consumed in FGA development (Hong et al., 2014).

Understanding the underlying mechanisms in FGA evolution is crucial to obstruct fatigue failure in type II materials. Several models have been developed in this regard:

- Murakami et al. (2000a,b) explain the formation of the FGA as a result of hydrogen entrapment by inclusions yielding steady crack growth and leaving a rough surface behind. The authors predict fatigue failure in terms of the inclusion geometry and matrix hardness (stress ratio $R_\sigma \neq 1$):

$$\sigma_w = \frac{C_{\mathrm{M}_1}(HV + 120)}{(\sqrt{area})^{\frac{1}{6}}} \left(\frac{1 - R_\sigma}{2}\right)^{\alpha_{\mathrm{M}}} \tag{1.3}$$

  where σ_w is the fatigue stress limit, $area$ the projection area of the inclusion onto a plane perpendicular to the loading axis, C_{M_1} a parameter which accounts for inclusion location (surface, subsurface or interior), HV Vicker's hardness of the matrix, and α_{M} a parameter depending on HV.

  Fatigue fracture has been described in terms of linear elastic fracture mechanics: If the maximum stress intensity factor $K_{\max} = C_{\mathrm{M}_2}\sigma_0\sqrt{\pi\sqrt{area}}$ exceeds a threshold stress intensity factor K_{th}, typically in the range of $4\,\mathrm{MPa}\sqrt{\mathrm{m}} < K_{\mathrm{th}} < 6\,\mathrm{MPa}\sqrt{\mathrm{m}}$ (Shiozawa und Lu, 2002), then crack initiation is possible (Grad et al., 2012). The parameters σ_0 and C_{M_2} are respectively the maximum tensile stress and a parameter similar to C_{M_1} related to the location of the inclusion. It turns out that this assumption is only valid when

the parameter *area* is taken as the area of the inclusion and the FGA combined, which makes the latter region of even more importance.

- Shiozawa et al. (2006) suggest that in high strength steels rich in carbon, the FGA forms due to decohesion of spherical carbides from the matrix.
- Local grain refinement in the FGA is attributed to the formation of dislocation cells by Grad et al. (2012). Due to the grain refinement, K_{th} decreases locally and gets exceeded by K_{max} leading to crack initiation in the FGA. Indeed, Chai et al. (2012) observe local plastic deformation around inclusions and identify cell structures in TEM images.

2. Simulation- and analysis methods

2.1 Discrete Dislocation Dynamics

Discrete Dislocation Dynamics (DDD) is a mesoscale simulation method based on a discrete representation of dislocations. Thus, plasticity, which is a direct consequence of dislocation motion, can be studied thoroughly without the necessity to introduce phenomenological flow rules usually present in continuum plasticity models (Simo und Hughes, 2006). In contrast to molecular dynamics (MD), where dislocations arise naturally in a strained crystal, dislocations need to be introduced into the simulation domain. While MD is limited to small- system sizes (nm) and time scales (ps), DDD systems can be several microns large and in the microsecond range. This allows to study mechanisms of complex dislocation networks and dynamical problems such as early stages of fatigue. Several authors developed DDD codes during the last 30 years (Kubin und Canova, 1992, Van der Giessen und Needleman, 1995, Fivel et al., 1996, Weygand et al., 2002, Arsenlis et al., 2007). The simulations in this work were performed using the DDD-framework Weygand et al. (2001, 2002), Weygand und Gumbsch (2005). Only a brief summary is given here.

Dislocations are treated as line singularities embedded into an elastic continuum. The curved lines are approximated using straight segments connected by nodes with assigned properties such as the Burgers vector $\boldsymbol{b}$ and line direction $\boldsymbol{t}$. The habitat of dislocations is the crystal system which comprises a set of discrete slip planes fixed at a constant distance from each other. Dislocation kinetics are described by a semi empirical Newtonian-type equation

$$m_0 \frac{\partial \boldsymbol{v}}{\partial t} + D\boldsymbol{v} = \boldsymbol{f}^{\boldsymbol{g}}_{\mathrm{pk}} \tag{2.1}$$

where m_0 is the effective mass per unit length of a dislocation, $\boldsymbol{v}$ the dislocation velocity, D a material specific drag coefficient and $\boldsymbol{f}_{\mathrm{pk}}$ the glide component of the Peach-Köhler force at a specific location $\boldsymbol{l}$ along the dislocation line. Both m_0

and D are atomic-scale properties which are parameterized using MD simulations (Bitzek und Gumbsch, 2005). The Peach-Köhler force is calculated according to

$$\boldsymbol{f}_{\mathrm{pk}} = \boldsymbol{\sigma b} \times \boldsymbol{e_t} \tag{2.2}$$

where $\boldsymbol{\sigma}$ is the total stress and $\boldsymbol{e_t}$ the normalized line direction. The glide component of the Peach-Köhler force is calculated according to

$$\begin{aligned} \boldsymbol{f}^{\boldsymbol{g}}_{\mathrm{pk}} &= (\boldsymbol{f}_{\mathrm{pk}} \cdot \boldsymbol{e_s})\boldsymbol{e_s} \\ &= (\boldsymbol{\sigma b} \cdot \boldsymbol{n})\boldsymbol{e_s} \end{aligned} \tag{2.3}$$

where $\boldsymbol{n}$ is the normalized glide plane normal and $\boldsymbol{e_s} = \boldsymbol{n} \times \boldsymbol{e_t}$ a unit vector perpendicular to the line segment and located in the glide plane. The resolved shear stress in the glide plane is $\tau = ||\boldsymbol{f}^{\boldsymbol{g}}_{\mathrm{pk}}||/b$ with $b = ||\boldsymbol{b}||$.

For each dislocation line, a one-dimensional FEM approximation is applied (Weygand et al., 2002, Bitzek et al., 2004) and briefly explained in the following. The principle of virtual work is applied to equation 2.1 which yields an equation for the rate of energy dissipation due to dislocation glide

$$m_0 \int \dot{\boldsymbol{v}}(l) \cdot \, \delta \boldsymbol{v}(l)\, dl + D \int \boldsymbol{v}(l) \cdot \, \delta \boldsymbol{v}(l)\, dl - \int \boldsymbol{f}^{\boldsymbol{g}}_{\mathbf{pk}}(l) \cdot \, \delta \boldsymbol{v}(l)\, dl = 0 \tag{2.4}$$

where $\delta \boldsymbol{v}(l)$ is the virtual velocity of the dislocation at position l along the dislocation loop. The local velocity $\boldsymbol{v}$ is interpolated using linear shape functions $\mathcal{N}(l)$ between nodal velocities $\boldsymbol{V}_A$

$$\boldsymbol{v}(l) = \sum_{A=1}^{N_A} \mathcal{N}_A(l) \boldsymbol{V}_A \tag{2.5}$$

where N_A is the total number of nodes. The same interpolation is also used for the acceleration $\dot{\boldsymbol{v}}$ and virtual velocity $\delta \boldsymbol{v}$. Substituting equation 2.5 into equation 2.4 yields

$$\begin{aligned} \sum_{A=1}^{N_A} \Big[m_0 \sum_{B=1}^{N_B} \dot{\boldsymbol{V}}_B \underbrace{\int \mathcal{N}_A(l)\, \mathcal{N}_B(l)\, dl}_{\boldsymbol{L}_{AB}} + D \sum_{B=1}^{N_B} \boldsymbol{V}_B \int \mathcal{N}_A(l)\, \mathcal{N}_B(l)\, dl \\ - \underbrace{\int \mathcal{N}_A(l)\, \boldsymbol{f}^{\boldsymbol{g}}_{\mathbf{pk}}(l)\, dl}_{\boldsymbol{f}_A} \Big] \cdot \delta \boldsymbol{V}_A = 0 \end{aligned} \tag{2.6}$$

where N_B is the total number of neighboring nodes of node A and $\boldsymbol{L}_{AB}$ is a matrix containing coupling information about segment lengths of neighboring nodes. The nodal force of node A reads

$$\boldsymbol{f}_A = \sum_{B=1}^{N_B} \boldsymbol{f}_{AB} = \int \mathcal{N}_A(l)\, \boldsymbol{f}^{\boldsymbol{g}}_{\mathbf{pk}}(l)\, dl \tag{2.7}$$

which is the sum of nodal forces $\boldsymbol{f}_{AB}$ of all segments AB connected to node A. Requiring equation 2.6 to hold for arbitrary $\delta \boldsymbol{V}_A$ yields a system of equations for node A

$$\sum_{B=1}^{N_B} \left[\boldsymbol{M}_{AB} \dot{\boldsymbol{V}}_A + \boldsymbol{K}_{AB} \boldsymbol{V}_A \right] = \boldsymbol{f}_A \tag{2.8}$$

where $\boldsymbol{M}_{AB} = m_0 \boldsymbol{L}_{AB}$ and $\boldsymbol{K}_{AB} = D\boldsymbol{L}_{AB}$ are the mass- and stiffness matrices respectively. Time integration of equation 2.8 is carried out using the Störmer-Verlet algorithm which necessitates a constant time-step δt with a numerical constraint $\delta t \ll 2m_0/B$.

In order to determine the stress $\boldsymbol{\sigma}$, strain $\boldsymbol{\varepsilon}$ and displacement $\boldsymbol{u}$ around a dislocation, a linear-elastic boundary value problem (BVP) with discontinuities has to be solved (Weygand et al., 2001, 2002). The BVP is shown on the left side of figure 2.1: Dislocations are embedded into a finite solid of volume Ω with Neumann boundary conditions (traction $\boldsymbol{T}^0$) and Dirichlet boundary conditions (displacement $\boldsymbol{u}^0$) prescribed on boundaries $\partial\Omega_T$ and $\partial\Omega_u$ respectively. The solution to this problem is a decomposition into an analytical part denoted by $(\tilde{\cdot})$-fields, for which analytical elastic fields are given in linear elastic isotropic infinite continua, and a correction part using FEM (Weygand et al., 2001), denoted by $(\hat{\cdot})$-fields, which is added onto the analytical solution to correct for the boundary condition (Van der Giessen und Needleman, 1995). This yields the set of final equations

$$\boldsymbol{\sigma} = \tilde{\boldsymbol{\sigma}} + \hat{\boldsymbol{\sigma}}, \qquad \boldsymbol{\varepsilon} = \tilde{\boldsymbol{\varepsilon}} + \hat{\boldsymbol{\varepsilon}}, \qquad \boldsymbol{u} = \tilde{\boldsymbol{u}} + \hat{\boldsymbol{u}} \tag{2.9}$$

Unfortunately, a computational problem arises due to the long range nature of the stress field accounting for dislocation-dislocation interaction which is $\propto 1/r$: No cut-off can be introduced to reduce the $O(N^2)$ complexity (N being the total number of dislocation segments) commonly applied, for example, for metal potentials in MD. In Weygand et al. (2002) and Weygand und Gumbsch (2005), the authors address this problem by introducing a hierarchical method based on a sub-iteration scheme, where local and global contributions are distinguished. In the so-called sub-timesteps,

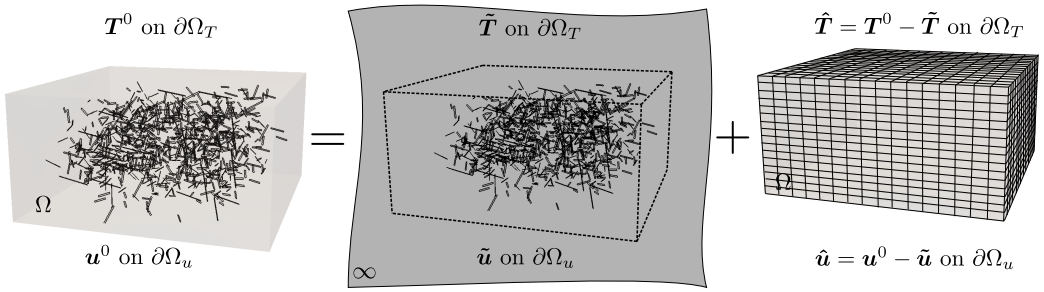

Figure 2.1: Decomposition of the boundary value problem into an infinite solid ($\tilde{(.)}$-fields) containing dislocations and a correction part ($\hat{(.)}$-fields) accounting for the finite solid and boundary condition.

only local interactions in the neighborhood of a segment are accounted for while the global interactions are kept constant. Upon evolving the microstructure over a maximum time interval, global interactions and external conditions are updated. The method offers an acceleration of two orders of magnitude and a stability regarding junctions.

Alternatively, the superposition principle mentioned before could be replaced by the eigenstrain method (Lemarchand et al., 1999, 2001, Vattré et al., 2014). In this model, dislocations are treated as thin plate-like inclusions with their slipped area regularized as plastic strain. DDD is responsible for the dynamics, local reactions and computation of plastic strain, while a finite element part calculates long range stresses due to eigenstrain and solves the boundary condition. Another approach is to use the multipole method developed by Greengard und Rokhlin (1987), which was adapted by Wang und LeSar (1995) and Rickman und Lesar (2002) in the DDD context. It is based on developing complex potentials, from which stress fields can be derived, and expanding them in multipole series. The method reduces the complexity of the problem to $O(N)$.

Dislocation reactions are treated as discrete events. Based on geometrical and energetic criteria (if the elastic energy $\propto Gb^2$ is minimized due to junction formation), segments that are possibly to intersect, are tested if they are favorable to form a junction (Weygand et al., 2002). In an *fcc* crystal four types of junctions are distinguished: Lomer-, glissile-, Hirth- and collinear (Hull und Bacon, 2001).

Partial dislocations are neglected in the used DDD code. This is a good assumption for the materials used which are aluminium and iron, the first has an *fcc* lattice with the largest stacking fault energy (the cores of two partials overlap) (Kubin et al., 1998) while the second is a *bcc* metal with no metastable stacking fault (Vitek, 2004).

2.1.1. Cross-slip

Due to the fact that the Burgers vector $\boldsymbol{b}$ and line direction $\boldsymbol{t}$ of a screw dislocation are parallel to each other, no unique glide plane can be associated to it. A screw dislocation can change the glide plane such that cross-slip can occur whenever the local stresses are higher in the cross-slip plane of the screw dislocation. In the underlying work, different approaches are used to treat cross-slip for *fcc*- and *bcc* lattices.

For *fcc* metals, cross-slip is based on the probabilistic approach given in (Kubin et al., 1992, Weygand et al., 2002). Only a brief summary is provided here. A segment is identified as screw if $|(\boldsymbol{e_b} \times \boldsymbol{e_t}) \cdot \boldsymbol{e_n}| < \sin(\alpha_{\mathrm{cs}})$ with $\alpha_{\mathrm{cs}} = 10°$. For such a segment, a connected sector containing neighboring screw segments is considered for cross-slip if its length L_{sector} is greater than a minimum cross-slip length $L_{\mathrm{min,cs}} > 3l_{\mathrm{min,seg}}$ with $l_{\mathrm{min,seg}}$ the minimum segment length. If this is the case, then the sector is used to calculate an averaged resolved shear stress on both primary τ_{primary} and cross-slip τ_{cs} planes. If $\tau_{\mathrm{cs}} > 1.1\tau_{\mathrm{primary}}$, then the cross-slip probability used in Weygand et al. (2002) is compared to a random number from a uniform distribution. If the probability is higher, then the screw dislocation sector can cross-slip if the bow-out radius in the primary plane is $0.25\mu/(\tau_{\mathrm{cs}}b) < 3L_{\mathrm{sector}}$ to stabilize the cross-slip geometry.

The screw sector for *bcc* metals is defined by connected segments that are of screw type and obey $\tau_{\mathrm{cs}} > \tau_{\mathrm{primary}}$. There are two possible cross-slip planes, but all segments of the sector must utilize the same cross-slip plane. If this is the case, then the sector can cross-slip if $L_{\mathrm{sector}} > L_{\mathrm{min,cs}}$ and the shear stress is larger than the friction stress applied on screw segments (described in section 2.1.5).

2.1.2. Cyclic loading

The applied cyclic loading is imposed using a tensile-compression boundary condition. Either strain- or stress control, which implies displacement control of the cyclic loading are possible. The total displacement in y-direction of the upper surface is linearly increased according to $u_y = \dot{\varepsilon} f(t) L_y$, where $\dot{\varepsilon}$ is the strain rate, $f(t)$ a saw-tooth function and L_y the length of the sample in tensile direction. Once the prescribed displacement yields the specified amplitude, the sign of loading rate is inverted.

The plastic strain in the loading direction $\varepsilon_{\mathrm{pl},y} = (< \tilde{u}_y(0) > - < \tilde{u}_y(L_y) >)/L_y$ is controlled using averaged plastic displacements $< \tilde{u}_y(0) >$ of the lower- and

$< \tilde{u}_y(L_y) >$ upper y-surfaces respectively. In the case of stress amplitude monitoring, the specified stress amplitude is compared with the average stress in y-direction of the surface $y = L/2$.

2.1.3. Grains

The total simulation volume is a cuboidal domain discretized using finite elements with its boundaries being transmissible to dislocation motion. A grain is realized as an embedded volume limited by a set of flat interfaces. Inside the volume the interfaces are shared by the grain and represent grain boundaries. Interfaces shared with the free surface are transmissible to dislocations. The algorithm allows only convex geometries and is described in detail in appendix A. Dislocations are not allowed to penetrate grain boundaries. The grain boundary handling algorithm is explained in section B.1.

2.1.4. Precipitates

Precipitates are modeled as isotropic spherical inhomogeneities with different size and different elastic properties of the matrix. Similar to grain boundaries (section 2.1.3), the interfaces are treated impenetrable to dislocations. Details about the algorithm for the dislocation-precipitate interface handling are given in section B.2. To avoid unnatural structures around the precipitate, dislocation discretization is adapted locally w.r.t. the precipitate radius.

The elastic interaction between a precipitate and a dislocation is separated into two parts:

- an analytical stress field $\boldsymbol{\sigma}^*$ related to the misfit strain $e^* = (R_p - R_H)/R_H$ (Mott und Nabarro, 1940) due to the difference in size between the precipitate of radius R_p and the virtual hole of radius R_H, in which the precipitate is located. The stress field was given by Ashby und Johnson (1969) in spherical coordinates as

$$\begin{aligned} \sigma^*_{rr} &= -4\mu e^*_C \left(\frac{R_p}{||\boldsymbol{r}||}\right)^3 \\ \sigma^*_{\theta\theta} = \sigma^*_{\phi\phi} &= 2\mu e^*_C \left(\frac{R_p}{||\boldsymbol{r}||}\right)^3 \end{aligned} \tag{2.10}$$

where μ is the shear modulus of the matrix, $\boldsymbol{r}$ the position with respect to the inclusion center and $e_C^* = 3K_p/(3K_p + 4\mu)e^*$ (K_p is the bulk modulus of the precipitate) is an extension of the misfit strain e^* denoted as constrained eigenstrain (Eshelby, 1957). By using the constrained eigenstrain e_C^* in equation 2.10, the precipitate's elastic properties are implicitly taken into account.

- a numerical stress field $\boldsymbol{\sigma}^{\mathrm{el}}$ due to difference in elastic constants using a perfectly fitting particle. The stress is calculated using the commercial software `ABAQUS` for a total strain controlled cyclic loading scenario. The loading profile is a saw-tooth function with a period controlled by a fixed strain rate. Hexahedral finite elements with quadratic shape functions are used with a grid refinement around the inclusion. Because the generated mesh is irregular, especially around the inclusion, the stress field is linearly interpolated onto a regular grid and afterwards onto dislocations (appendix C).

The incorporation of the model into the DDD-framework is shown in figure 2.2. The BVP (on the left side) consists of a finite solid with prescribed traction- or displacement boundary conditions containing dislocations and a misfitting inclusion that has different elastic constants (E_p and ν_p) than the matrix (E and ν). The solution is the decomposition of the BVP into an infinite analytical dislocation part (upper left), a correction part due the boundary conditions (upper right), a misfitting inclusion (lower left) and one with different elastic properties than the matrix (lower right) which is solved in `ABAQUS`. Then the total stress can be calculated as

$$\boldsymbol{\sigma} = \tilde{\boldsymbol{\sigma}} + \hat{\boldsymbol{\sigma}} + \boldsymbol{\sigma}^* + \boldsymbol{\sigma}^{\mathbf{el}} \tag{2.11}$$

where $\boldsymbol{\sigma}^{\mathbf{ana}} = \tilde{\boldsymbol{\sigma}} + \boldsymbol{\sigma}^*$ is the analytical part of the stress field from equation 2.9.

2.1.5. Model for *bcc* metals

An atomistically informed discrete dislocation dynamics code has been previously implemented for *bcc* metals (Srivastava et al., 2013, Marichal et al., 2014, Srivastava et al., 2014). In the model, the kink-pair nucleation mechanism is controlled by an activation enthalpy, which is obtained by fitting a line-tension model to atomistic data. It can reproduce the well-known tension-compression asymmetry observed in *bcc* materials and account for non-Schmid effects which are included in the activation enthalpy. Yet, in this thesis, computational efficiency is crucial to simulate a large number of cycles with the available computational resources. Therefore, a somewhat simplified model for *bcc* metals is used as will be explained in the following.

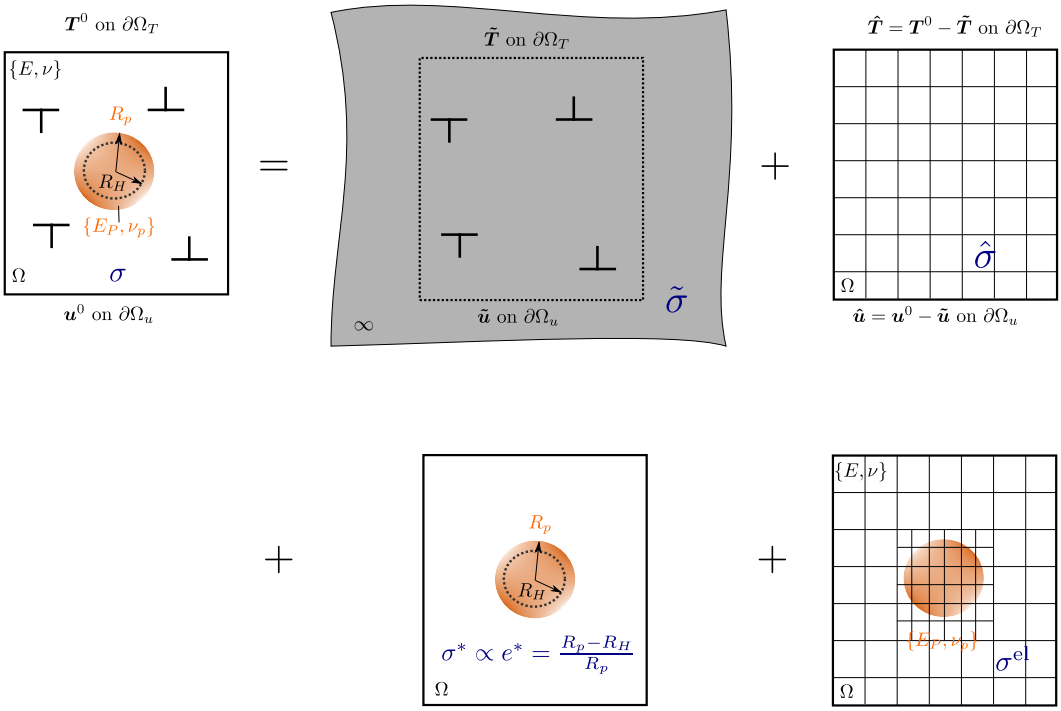

Figure 2.2: The boundary value problem (BVP) containing dislocations and a misfitting isotropic inclusion with different elastic constants than the matrix. The solution is a decomposition into an infinite part containing dislocations (upper left), correction part for boundary conditions (upper right), misfitting inclusion (lower left) and perfect fitting inclusion with different elastic constants (lower right).

It is assumed that dislocation glide occurs on the $\{110\}\langle 111\rangle$ slip systems (table J.1). In order to account for Peierl's barrier, a friction stress τ' is considered for screw segments. For a dislocation segment AB, the friction stress reads

$$\tau'_{AB} = w_{\mathrm{screw}_{AB}} \tau_{\mathrm{crit}} \tag{2.12}$$

where τ_{crit} is a constant critical resolved shear stress and $w_{\mathrm{screw}_{AB}}$ an orientation dependent weight. To avoid sharp cut-offs, a sigmoidal function

$$w_{\mathrm{screw}_{AB}} = \frac{1}{2}\left(\frac{|\boldsymbol{e_{b_{AB}}} \cdot \boldsymbol{e_{t_{AB}}}| - \cos\alpha_{\mathrm{tol}}}{2 \times 10^{-5} + ||\boldsymbol{e_{b_{AB}}} \cdot \boldsymbol{e_{t_{AB}}}| - \cos\alpha_{\mathrm{tol}}|} + 1\right) \tag{2.13}$$

is chosen with $\alpha_{\mathrm{tol}} = 2°$.

The friction stress is included in the calculation of nodal forces $\boldsymbol{f}_A$ (equation 2.7) as follows:

- For a segment AB with length $l_{\mathrm{seg}_{AB}}$ and Burgers vector $\boldsymbol{b}_{AB}$ an averaged resolved shear stress $\tau_{\mathrm{tot}_{AB}} = (f_{AB} + f_{BA})/(b_{AB} l_{\mathrm{seg}_{AB}})$ is calculated in order to compare it with the friction stress τ'_{AB} (equation 2.12) of the segment.

- The calculation of $\boldsymbol{f}_A$ is given by

$$\boldsymbol{f}_A = \sum_{B=1}^{N_B} H(\tau_{\mathrm{tot}_{AB}} - \tau'_{AB}) \left(\boldsymbol{f}_{AB} - \frac{1}{2} b_{AB} \tau'_{AB} l_{\mathrm{seg}_{AB}} \boldsymbol{e}_{\boldsymbol{s}_{\boldsymbol{AB}}} \right) \tag{2.14}$$

  where H is the Heaviside function. If $\tau_{\mathrm{tot}_{AB}}$ is smaller than τ'_{AB} for all segments, node A is immobile.

- Special treatment is given for nodes that are connected to only two segments ($N_B = 2$) with the shear stress of one segment below the friction stress ($\tau_{\mathrm{tot}_{A1}} < \tau'_{A1}$) and the other higher than the friction stress ($\tau_{\mathrm{tot}_{A2}} > \tau'_{A2}$). In this case, the contribution of the force of segment $A2$ is only considered in the screw direction

$$\boldsymbol{f}_A = \boldsymbol{f}_{A2} - (\boldsymbol{f}_{A2} \cdot \boldsymbol{e}_{\boldsymbol{s}_{\boldsymbol{A1}}}) \boldsymbol{e}_{\boldsymbol{s}_{\boldsymbol{A1}}} \tag{2.15}$$

  The latter condition assures a screw segment, which experiences a stress below the frictions stress, remains straight even if one of its nodes is connected to a non-screw segment experiencing a force higher than the friction stress.

Dislocation junctions of type $\langle 100 \rangle$, which are seen in dislocation networks (Matsui und Kimura, 1976, Louchet und Kubin, 1975)), are the reaction product of two $\langle 111 \rangle$-type dislocations for example

$$\frac{1}{2}[111] + \frac{1}{2}[1\bar{1}\bar{1}] \longrightarrow [100].$$

If the resulting $\langle 100 \rangle$ Burgers vector does not lie in one of the planes of the reacting dislocations, then they are sessile geometrically. Glissile $\langle 100 \rangle$-type dislocations have been reported to have a negligible contribution to plastic strain (Hull und Bacon, 2001), therefore, their mobility is reduced in the DDD model by a applying a higher friction stress of $100\tau'$.

2.2 Irreversibility characterization

The text below closely follows the open source publication El-Achkar und Weygand (2018).

2.2.1. Graph representation

A graph representation of the dislocation network allows to employ measures, established in graph theory (Cormen, 2009). The dislocation microstructure is considered as a spatial graph $G = (V, U)$ composed of a set of vertices V and edges U representing discretization nodes and segments respectively. A node V_i is characterized by a Cartesian position $\boldsymbol{x_i}$, whereas an edge U_l connecting nodes V_i and V_j has properties such as line direction $\boldsymbol{t}$ and Burgers vector $\boldsymbol{b}$ acting as a weight. A reaction's Burgers vector $\boldsymbol{b_{react}}$ is calculated using Frank's rule $\sum_i \boldsymbol{b_i} = 0$ (Hirth und Lothe, 1982, Cai und Nix, 2016). Figure 2.3 shows examples of reactions leading to a resulting Burgers vector $\boldsymbol{b_{react}} = 0$: In (a) the end-nodes of a collinear reaction (Madec et al., 2003) (figure 2.3(a)) are connected to each other only by means of virtual edges. The latter type of edges are also stored during the simulation and allow to track the total plastic deformation; in (b) the emitted loop of a glissile reaction (figure 2.3(b)) with Burgers vector $\boldsymbol{b_3}$ results in $\boldsymbol{b_{react}} = 0$, which means that the junction end-nodes are physically connected to one another only by the glissile loop. Therefore, we differentiate between physical connections as those where the edges carry a non-zero Burgers vector and virtual edges belonging to junctions with an effective zero Burgers vector.

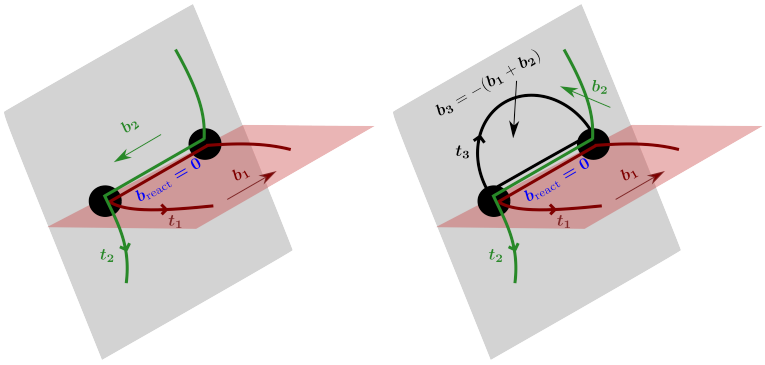

(a) (b)

Figure 2.3: Different reactions with zero-net Burgers vector resulting in different connections: (a) the end-nodes of a collinear reaction have no physical connection. (b) End nodes of a glissile reaction are connected by the emitted loop with Burgers vector $\boldsymbol{b_3}$ (El-Achkar und Weygand, 2018).

Generally, we define the degree of a node in the dislocation graph as the number of connections which a node can have. The following types are identified:

- 1 in the case of pinned end-nodes of e.g. a Frank-Read source or surface nodes. Surface nodes are connected to the outside by virtual dislocation segments to

allow for a proper boundary value problem, which requires closed dislocation loops.

- 2 which are discretization nodes along the dislocation loops. Those nodes are the most frequent ones and can be added or removed easily during rediscretization.
- > 2 are related to dislocation junctions. Due to the use of virtual segments, this number is e.g. 4 for a Lomer; Hirth or collinear reaction and 6 for a glissile reaction. The end-nodes of a junction are therefore connected multiple times. More precisely the number of mutual connections corresponds to the number of loops involved in the junction. Nodes that are shared by several junctions may have even more connections.

Based on physical edges, the dislocation microstructure is filtered into components. A component is a subgraph χ, where any two vertices are connected to each other by physical edges and are not connected to additional vertices in G (Cormen, 2009). This was implemented by traversing the edges of vertices recursively and assigning the same number to edges belonging to the same component.

2.2.2. Prismatic loops

The algorithm of prismatic loop detection is based on filtering the dislocation microstructure into closed components χ_c. Among χ_c, prismatic loops are subsets which contain at least four distinct dislocation loops, found on at least two glide plane families (with distinct plane normals) [1] and are quasi-planar. The evaluation of quasi-planarity requires the calculation of an average normal $\bar{\boldsymbol{n}}(\chi_c)$, which is determined using principle component analysis (Jolliffe, 2013). The positions of m vertices $\in \chi_c$ are written into a $3 \times m$-matrix $\boldsymbol{Q}$ and centered by subtracting the positions from the average position $\boldsymbol{\alpha}(\chi_c)$. A 3×3 covariance matrix $\boldsymbol{C} = \boldsymbol{Q}\boldsymbol{Q}^T$ is calculated, and its eigenvalues λ_1, λ_2 and λ_3 (given in ascending order) are computed. These eigenvalues correspond to the extension of the prismatic loop in different dimensions. In the case of a classical prismatic loop, λ_1 is orders of magnitude smaller than the other two eigenvalues meaning that the eigenvector corresponding to λ_1 is the normal vector $\bar{\boldsymbol{n}}$. A rare case of extremely twisted elongated prismatic loops may show $\lambda_1 \approx \lambda_2$ and $\lambda_3 >> \lambda_2$ meaning that discretization points are spread rather equally in two dimensions. In this case, eigenvalues are evaluated using the correlation matrix $\boldsymbol{R} = \sqrt{\text{diag}(\boldsymbol{C})}^{-1}\boldsymbol{C}\sqrt{\text{diag}(\boldsymbol{C})}^{-1}$. Alternatively, $\bar{\boldsymbol{n}}$ can be calculated using the best planar fit of the point cloud $\boldsymbol{Q}$ with a least squares regression. Finally

[1] overall four glide planes are involved with only two distinct normals.

quasi-planarity is satisfied if the heuristic condition $(\boldsymbol{x} - \boldsymbol{\alpha}) \cdot \bar{\boldsymbol{n}} < 50a$, i.e. the distance from a node $\in \chi_c$ with position $\boldsymbol{x}$ to the plane spanned by the average position $\boldsymbol{\alpha}$ and normal $\bar{\boldsymbol{n}}$ needs to be smaller than $50a$.

Since the discrete dislocation framework assumes dislocation glide, prismatic loops are created by a sequence of cross-slip, collinear- or glissile reactions. Prismatic loops have a Burgers vector which is not contained in the effective loop plane. In the simplest case, they can glide parallel to the Burgers vector direction along prisms of different complexity. In the context of fatigue irreversibility, prismatic loops are particularly stable because the total force acting on them under homogeneous stress fields is zero allowing the loop to only twist due to moments along the glide cylinder (Hirth und Lothe, 1982, Kroupa, 1966).

The simplest type of prismatic loop consists of interstitial or vacancy type and due to volume conservation of dislocation glide. They effectively have to occur in pairs (one interstitial and the other vacancy type) except if they are generated at the surface or from climbing dislocations. The pairs are linked by virtual edges within the dislocation network (section 2.2.1). Since there are several possibilities for the formation of prismatic loops or prismatic clusters, the following classification is done (figure 2.4): prismatic loops of the 1^{st} order (figure 2.4(a)) which arise due to cross-slip and annihilation reactions involving only one Burgers vector. Only two glide plane families (two distinct normals), are involved in this construction and at least four dislocation sectors. This type is the simplest prismatic loop. Furthermore, prismatic loops of the 2^{nd} order (figure 2.4(a)) are defined to comprise three different glide planes and comprise also former Lomer-type junctions (colored in yellow) and non-junction dislocations. At first sight, this looks surprising, as a Lomer reaction generally involves two dislocations. Here only the Lomer reaction and only a single dislocation emerge from the respective end-nodes. This transformation of a Lomer reaction to a spiral source with pinned end-nodes was first observed by Motz et al. (2009). The mechanism leading to this structure involves cross-slip respectively glissile reaction of the two dislocations arms initially forming the Lomer reaction, involving the third glide plane compatible with their respective Burgers vectors. This plane is inclined to the line direction of the Lomer junction. Therefore the incorporated Lomer-junctions' end-nodes are pinned, evoke extreme stability and serve as extended obstacles or sources of stress gradients.

Among the evolved structures are prismatic loops of equiaxed or elongated shape (figure 2.4(a)) which have been previously reported in (Feltner, 1965, 1966). The shape characterization is approached here using the ratio

$$p_{\text{shape}} = \frac{4\sqrt{A_{\text{enc}}}}{U_{\text{perim}}} \tag{2.16}$$

where U_{perim} is the perimeter and A_{enc} the enclosed area of a prismatic loop spanned by $\bar{\boldsymbol{n}}$ and $\boldsymbol{\alpha}$. The value spectrum of the ratio is $p_{\text{shape}} \in [0, 1]$ where $p_{\text{shape}} = 1$ for equiaxed and $p_{\text{shape}} < 1$ for elongated prismatic loops. For rectangular prismatic loops, side lengths l_1 and l_2 can be retrieved by solving the set of equations

$$l_1 + l_2 = \frac{U_{\text{perim}}}{2} \tag{2.17}$$

$$l_1 + l_2 \frac{p_{\text{shape}}^2 - 2\sqrt{1 - p_{\text{shape}}^2} - 2}{p_{\text{shape}}^2} = 0 \tag{2.18}$$

which can be used to calculate the maximum loop dimension defined as $\max(l_1, l_2)$. The other type of extracted components are classified as dislocation debris (figure 2.4(c)) which are non-planar subsets of χ_c and may contain Lomer junctions. Similar to the 2nd order type, they are very stable.

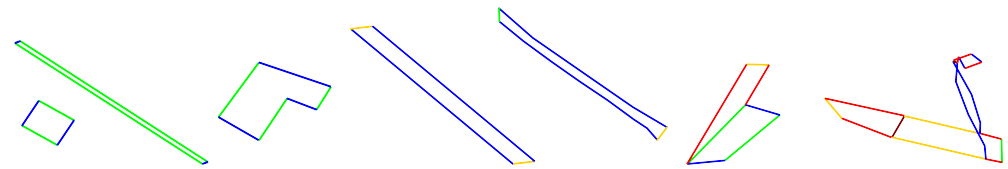

(a) prismatic loops of the 1st order (b) prismatic loops of the 2nd order (c) dislocation debris

Figure 2.4: Prismatic loops of different orders in (a) and (b). Coloring is according to plane normals, yellow represents a Lomer junction (El-Achkar und Weygand, 2018).

2.2.3. Dislocation dipoles

Dislocation dipoles are treated more generally compared to previously discussed defects. The condition to detect dislocation dipoles is purely geometrical, hence, dipolar prismatic loops are a subgroup of dislocation dipoles. A pair of dislocations (dislocations I and II) is considered as a dislocation dipole if both dislocations are parallel, at a distance $h < h_{\text{crit}}$ and span a minimum necessary length of $l > l_{\text{crit}}$. The algorithm starts on the level of a dislocation loop, all dislocation loops lying in its vicinity that have the same normal vector and are located in parallel glide

planes are considered. To determine if another loop is close, adaptive discretization boxes which depend on the volume size and maximum dislocation segment length are used. If a dislocation loop lies in one of the neighboring boxes, then it is evaluated. Furthermore, the search continues on the level of dislocation segments. More specifically, edges i and j of dislocations I and II respectively are classified as parallel if the closest distance vector connecting the two edges forms an angle larger than 80° with both edges. The critical allowed distance between the edges is calculated using $h_{\mathrm{crit}} = \frac{\mu b}{8\pi(1-\nu)\tau_{\mathrm{crit}}}$ (Kroupa, 1966), where τ_{crit} is the critical resolved shear stress required to destabilize a dipole. Here, τ_{crit} is assumed to be the macroscopic total resolved shear stress on the system, which is measured from the stress-strain curve. The final restriction is that the dislocation pair needs to span a minimum length of $L_{\mathrm{min}} > 2h$ in order to exceed intrinsic discretization lengths. Furthermore dislocations in the vicinity of grain boundaries (at distances $< 100a$ from a grain boundary) are ignored in this algorithm to avoid mistaking dislocation dipoles with grain boundary pile-ups.

2.2.4. Dislocation structure analysis

A fatigued dislocation microstructure is well-known to show different types of pattern formation depending on the prescribed strain amplitude, crystal orientation or ease to cross-slip (Mughrabi, 2010, Xiao und Umakoshi, 2003). To analyze various resulting dislocation structures, dislocation edges are binned according to their line direction onto $\langle 110 \rangle$, $\langle 112 \rangle$ and $\langle 122 \rangle$ directions with $\approx 16°$ tolerance. In the case of pronounced dislocation bundles, the following method to characterize their spatial distribution is used: dislocation dipoles which belong to a pronounced alignment direction are filtered and the intersection points r_i of such dislocations and 200 planes [2] with normal $\boldsymbol{n}_{\mathrm{plane}} = \boldsymbol{e_t}$ are calculated, for which the 2d pair correlation function

$$g_{2\mathrm{d}}(r) = \frac{1}{A_{\mathrm{shell}} N_{\mathrm{inter}} \rho_{\mathrm{corr}}} \sum_{i}^{N} \sum_{j \neq i}^{N} \delta(r - r_{ij}) \tag{2.19}$$

is computed. In equation 2.19, r_{ij} is the distance between points i and j, $\rho_{\mathrm{corr}} = \frac{N_{\mathrm{inter}}}{A}$ (A area of a plane and N_{inter} total number of intersection points) is the number density used for normalization and $A_{\mathrm{shell}} = \pi(r_{\mathrm{out}}^2 - r_{\mathrm{in}}^2)$ the area of the shells, where $dr = r_{\mathrm{out}} - r_{\mathrm{in}}$ (figure 2.5). Finally the mean pair correlation function is obtained by averaging $g_{2\mathrm{d}}$ in $\boldsymbol{t}$-direction.

[2] the distance between the planes is $100a$, such that a combination of the projected positions resembles the 3-dimensional microstructure along the desired direction.

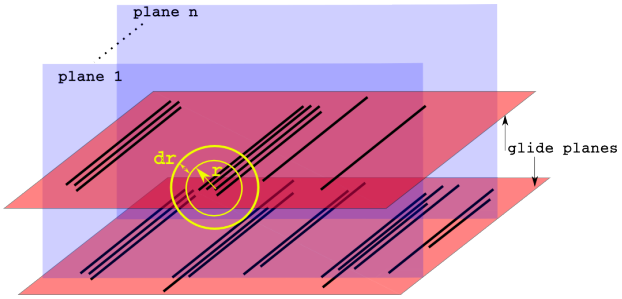

Figure 2.5: Spatial characterization of a dislocation bundle structure using 2d pair correlation function.

On the other hand, microstructures which exhibit a cell structure pattern are analyzed using fractal box-counting technique (Hähner et al., 1998a). This measure has been previously used in the DDD context by Hussein und El-Awady (2016a), however not normalized by the grid size.

A further measure to characterize dislocation density around Lomer junctions is computed using

$$\rho_{\text{around}}(r) = \frac{1}{N_L \rho_{\text{t}} \frac{4}{3}\pi r^3} \sum_{i}^{N_L} \sum_{j \neq i}^{N} l_{\text{segment},j} w_{ij}(r) \tag{2.20}$$

where N_L is the number of Lomer-junction segments, l_{segment} the length of the segment and

$$w_{ij}(r) = \begin{cases} 1 & \text{if} \quad d_{ij} < r \\ 0 & \text{otherwise} \end{cases} \tag{2.21}$$

where d_{ij} is the distance between the middle point of a segment i (belonging to a Lomer junction) and any other segment j. Self-correlation among Lomer junctions is deliberately ignored.

2.2.5. Macroscopic damage parameters

Surface roughness Stable dislocation arrangements manifest themselves in the form of irreversible surface steps leading to a roughening of the free surface. The deep steps are well-known to cause stress localization leading to crack initiation. Therefore, to analyze the surface topography evolution during cyclic loading, the surface, which is initially flat, is discretized into a two dimensional equidistant grid and the plastic component $\tilde{u}$ is calculated during post-processing analytically at

each grid point. Provided displacement distributions, surface roughness can be characterized using Root Mean Square (RMS)

$$\mathrm{RMS} = \sqrt{\frac{1}{N}\sum_{i=1}^{N}(\tilde{u}_i - <\tilde{u}>)^2} \tag{2.22}$$

With its help, the irreversibility factor p, which quantifies the fraction of slip which is irreversible (Differt et al., 1986, Mughrabi, 1999, Weidner et al., 2010), can be calculated

$$\mathrm{RMS} = 1.2\sqrt{4N_{\mathrm{cycles}}\gamma_{\mathrm{pl,loc}}pb\tilde{h}} \tag{2.23}$$

where $\gamma_{\mathrm{pl,loc}}$ is the resolved shear strain amplitude, N_{cycles} the number of cycles and $\tilde{h}$ the distance along which the peak-to-valley roughness is measured. The resolved shear strain amplitude can be estimated from $\gamma_{pl,loc} = M\Delta\varepsilon_{\mathrm{pl,loc}}/2$ where $\Delta\varepsilon_{\mathrm{pl,loc}}/2$ is the local axial plastic strain amplitude and $M = 2.24$ the Sachs orientation factor. The p-factor describes the degree of irreversibility of the system ($0 < p < 1$), hence, it is zero for fully reversible systems and equal to one for fully irreversible systems.

An additional sensitivity measure to characterize the change in surface step heights is the maximum value of the norm of the gradient of the displacement field $||\nabla\tilde{u}||$. The gradient, for example, for the z-surface $\nabla\tilde{u}_z = (\partial_x\tilde{u}_z, \partial_y\tilde{u}_z)$ is calculated by computing gradients along the x- and y directions of the grid using second order accurate central differences.

Irreversible plastic strain In plastic strain-controlled simulations, the total net plastic strain in loading direction $\varepsilon_{\mathrm{pl,y}}$, which is proportional to total signed areas swept by dislocations, is a cyclic function that is impelled to pass through zero for each cycle. The implication is that for $\varepsilon_{\mathrm{pl,y}} = 0$ it cannot be distinguished whether the system is fully reversible with every individual FR-source reverting to its initial state or if an irreversibility is present but signed swept areas cancel out. To differentiate between both cases, the absolute value of swept areas can be utilized by summing up the von Mises plastic strain $\varepsilon_{\mathrm{pl,vM}}$ of N loops to yield the so-called irreversible plastic strain $\varepsilon_{\mathrm{pl,irre}}$. This measure can be used to calculate the p-factor (Differt et al., 1986) directly from dislocations

$$p = \frac{\varepsilon_{\mathrm{pl,irre}}}{\varepsilon_{\mathrm{pl,cum}}} = \frac{\sum_{i=1}^{N}\varepsilon_{\mathrm{pl,vM}_i}}{2\Delta\varepsilon_{\mathrm{pl}}N_{\mathrm{cycles}}} \tag{2.24}$$

where $\varepsilon_{\mathrm{pl,cum}} = 2\Delta\varepsilon_{\mathrm{pl}}N_{\mathrm{cycles}}$ is the cumulative plastic strain.

3. Results

3.1 Fatigue in *fcc* surface grains

The results in the succeeding sections present cyclic loading simulations of surface grains for different tensile axis orientations. As a ductile *fcc* material model, Aluminium is chosen and assumed to be elastically isotropic (shear modulus $\mu = 27$ GPa, Poisson ratio $\nu = 0.347$, lattice constant $a = 0.404496$ nm, drag coefficient $D = 10^{-4}$ Pa s and mass per unit length $m_0 = 1.1 \times 10^{-16}$kg/m). A large part of the results are published in El-Achkar und Weygand (2018, 2019).

3.1.1. [010]-tensile axis orientation

Aspects of grain geometry

To study the influence of grain geometry w.r.t. dislocation irreversibility, an initial FR source of length $2000\,a$ is positioned at the center of a surface grain and subjected to a total strain controlled cyclic loading. The FR source has a Burgers vector $\boldsymbol{b_1} = a/2[0\bar{1}1]$ (large surface component) and is located on a slip plane with normals vector $\boldsymbol{n_1} = 1/\sqrt{3}(111)$. The latter is enforced using a saw-tooth function (section 2.1.2) operating at an amplitude of $\varepsilon_{\text{tot}} = 0.2\%$ and a strain rate of $\dot{\varepsilon} = \pm 5000\text{s}^{-1}$ that complies to a frequency of 6250 KHz. The surface grain itself is embedded into an isotropic elastic medium and modeled such that its grain boundaries are impermeable to dislocation motion. Details about the grain construction algorithm and grain boundaries are given in sections A and B.1 respectively. Two different surface grain geometries are examined (table 3.1): A cuboidal geometry in setup 1a (figure 3.1(b)) and a truncated dodecahedron in setup 1c (figure 3.1(c)). The crystal orientation w.r.t. the tensile axis and free surface is given in figure 3.1(a). The boundary conditions for both setups are shown in the figures: Dislocations can escape the grain only through the surface, displacement boundary conditions $u_y = 0$

Setup	Tensile axis y	Complementary axis x	Microstructure	Grain shape
1a	[010]	[100]	single FR source $\boldsymbol{b_1} = a/2[0\bar{1}1]$	surface cuboid
1b	[010]	[100]	single FR source $\boldsymbol{b_2} = a/2[110]$	surface cuboid
1c	[010]	[100]	single FR source $\boldsymbol{b_1} = a/2[0\bar{1}1]$	truncated surface dodecahedron
1d	[010]	[100]	single FR source $\boldsymbol{b_1} = a/2[0\bar{1}1]$	bulk cuboid
1e	[010]	[100]	random distribution of FR sources $\rho_t = 4.5 \times 10^{11}\mathrm{m}^{-2}$	truncated surface dodecahedron
1f	[010]	$\boldsymbol{e_{b_6}} = \frac{1}{\sqrt{2}}[101]$	random distribution of FR sources $\rho_t = 4.5 \times 10^{11}\mathrm{m}^{-2}$	truncated surface dodecahedron

Table 3.1: Setups' nomenclature for a [010]-tensile axis orientation.

are applied on the bottom surface and $u_y = \dot{\varepsilon} L f(t)$ on the top surface $y = L$. The remaining degrees of freedom at the surface have traction free boundary conditions.

In figure 3.2, the evolution of several microstructural measures are shown for 6 cycles. The dislocation density ρ_t (figure 3.2(a)) is up to 1.5 cycles almost equal for both the dodecahedron (setup 1c) and the cuboid (setup 1a). Afterwards ρ_t increases gradually for the cuboid, whereas the dodecahedron shows both an increase and decrease of the dislocation density until 4 cycles. Then the dodecahedron shows a stable increase of the dislocation density to reach $\rho_t = 5.5 \times 10^{12}\mathrm{m}^{-2}$, on the other hand the cuboid reaches $\rho_t = 6.8 \times 10^{12}\mathrm{m}^{-2}$. The evolution of the number of cross-slip and collinear junctions (figure 3.2(b)) shows higher number of reactions for the cuboid than for the dodecahedron. The latter shows small number of cross-slip events and collinear reactions that reach zero after every cycle. On the other hand, the cuboid shows for both reaction types an increasing trend reaching almost 4.5 and 2.7 times more cross-slip events and collinear reactions respectively than the dodecahedron. A similar behaviour is observed in terms of the number of prismatic loops (figure 3.2(c)). The dodecahedron shows a small almost constant number of 8 prismatic loops, whereas an increase in the number of loops is seen for the cuboid which oscillates around 60 prismatic loops after 4.5 cycles. The evolution of the

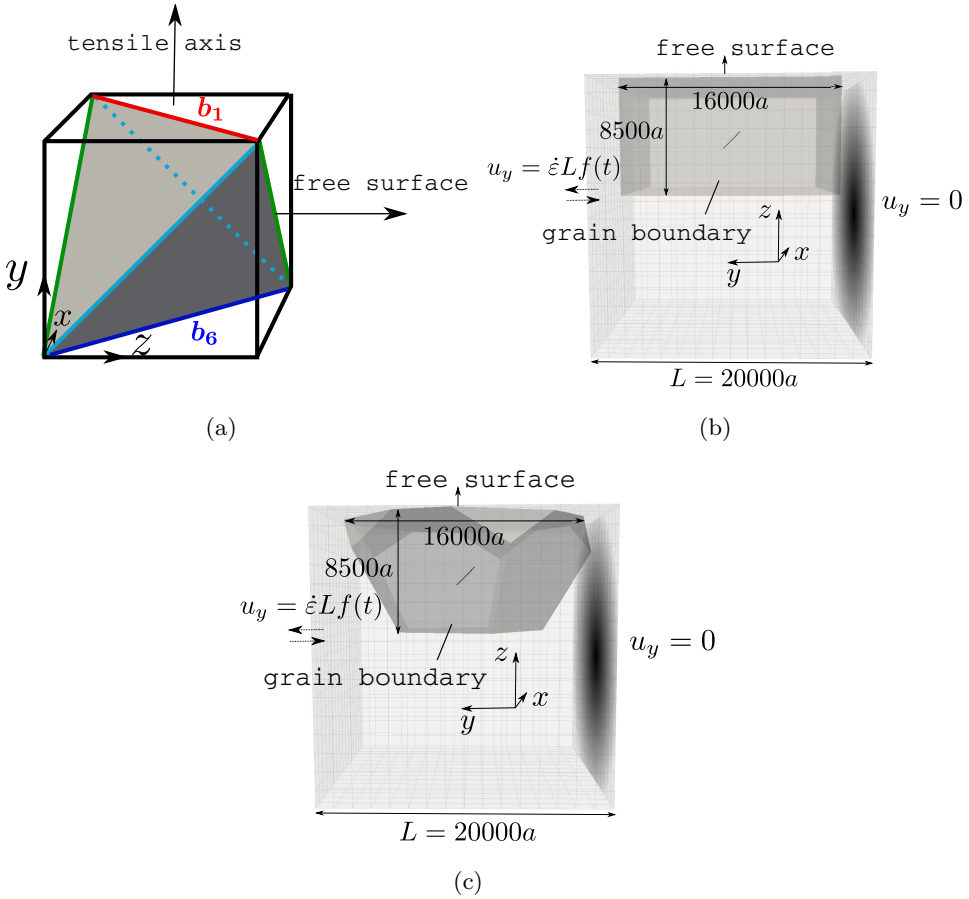

Figure 3.1: (a) [010] crystal orientation of setups 1a-1e. Initial- and boundary conditions of the (b) cuboid- and (c) dodecahedron surface grain embedded into an elastic volume (El-Achkar und Weygand, 2018). The initial dislocation microstructure consists of a single FR source of length 2000 a.

averaged von Mises plastic strain (figure 3.2(d)) shows up to 2-3 times smaller values for the dodecahedron compared to the cuboidal grain.

Another aspect is the location of the grain w.r.t. the free surface. The analysis includes the cuboidal surface grain from figure 3.1(b) (setup 1a) and the exact same grain with the same initial microstructure embedded into the bulk (setup 1d in table 3.1), i.e. having all of its surfaces as grain boundaries. The evolution of the dislocation density (figure 3.3(a)) shows that for the bulk grain the dislocation density reaches zero after unloading steps meaning almost full reversibility, whereas as mentioned above, the surface grain shows an increase in this quantity. In figure 3.3(b), the microstructure is shown for maximum load for the bulk grain after 15 cycles. Pile-ups in the primary plane (blue color) and dislocations that form due to double cross-slip from the original FR source are observed. A remarkable feature is the symmetry of the developed structure w.r.t. the original plane.

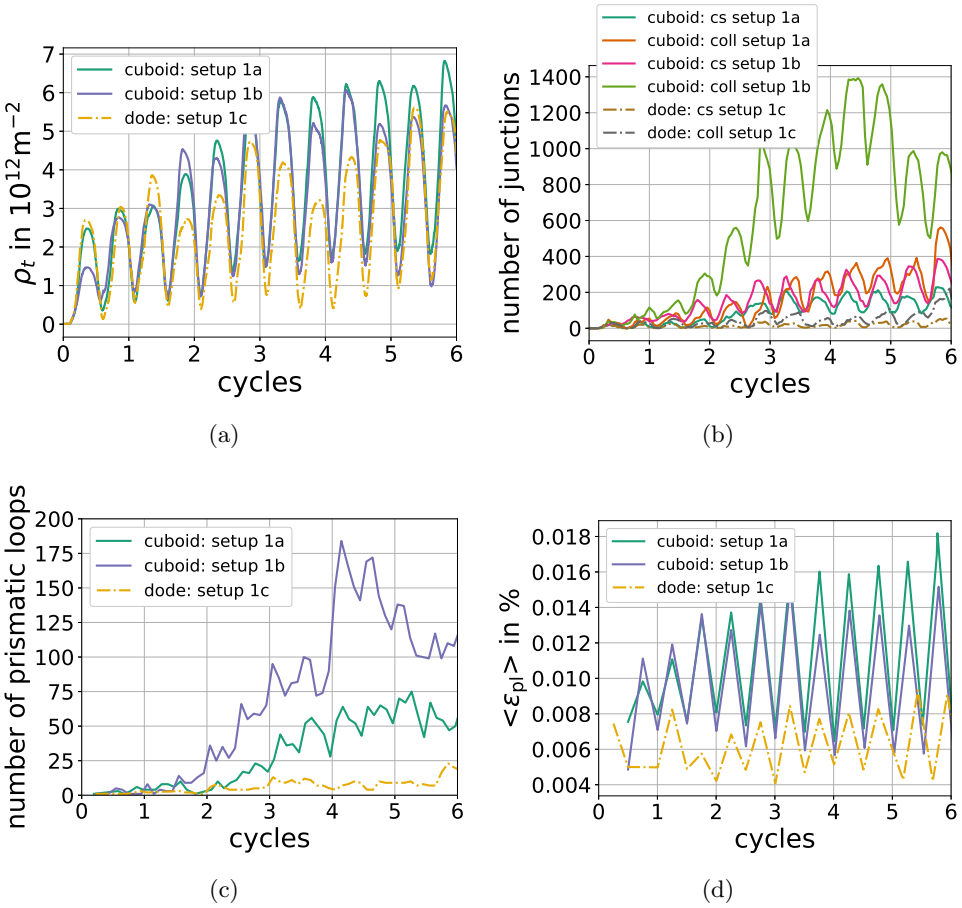

Figure 3.2: Evolution of the (a) dislocation density, (b) number of junctions, (c) number of prismatic loops and (d) mean von Mises plastic strain for the cuboid setup 1a ($\boldsymbol{b_1} = a/2[0\bar{1}1]$) and setup 1b ($\boldsymbol{b_2} = a/2[110]$) orientations and dodecahedron for $\boldsymbol{b_1}$ Burgers vector orientation (setup 1c) (El-Achkar und Weygand, 2018).

Burgers vector orientation

The influence of the Burgers vector orientation is analyzed. Two different orientations for the initial FR source in the cuboidal surface grain (figure 3.1(b)) are considered (table 3.1):

- Setup 1a: the Burgers vector $\boldsymbol{b_1} = a/2[0\bar{1}1]$ has a large free surface component.
- Setup 1b: the Burgers vector $\boldsymbol{b_2} = a/2[110]$ is parallel to the free surface.

The microstructure for the first cycle for both setups is shown in figure 3.4. After reaching the critical stress for activating the FR source, dislocations pile-up at at the grain boundary in setup 1a until a higher stress is reached on the cross-slip plane. The latter triggers cross-slip of screw dislocations in the vicinity of the grain

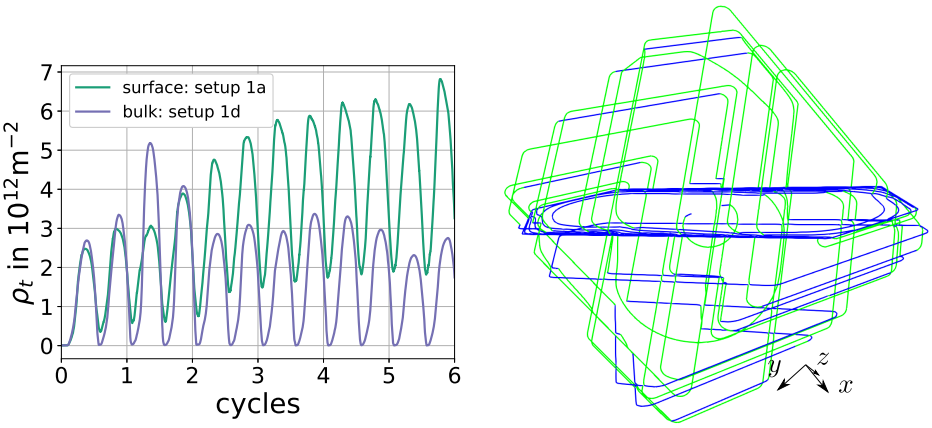

(a) (b)

Figure 3.3: (a) Comparison of the dislocation density evolution for the surface- (setup 1a) and bulk grain (setup 1d) for $\boldsymbol{b_1}$ orientation. (b) Dislocation microstructure at load maximum of the bulk grain after 15 cycles.

boundary on both ends of the cuboid (upward and downward motion depending on the line direction). The emission of several loops shows that cross-slips events also occur at a far distance from the grain boundary. On the other hand, in setup 1b, where the Burgers vector $\boldsymbol{b_2}$ is parallel to the free surface, cross-slip takes place in the vicinity of only one grain boundary which is of screw orientation. After 5 cycles, the microstructure in setup 1a shows a stair-like structure spread throughout the volume with many cross-slip events and small prismatic loops. Setup 1b shows a distinct structure that is primarily filled with pairs of prismatic loops of different sizes.

The evolution of microstructural measures shown in figure 3.2 indicates no substantial difference in the dislocation density and averaged von Mises strain plastic for both setups. Yet, more dislocation reactions are observed in setup 1b. Collinear reactions occur up to three times more for setup 1b than 1a. Also cross-slip events are more frequent in setup 1b and the dislocation density due to cross-slip (not shown) is up to three times larger. The number of prismatic loops shows a similar trend as the number of collinear reactions: The number of prismatic loops in setup 1b increases gradually until a maximum is reached in the 4th cycle followed by a decrease at the end of the cycle, whereas for setup 1a they increase and stabilize after the 4th cycle. It is evident that the number of prismatic loops are 2-3 times higher in setup 1b.

The distribution of the averaged von Mises plastic strain in voxels of side-length $400\,a$ is shown for load maximum for both setups in figure 3.5. It is apparent, that plastic strain is spread for setup 1a homogeneously throughout the whole grain in

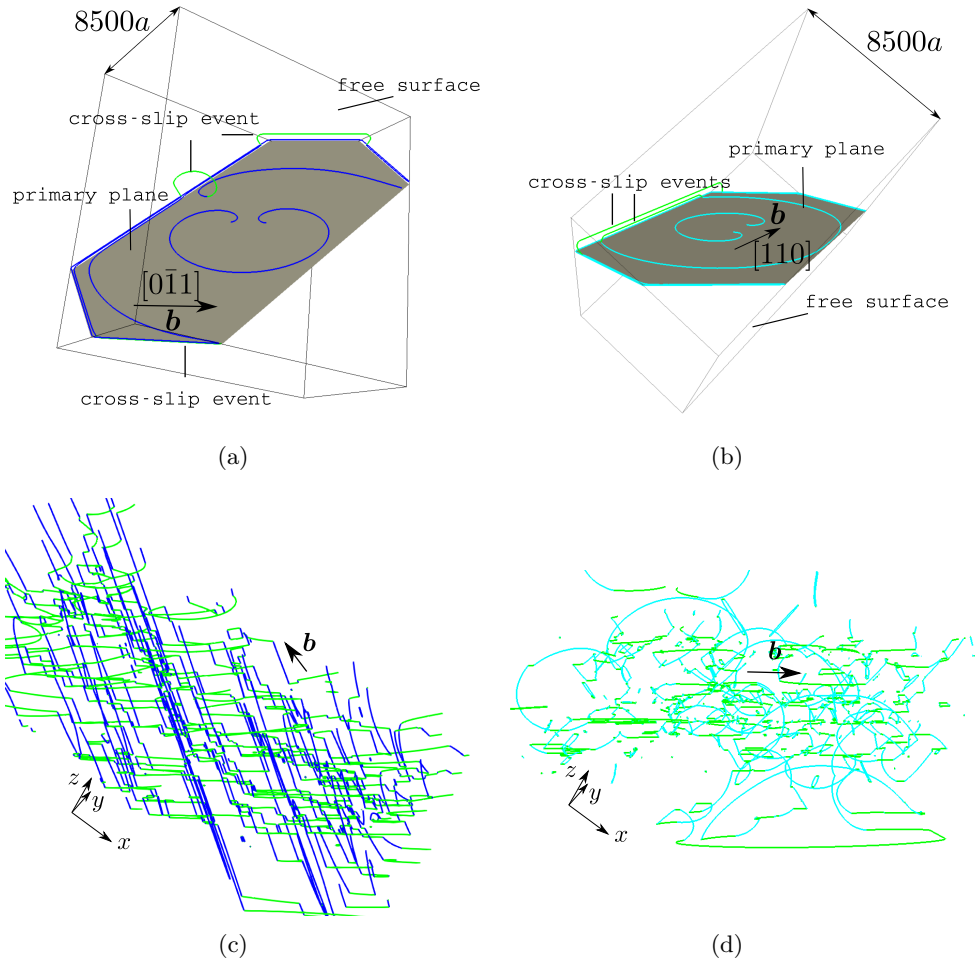

Figure 3.4: Dislocation microstructure during tensile loading of the first cycle of the cuboidal surface grain for (a) setup 1a ($\boldsymbol{b_1} = a/2[0\bar{1}1]$) and (b) setup 1b ($\boldsymbol{b_2} = a/2[110]$) (El-Achkar und Weygand, 2018). The primary slip plane is highlighted in gray. Microstructure in the fifth cycle while unloaded (dislocation density minimum) for setup (c) 1a and (d) 1b.

contrast to a localization in setup 1b. In both setups peak values of plastic strain can be observed along the Burgers vector in microstructural zones along which channels of dipolar loops are found.

The characterization of irreversibility extends to surface analysis (section 2.2.5). Setup 1b shows surface steps in the direction of the Burgers vector related to bowing out of dislocations which gradually disappear after unloading. Conversely, for setup 1a a pronounced surface roughness appears and remains even after unloading. The microstructure in figure 3.6(a) resembles an alignment of prismatic loops and dislocation dipoles along $\boldsymbol{b_1}$ that end at the surface as permanent steps. The surface profile (grid spacing $\Delta = 156.25\,a$) along the y-direction in the middle of the surface

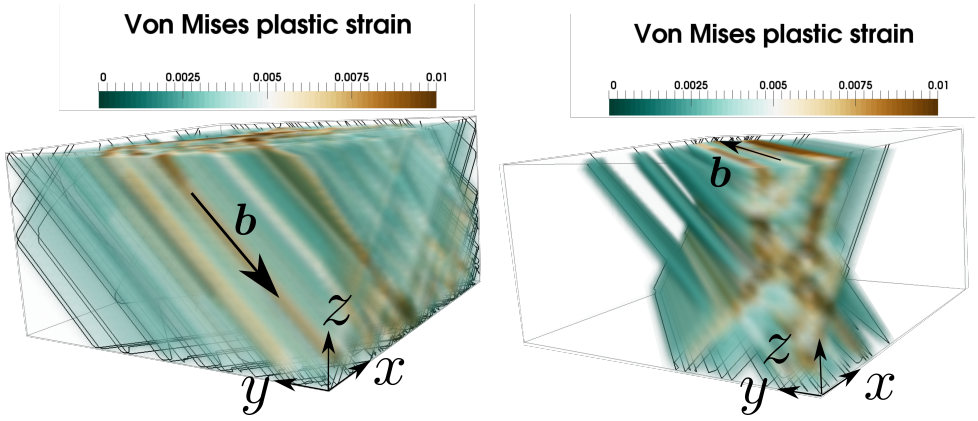

(a) (b)

Figure 3.5: Distribution of the voxel-averaged von Mises plastic strain in the cuboidal surface grain for (a) setup 1a ($\boldsymbol{b_1} = a/2[0\bar{1}1]$) and (b) setup 1b ($\boldsymbol{b_2} = a/2[110]$). The voxels are of $400\,a$ side length (El-Achkar und Weygand, 2018).

for cycles 2 and 5 (figure 3.6(b)) shows a drastic topographical change: While the surface favors a stair-like profile after 2 cycles, a rougher surface is observed after 5 cycles due to localized and sharp peaks. A detailed analysis on the surface roughness

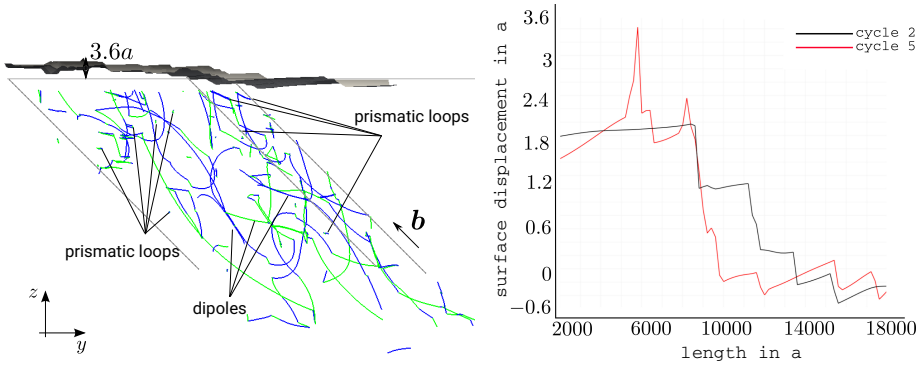

(a) (b)

Figure 3.6: (a) A slice of the dislocation microstructure parallel to $\boldsymbol{b_1}$ and plastic surface displacement for the cuboid (setup 1a) after 5 cycles while unloaded. (b) Plot of the plastic surface displacement along the y-direction in the middle of the surface for cycles 2 and 5 (El-Achkar und Weygand, 2018).

evolution is presented in figure 3.7 and consists of contour plots of the surface, the average displacement, RMS (given in error bars) and minimum/maximum values for load maximum. The minimum/maximum values as well as RMS increase from the start to reach their highest values after 4 cycles (point V) and then slightly decrease. After one cycle, surface displacements are found to be on average positive. The contour plots show during the first 2 cycles extended displacement steps due

to individual dislocation arms ending at the surface. The steps show that four dislocations from both primary and cross-slip planes contribute to the steps (point I). The steps increase in number after the first and second cycle (points II and III) and form a complex topography afterwards from the third cycle. During the latter, the surface is divided into two parts: One side consists of positive and the other of negative displacements separated by a small region of zero displacement. The formation of an irreversible step is observed to form whenever a prismatic loop leaves the surface while its counter part remains in the volume.

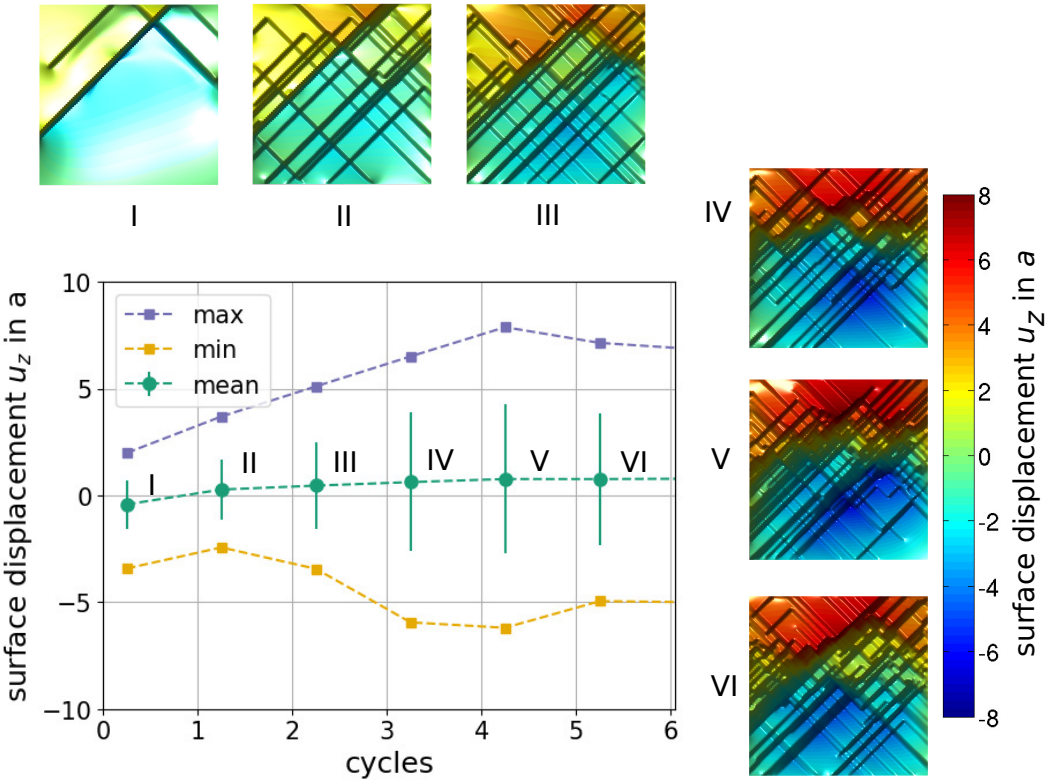

Figure 3.7: Evolution of the surface roughness measures and contour plots of the plastic surface displacement of the cuboid (setup 1a) for maximum load (the error bars represent RMS) (El-Achkar und Weygand, 2018).

Glide system interaction and crystal rotation around tensile axis

In the preceding section, the aspects of a single FR source in crystal orientation of figure 3.1(a) subjected to cyclical loading were examined. To understand the role of interplay of different glide systems and their orientation w.r.t. the tensile axis, FR sources of lengths $4745a$ are populated into the truncated dodecahedral surface grain of figure 3.1(c) such that the total dislocation density $\rho_t = 4.5 \times 10^{11}\mathrm{m}^{-2}$ yielding a

mean dislocation spacing $1/\sqrt{\rho_t} = 3685.4\,a$ (setup 1e in table 3.1). The boundary conditions are kept as above with the exception of a plastic strain controlled cyclic loading (section 2.1.2) using an amplitude of $\Delta\varepsilon_{\mathrm{pl}}/2 = 0.01\%$. To test the influence of a crystal rotation about the tensile axis (setup 1f), the crystal system is rotated with angle of 45° about the tensile axis such that $\boldsymbol{b_2} - \boldsymbol{b_5}$ are symmetric w.r.t. the free surface (figure 3.8). Intermediate rotations around the tensile axis are given in section F of the appendix.

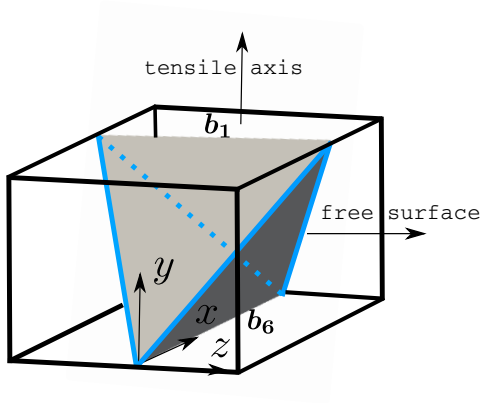

Figure 3.8: Setup 1f: Thompson tetrahedron displaying the rotated [010] crystal orientation w.r.t. the tensile axis and free surface (table 3.1) (El-Achkar und Weygand, 2019).

The final dislocation density distribution for setup 1e (figure 3.9(a)) shows glide systems 2, 6, 7 and 11 (Burgers vectors $\boldsymbol{b_5}$ and $\boldsymbol{b_2}$ respectively) with highest dislocation density followed by systems 1, 12, 5 and 8 (Burgers vectors $\boldsymbol{b_4}$ and $\boldsymbol{b_3}$ respectively) that have around half the dislocation density of the latter. Systems 3, 9, 4 and 10 (Burgers vectors $\boldsymbol{b_6}$ and $\boldsymbol{b_1}$ respectively) show almost no activity[1]. In setup 1f (figure 3.9(b)), the dislocation density is almost equally distributed among systems 1, 2, 5, 6, 7, 8, 11 and 12. The remaining systems have a small dislocation density $\approx 3\%$ per glide system.

Another distinct behavior is visible in the number of Lomer reactions (figure 3.10(a)): Their number increases at a higher rate in setup 1f than setup 1e and reaches around 900 junctions in contrast to 220 after 5 cycles. Also the surface deformation after 4 cycles reveals qualitative differences (figures 3.10(b) and 3.10(c)): Setup 1e shows a well-defined block structure whereas setup 1f shows triangular surface markings. Noticeable is the location of intrusions that are in the center of the surface in setup 1e but spread along the whole surface in setup 1f.

[1] Glide system numbering can be found in figure J.1

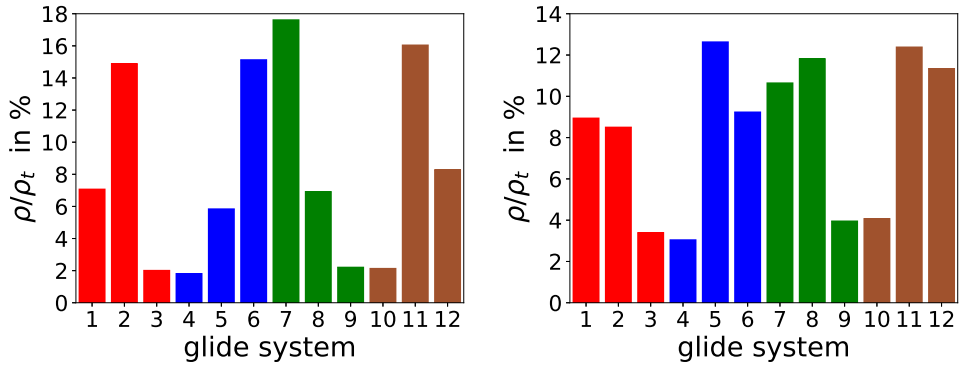

(a) (b)

Figure 3.9: Distribution of the fraction of the final dislocation density ρ per glide system w.r.t. the total dislocation density ρ_t for [010] crystal orientation setups (a) 1e and (b) 1f (table 3.1). Glide systems belonging to the same glide plane obtain the same color (El-Achkar und Weygand, 2019).

Additional sensitivity analysis for a 10° rotation from the [010]-tensile axis is given in section F of the appendix.

Pattern formation

The evolved microstructure of setup 1e shows in a cross-section perpendicular to the [100] direction a cellular structure after 16 cycles (figure 3.11(a)). A 2000 a thin TEM-like (Transmission Electron Microscope) slice is prepared by discretizing the volume into boxes of side-lengths of 400 a and keeping dislocations only if they have lengths above 500 a. The latter procedure allows to remove debris which is unconnected to the main structure. To quantitatively characterize the obtained structure, the box-counting technique (Hähner et al., 1998a) is applied to the dotted region of figure 3.11(a) which contains the largest- and second largest cells denoted by numbers 1 and 2 respectively (figure 3.11(b)). The scaled box-counting measure $N(\Delta x)^2$ shows the slope of this measure approaches zero for box sizes above $\Delta x \approx 900a$ and below $\Delta x \approx 10a$.

Amplitude variations

For the preceding setup 1e (table 3.1), simulations for a range of applied plastic strain amplitudes $\Delta\varepsilon_{\mathrm{pl}}/2 = \{0.001\%, 0.002\%, 0.004\%, 0.01\%\}$ are conducted. Since the dislocation density is directly proportional to the applied amplitude (computational cost), final cycles of 160, 50, 30 and 16 for the range of amplitudes are

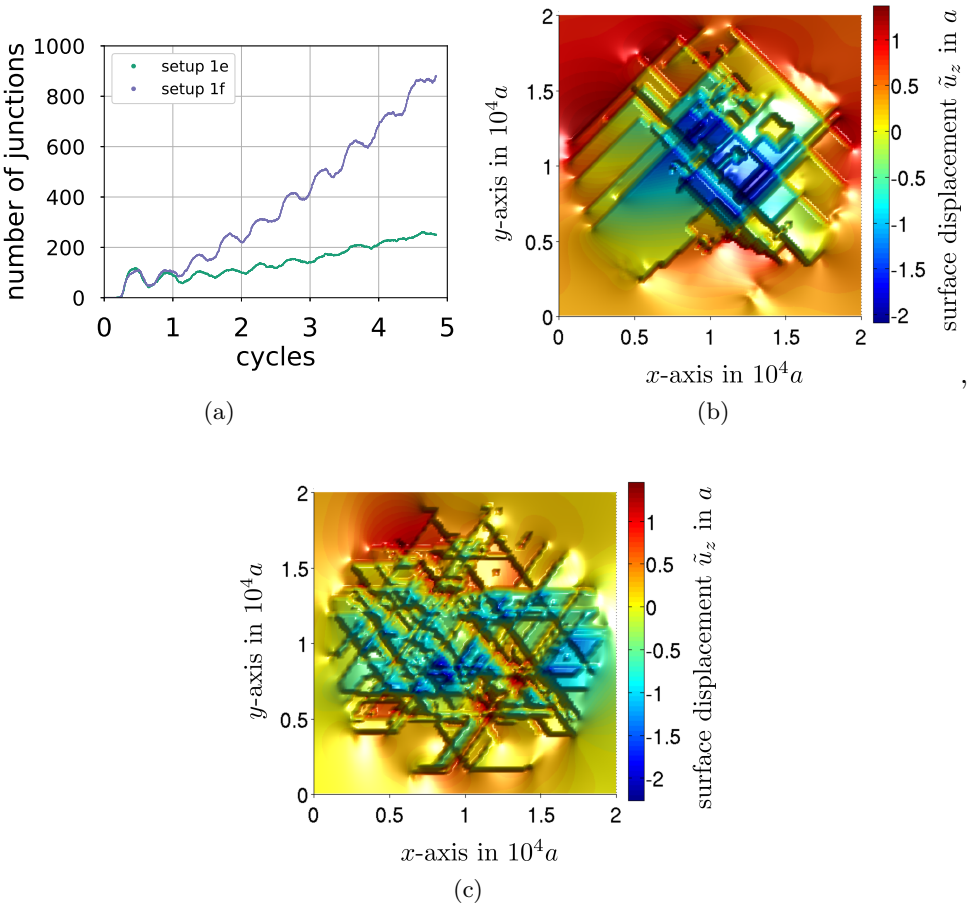

Figure 3.10: (a) Comparison of the evolution of the number of Lomer junctions in the [010] crystal orientation for setups 1e and 1f. Contour plots of the plastic surface displacement after 4 cycles while unloaded for (b) setup 1e and (c) setup 1f (El-Achkar und Weygand, 2019).

respectively reached. The analysis includes an extensive characterization of the extracted microstructural defects, which has partly been measured by experiments. The goal is to qualitatively understand, how microstructural features change upon changing the loading amplitude and compare the observations with experimental data.

The dislocation density evolution is fitted using a straight line and its slope is plotted against the imposed amplitudes in figure 3.12. From an amplitude of 0.002% and up to 0.01% the slope shows an almost linear regime. Below 0.002%, the slope curve kinks and the value reaches approximately zero for $\Delta\varepsilon_{\mathrm{pl}}/2 = 0.001\%$. The error bars, which indicate standard deviation, increase with plastic strain amplitude. In the following, a detailed microstructural comparison for $\Delta\varepsilon_{\mathrm{pl}}/2 = 0.001\%$ and

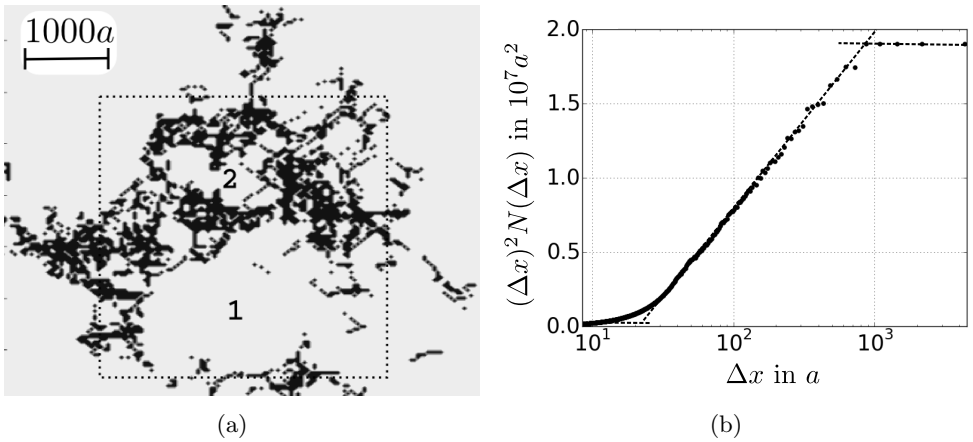

(a) (b)

Figure 3.11: (a) Evolved cell structure of setup 1e (table 3.1) in a TEM-like slice perpendicular to the [100] direction. (b) Box-counting technique (Hähner et al., 1998a) applied to the dotted region in (a). Δx is the box side-length and $N(\Delta x)$ the number of boxes containing a dislocation. (El-Achkar und Weygand, 2019)

$\Delta\varepsilon_{\mathrm{pl}}/2 = 0.01\%$ is carried out. The latter will be referred to as small and large amplitudes respectively.

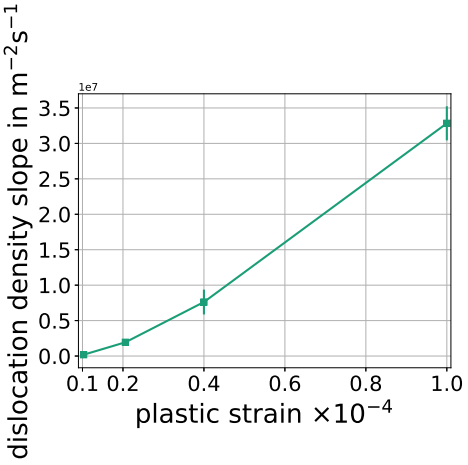

Figure 3.12: Linearly fitted dislocation density slope for various applied plastic strain amplitudes.

In figure 3.13, the stress-plastic strain curves for both amplitudes show hysteresis behavior. The stresses reach maximal absolute values at the imposed plastic strain amplitudes, where the loading rate changes sign. Due to the sudden change in loading direction the plastic strain is overshooting. With increasing number of cycles this overshoot decreases and the hysteresis shows a more stable shape. The difference in amplitudes is one order of magnitude, whereas the enclosed area of the larger amplitude is approximately five times larger than the one of the smaller amplitude.

The average plastic overshoot is $\Delta\varepsilon_{\mathrm{o,pl}} \approx 0.001\%$ and 0.005% for the small and large plastic strain amplitudes respectively. The width of the overshoot zone is $\approx 0.003\%$ plastic strain for both amplitudes.

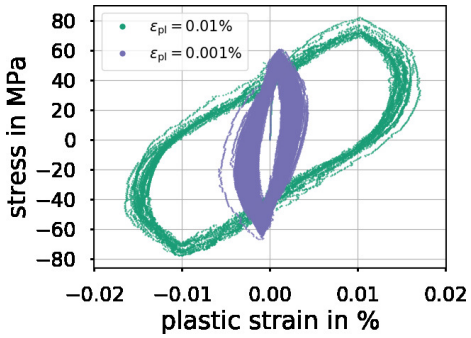

Figure 3.13: Stress versus plastic strain (El-Achkar und Weygand, 2019).

The dislocation microstructure evolution shows for both prescribed plastic strain amplitudes that plastic slip is at first mainly accommodated by the longest dislocations, whereas shorter dislocations act as barriers by forming junctions with mobile dislocations. However, significant qualitative differences in the microstructure are observed. Snapshots of the microstructure colored according to the number of graph components χ (section 2.2.1) are shown in figure 3.14, where dislocations colored in black belong to the largest component. For the plastic strain amplitude of $\Delta\varepsilon_{\mathrm{pl}}/2 = 0.01\%$, the dislocation density plot shows after 14 cycles a very stable large component alongside with numerous small components that are vastly prismatic loops and dislocation debris. The smaller amplitude $\Delta\varepsilon_{\mathrm{pl}}/2 = 0.001\%$ shows after about 10 times more cycles a low dislocation density and no clear structure formation. The number of components (figure 3.15) increases almost linearly with number of cycles, but the slope increases with increasing amplitude by a factor of 50.

For $\Delta\varepsilon_{\mathrm{pl}}/2 = 0.01\%$, the number of graph components for the dislocation network show rapid increase with a slope change after 6 cycles to reach almost 400 components after 16 cycles, whereas a rather slow evolution is observed for $\Delta\varepsilon_{\mathrm{pl}}/2 = 0.001\%$ leading to 140 components after 160 cycles. Furthermore, no saturation for the number of components in the investigated range is observed. Figure 3.16 shows the evolution of the fraction of the component density $\rho_{\mathrm{component}}$ with respect to the total dislocation density ρ_t for the largest three components. For $\Delta\varepsilon_{\mathrm{pl}}/2 = 0.01\%$ (figure 3.16(a)), the largest component constitutes, from the early stages and until the end of the simulation, the majority of the dislocation density and reaches a

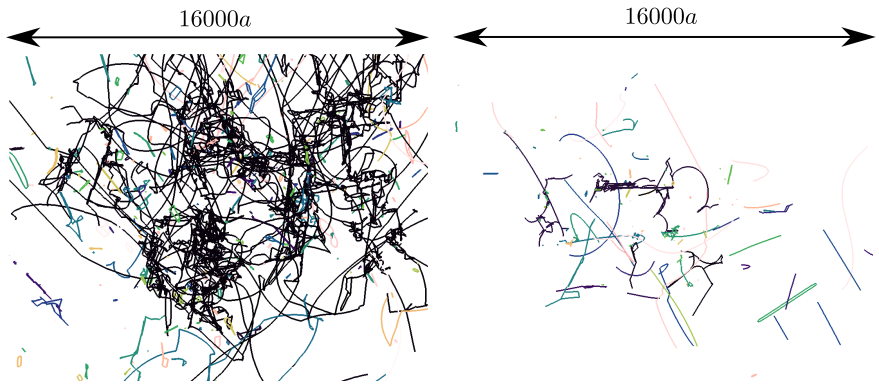

Figure 3.14: Visualization of spatial graph components χ for (a) $\Delta\varepsilon_{\mathrm{pl}}/2 = 0.01\%$ after 14 cycles and (b) $\Delta\varepsilon_{\mathrm{pl}}/2 = 0.001\%$ after 160 cycles while unloaded. The coloring corresponds to different components and black represents the largest component (El-Achkar und Weygand, 2019).

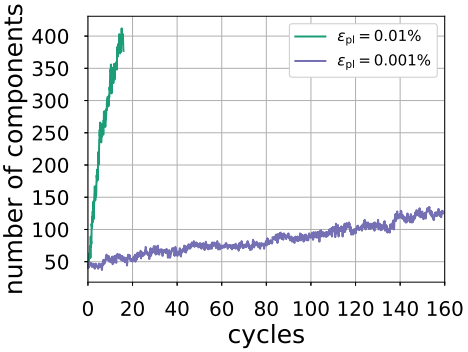

Figure 3.15: Evolution of the number of components (El-Achkar und Weygand, 2019).

saturation value of $\approx$ 70% of the total dislocation density after 6 cycles. The component density for $\Delta\varepsilon_{\mathrm{pl}}/2 = 0.001\%$ (figure 3.16(b)) shows rather comparable evolution for the largest three components in the early stages and a separation for the largest component after 70 cycles. The largest component fluctuates strongly and reaches peak values of up to 40% of the total dislocation density.

The evolution of the total dislocation density and dislocation character density are shown in figure 3.17. Dislocation character is binned according to $|\boldsymbol{e_b} \cdot \boldsymbol{e_t}| < 0.342$ for edge, $0.342 < |\boldsymbol{e_b} \cdot \boldsymbol{e_t}| < 0.9396$ for mixed and $|\boldsymbol{e_b} \cdot \boldsymbol{e_t}| > 0.9396$ for screw character. The dislocation density follows a similar two-slope regime as also seen in figure 3.15. For $\Delta\varepsilon_{\mathrm{pl}}/2 = 0.01\%$, the dislocation density reaches almost 16 times higher values than the initial density after 16 cycles while only 3 times higher values for $\Delta\varepsilon_{\mathrm{pl}}/2 = 0.001\%$ after 160 cycles. Compared to the dislocation density reached after one cycle, the final density for $\Delta\varepsilon_{\mathrm{pl}}/2 = 0.01\%$ is approximately three times

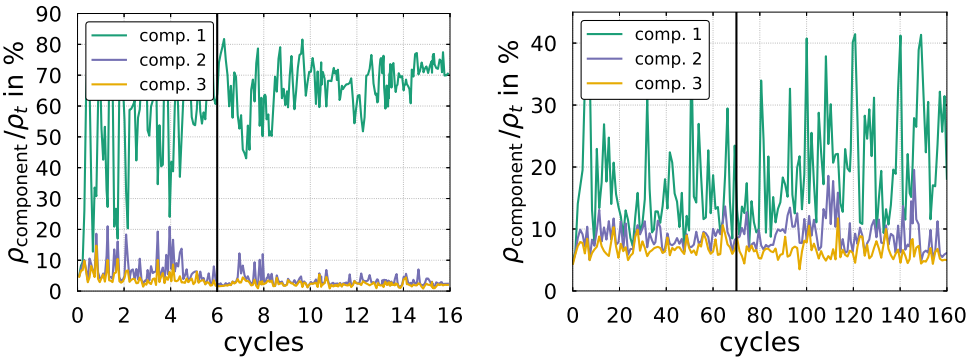

Figure 3.16: (a) Evolution of the fraction of dislocation density for the three largest components w.r.t. the total dislocation density for (a) $\Delta\varepsilon_{\text{pl}}/2 = 0.01\%$ and (b) $\Delta\varepsilon_{\text{pl}}/2 = 0.001\%$ (El-Achkar und Weygand, 2019).

higher. For $\Delta\varepsilon_{\text{pl}}/2 = 0.001\%$ an 1.2 fold increase is observed. The analysis of the dislocation character density shows that the density of screw dislocations is lowest and fluctuates around a constant value for the examined amplitudes. On the other hand, the density of mixed dislocations is highest and shows a trend similar to the total dislocation density. The edge dislocation density evolution is distinguishable from the rest, in early cycles it is almost equal to the screw density but after a critical number of cycles (6- and 70 cycles for $\Delta\varepsilon_{\text{pl}}/2 = 0.01\%$ and $\Delta\varepsilon_{\text{pl}}/2 = 0.001\%$ respectively) it shows an increase and separation from the screw dislocation density which is significant for $\Delta\varepsilon_{\text{pl}}/2 = 0.01\%$ but rather small for $\Delta\varepsilon_{\text{pl}}/2 = 0.001\%$.

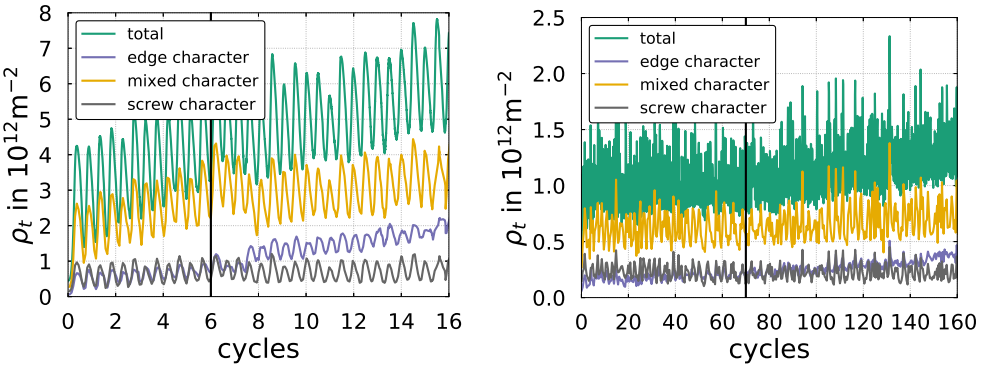

Figure 3.17: Evolution of the total dislocation density and character density for (a) $\Delta\varepsilon_{\text{pl}}/2 = 0.01\%$ and (b) $\Delta\varepsilon_{\text{pl}}/2 = 0.001\%$ (El-Achkar und Weygand, 2019).

The subsequent analysis is a detailed comparison at the level of physically-known irreversible defects such prismatic loops and dislocation dipoles. The number of

prismatic loops (figure 3.18) shows the same trend with respect to the slope change which was observed previously for the dislocation density as well as for component evolution. At the end of the simulation, the total number of prismatic loops for $\Delta\varepsilon_{\mathrm{pl}}/2 = 0.01\%$ is around 320 after 16 cycles and almost four times higher than for $\Delta\varepsilon_{\mathrm{pl}}/2 = 0.001\%$, where around 80 after 160 cycles are found and no saturation is observed for this value. The larger amplitude shows for the early stages that prismatic loops of the 1$^{\mathrm{st}}$ order are highest in number. After a critical number of cycles, the latter become similar in number to 2$^{\mathrm{nd}}$ order prismatic loops and dislocation debris. In the case of $\Delta\varepsilon_{\mathrm{pl}}/2 = 0.001\%$, the number of prismatic loops of 1$^{\mathrm{st}}$- and 2$^{\mathrm{nd}}$ order as well as dislocation debris evolve quite similar throughout the simulation. The evolution of the average shape of prismatic loops $< p_{\mathrm{shape}} >$

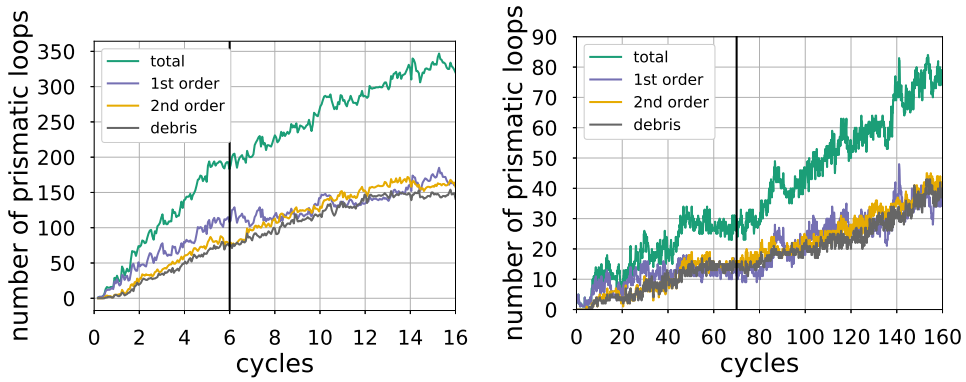

Figure 3.18: Evolution of the number of prismatic loops and dislocation debris for (a) $\Delta\varepsilon_{\mathrm{pl}}/2 = 0.01\%$ and (b) $\Delta\varepsilon_{\mathrm{pl}}/2 = 0.001\%$ (El-Achkar und Weygand, 2019).

during cycling is shown in figure 3.19(a). $< p_{\mathrm{shape}} >$ reaches a steady state value of 0.7 for the small amplitude after 20 cycles, while this value is smaller for the large amplitude in the early stages and reaches 0.75 at the end of the simulation. The distribution of p_{shape} (figures 3.19(b) and 3.19(c)) shows that elongated prismatic loops ($p_{\mathrm{shape}} < 1$) occur with a much higher probability for both amplitudes. With increasing number of cycles the maximum shifts from $p_{\mathrm{shape}} = 0.7$ to $p_{\mathrm{shape}} = 0.9$ for both amplitudes.

The distribution of the side length of the maximum loop extension (equations 2.17 and 2.18), which reflects the size of the evolved prismatic loops, is shown in figure 3.20. For both amplitudes, very small prismatic loops of side lengths $50a - 150\,a$ are found more frequently than large loops. This phenomenon is even more pronounced at later cycles, where a distinct maximum is visible for loops with maximum dimension of $50\,a$. Nevertheless, prismatic loops of maximum dimension larger than $500\,a$

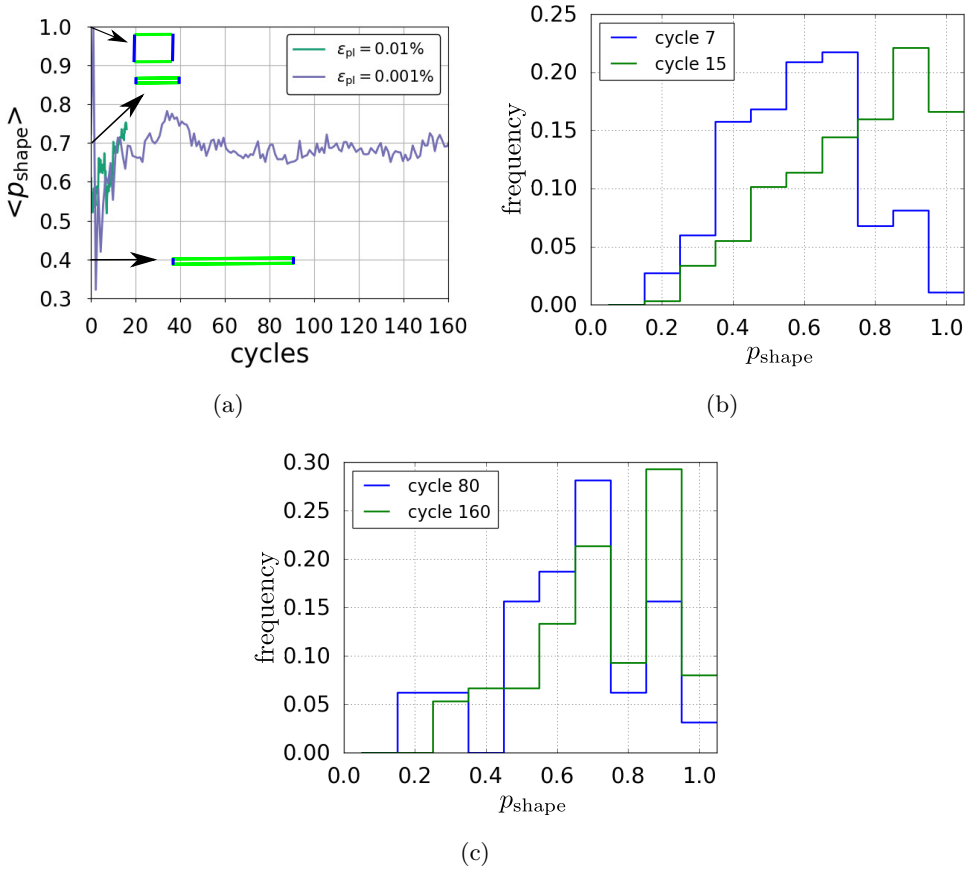

Figure 3.19: (a) Evolution of the mean prismatic shape p_{shape}. Distribution of the shape factor for (b) $\Delta\varepsilon_{\text{pl}}/2 = 0.01\%$ and (c) $\Delta\varepsilon_{\text{pl}}/2 = 0.001\%$ (El-Achkar und Weygand, 2019).

are also present. The investigation of dislocation dipoles by examining the mean dipolar height $< h >$ and length $< l >$ evolution (figures 3.21(a) and 3.22(a)) shows for $\Delta\varepsilon_{\text{pl}}/2 = 0.001\%$ in early cycles strong oscillations around the averaged values. Figure 3.21(a) shows that after approx. 20 cycles, $< h >$ stabilizes for the smaller amplitude around a value of $< h > \approx 38\,a$. This value varies early for the larger amplitude between $35a - 45\,a$ and increases to reach $< h > \approx 42\,a$ in the end of the simulation.

The frequency distribution of dipolar heights (figures 3.21(b) and 3.21(c)) shows an exponential distribution which can be fitted using $a/c_1 \exp(-(h - c_2)/c_1)$ with $c_2 = 11.5\,a$ and $c_1 = 24.8\,a$ respectively $c_1 = 30\,a$ for the large amplitude for cycles 7 and 15 respectively. The maximum dipolar height is located at the closest glide plane distance of $h = 11.8\,a$. For the small amplitude the fitting coefficients are $c_2 = 11.5\,a$ and $c_1 = 22.4\,a$ respectively $c_1 = 24.3\,a$ for cycles 80 and 160 respectively. Again, the height with the highest probability is very close to the smallest glide

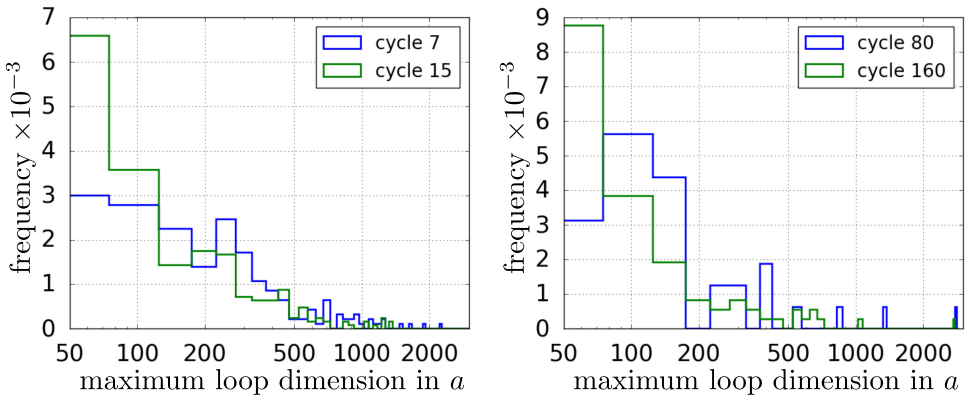

Figure 3.20: Distribution of the maximum loop dimension of prismatic loops for (a) $\Delta\varepsilon_{\mathrm{pl}}/2 = 0.01\%$ and (b) $\Delta\varepsilon_{\mathrm{pl}}/2 = 0.001\%$ (El-Achkar und Weygand, 2019).

plane distance. Increasing the number of cycles in both amplitude shows a decrease in the maximum values towards an increase in larger heights. The mean length of the dipoles $< l >$ (figure 3.22(a)) converges for both amplitudes towards a value of $< l > \approx 250\,a$. The frequency distribution of dipolar lengths (figures 3.22(b) and 3.22(c)) shows maximum values at $l = 200\,a$ for both amplitudes with a significant drop in this value afterwards. However, it is noticeable that long extended dipoles $l = 1000 - 2700\,a$ exist, although with a smaller frequency.

At a macroscopic level, the repeated forward and backward dislocation motion results in surface displacements, i.e. a surface roughness, part of which can be permanent (section 2.2.5). The surface topography, which is initially a flat surface, is represented by an equidistant grid with a spacing $\Delta = 156.25\,a$. At each grid point, the plastic surface displacement in z-direction $\tilde{u}_z$ is evaluated analytically in the post-processing stage. A developed sensitivity measure for surface evolution quantification is the maximum value of $||\nabla\tilde{u}_z||$ (figures 3.23(a) and 3.23(b)). The dotted orange line is a linear regression and shows for the large amplitude a fluctuation around a steadily increasing trend, whereas for the small amplitude it indicates a constant behavior. Nevertheless, a rise at 50 cycles followed by a drop to the initial value after 80 cycles is also observed for the small amplitude. The evolution of the distribution of the plastic surface displacement $\tilde{u}_z$ for different stages of unloading is shown in figures 3.23(c) and 3.23(d). For the large amplitude, fitting the distribution to a normal distribution yields mean and standard deviation values (in units of a) of $(0.26, 0.58)$, $(0.24, 0.68)$ and $(0.4, 0.75)$ for cycles 2, 7 and 14 respectively. The maximum value, which is located at zero for the second cycle, is shifted to higher values upon increasing the number of cycles. Additionally, values of $\tilde{u}_z = -2.5\,a$

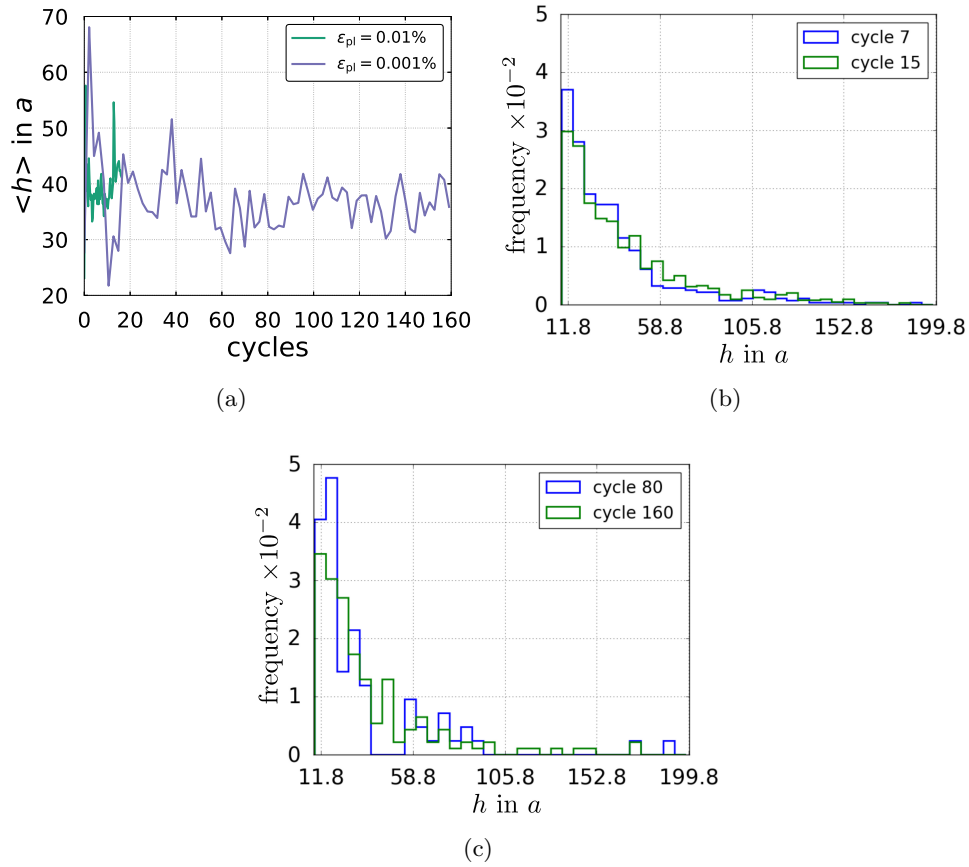

Figure 3.21: (a) Evolution of the mean dipolar height. Dipolar height distribution for (b) $\Delta\varepsilon_{\mathrm{pl}}/2 = 0.01\%$ and (c) $\Delta\varepsilon_{\mathrm{pl}}/2 = 0.001\%$ (El-Achkar und Weygand, 2019).

and $\tilde{u}_z = 1.6\,a$ are observed after 14 cycles. On the other hand, the distribution of displacements for the small amplitude for cycles 49, 70 and 146 (figure 3.23(b)) shows rather tight distributions located between $-0.4\,a$ and $0.4\,a$. After 49 cycles, the displacements are narrowed down to $0.05\,a$, $0\,a$ and $-0.05\,a$ in decreasing order respectively. A broader stair-case distribution is seen for 70 cycles for a maximum located at $-0.05\,a$. After 146 cycles, the displacements are extremely localized at $0.05\,a$ followed by smaller peaks at $0.1\,a$ and $0\,a$. A two-dimensional power spectrum visualization of both surfaces compared to other orientations is shown in figure H.2.

The extension of surface analysis is the irreversibility p factor (section 2.2.5). In figures 3.24(a) and 3.24(b), the evolution of p is shown for both amplitudes using surface- (equation 2.23) and bulk (equation 2.24) evaluation. The dotted orange line represents the ratio of slopes of the irreversible plastic strain $\varepsilon_{\mathrm{pl,irre}}$ and the cumulative plastic strain $\varepsilon_{\mathrm{pl,cum}}$ using a linear fit (figure H.1). It is evident that

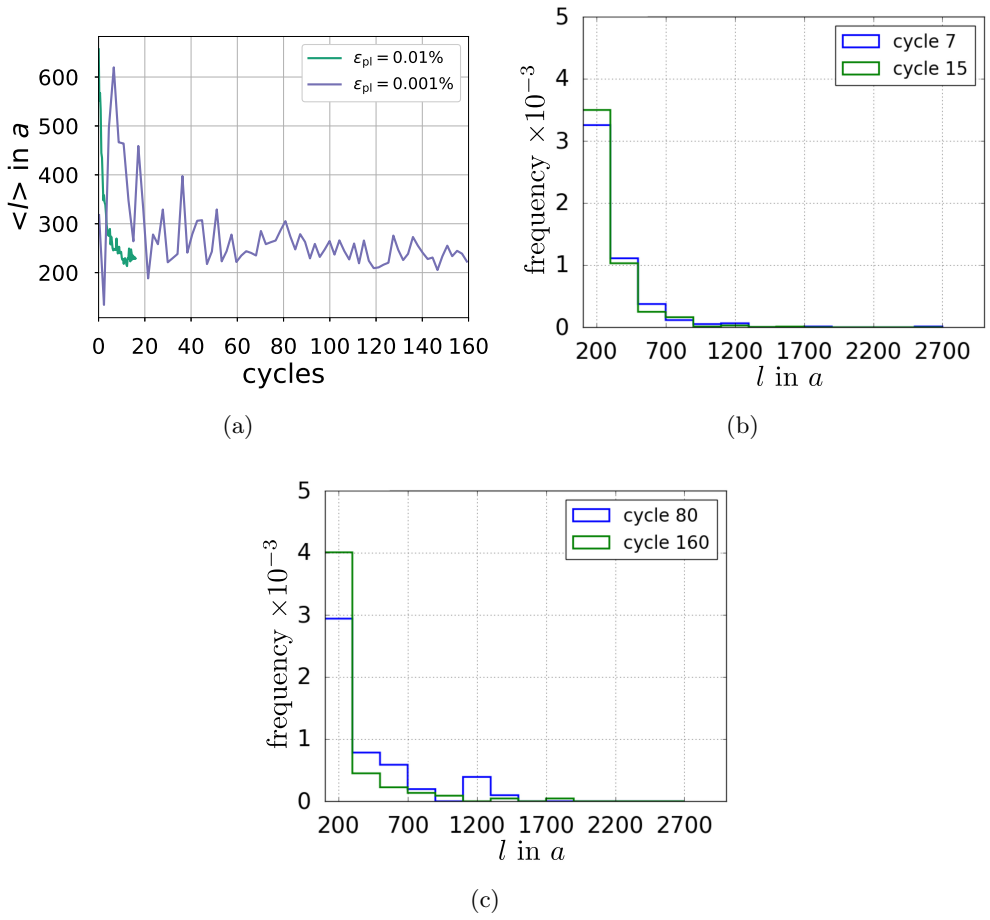

Figure 3.22: (a) Evolution of the mean dipolar length. Dipolar length distribution for (b) $\Delta\varepsilon_{\mathrm{pl}}/2 = 0.01\%$ and (c) $\Delta\varepsilon_{\mathrm{pl}}/2 = 0.001\%$ (El-Achkar und Weygand, 2019).

both surface and bulk measures decrease with number of cycles and the bulk p asymptotically approaches the slope line. Both setups show that p-surface is smaller than p-bulk and that the ratio of p-surface to p-bulk is 10 respectively 2 for the small- and large amplitude. p values for amplitudes from figure 3.12 are visualized alongside with experimental estimations for Cu and α-iron (Mughrabi, 2009) in a logarithmic plot (figure 3.24(c)). To mimic copper, an additional setup is included, for which screw dislocations can only cross-slip if the shear stress on the cross-slip plane is 50% higher than on the primary plane ($\tau_{\mathrm{cs}} > 1.5\tau_{\mathrm{primary}}$). Evident is that p-bulk values are higher than p obtained from surface measurements. The previously used cross-slip condition of 10% yields for the examined amplitude range fairly high p values when compared with Cu and α iron from experiments. When cross-slip is set to be more difficult (50%), then the curves shift downward, such that surface measurements become closer to experimental measurements of Cu.

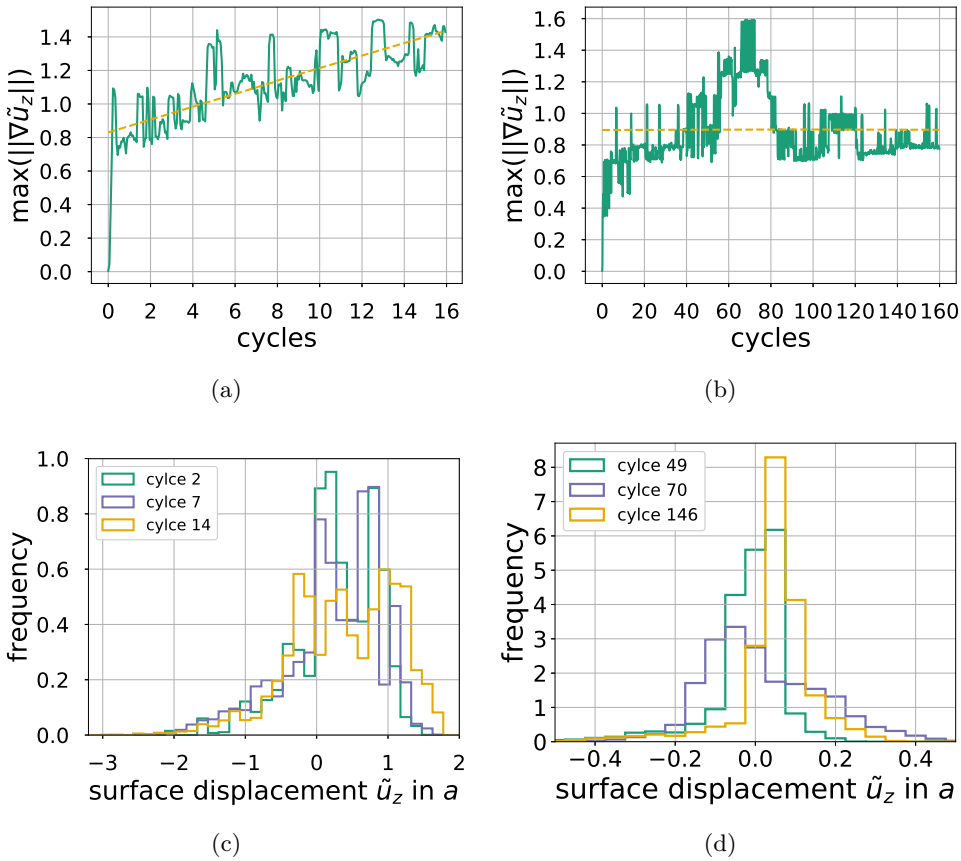

Figure 3.23: Evolution of the maximum value of $||\nabla \tilde{u}_z||$ for a grid resolution $\Delta = 156.25a$ for (a) $\Delta\varepsilon_{\mathrm{pl}}/2 = 0.01\%$ (El-Achkar und Weygand, 2019) and (b) $\Delta\varepsilon_{\mathrm{pl}}/2 = 0.001\%$. Distribution of the plastic surface displacement while unloaded for (c) $\Delta\varepsilon_{\mathrm{pl}}/2 = 0.01\%$ (El-Achkar und Weygand, 2019) and (d) $\Delta\varepsilon_{\mathrm{pl}}/2 = 0.001\%$.

3.1.2. [110]-tensile axis orientation

In setup 2a (table 3.2) the crystal orientation is chosen such that $\boldsymbol{e_{b4}}$ is in the direction of the tensile axis and $\boldsymbol{n_4}$ its complementary perpendicular axis along the x-direction (figure 3.25). The initial dislocation structure consists of FR sources of lengths 1000-5000 a embedded in the dodecahedron of figure 3.1(c) with the same boundary conditions as above and a plastic strain control cyclic loading with an amplitude of $\Delta\varepsilon_{\mathrm{pl}}/2 = 0.01\%$.

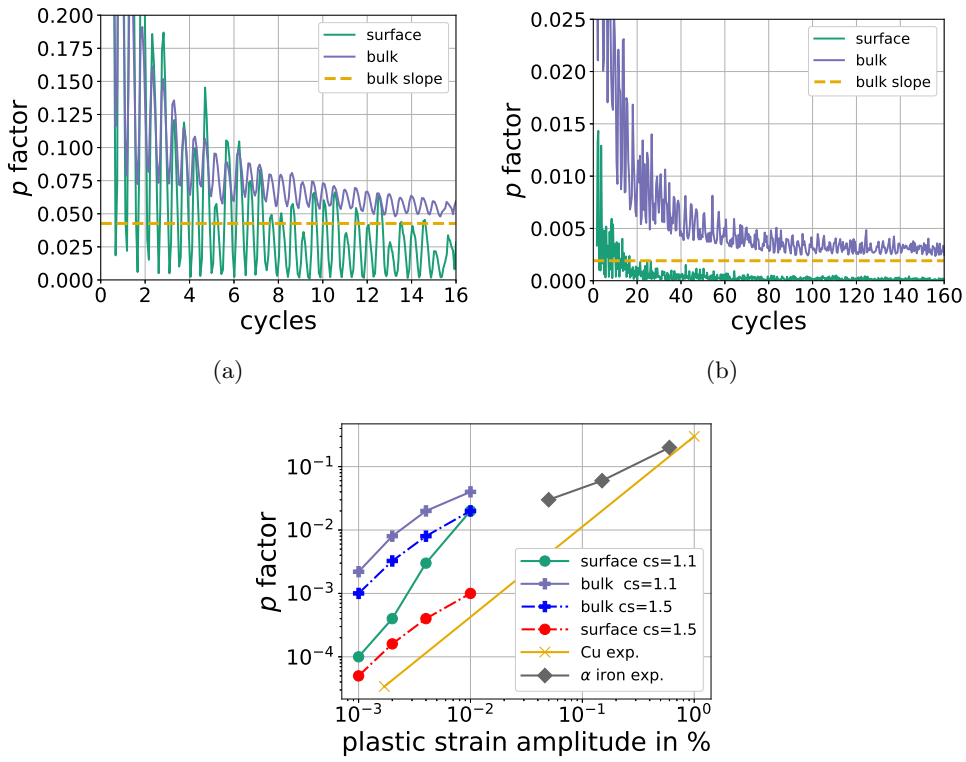

Figure 3.24: Evolution of the irreversibility factor p for (a) $\Delta\varepsilon_{\mathrm{pl}}/2 = 0.01\%$ and (b) $\Delta\varepsilon_{\mathrm{pl}}/2 = 0.001\%$. p is estimated from the surface and the bulk using equations 2.23 and 2.24 respectively. (c) p factor for experimental results for Cu and α-iron from Mughrabi (2009) alongside simulation results for the variation of cross-slip easiness such that cross-slip occurs if $\tau_{\mathrm{cs}} > 1.1\tau_{\mathrm{primary}}$ or $\tau_{\mathrm{cs}} > 1.5\tau_{\mathrm{primary}}$.

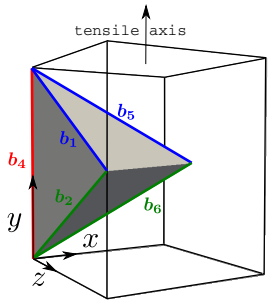

Figure 3.25: Setup 2a: [110] crystal orientation (El-Achkar und Weygand, 2019).

Pattern formation

The microstructure, during the simulation, is very distinct from the [010]-orientation. Dislocations arrange themselves into very stable bundles along the $\boldsymbol{e}_{\boldsymbol{b_3}} = 1/\sqrt{3}[\sqrt{2}01]$

Setup	Tensile axis y	Complementary axis x	Microstructure
2a	$\boldsymbol{e_{b_4}} = \frac{1}{\sqrt{2}}[110]$	$\bar{\boldsymbol{n}}_{\boldsymbol{4}} = \frac{1}{\sqrt{3}}(1\bar{1}1)$	random distribution of FR sources $\rho_t = 4.5 \times 10^{11}\mathrm{m}^{-2}$
2b	$\boldsymbol{e_{b_4}} = \frac{1}{\sqrt{2}}[110]$	$\boldsymbol{e_{b_3}} = \frac{1}{\sqrt{2}}[\bar{1}10]$	random distribution of FR sources $\rho_t = 4.5 \times 10^{11}\mathrm{m}^{-2}$
2c	$\boldsymbol{e_{b_4}} = \frac{1}{\sqrt{2}}[110]$	$\bar{\boldsymbol{n}}_{\boldsymbol{1}} = \frac{1}{\sqrt{3}}(\bar{1}11)$	random distribution of FR sources $\rho_t = 4.5 \times 10^{11}\mathrm{m}^{-2}$

Table 3.2: Setups' nomenclature for a [110]-tensile axis orientation.

direction (laboratory frame of reference) and accumulate with increasing number of cycles. These bundles are indicated by red numbers in figure 3.26(a). Figure 3.26(b) shows the mean pair correlation function (equation 2.19) characterizing the structure: Dislocations, which are aligned along $\boldsymbol{e_{b3}}$, are filtered out (section 2.2.4). The shell thickness and maximum radius are set to $dr = 30\,a$ and $r_{\max} = 4100\,a$ respectively. At very small distances, the mean pair correlation function shows a very high value followed by a drastic drop (figure 3.26(b)). Several well-defined peaks are also observed at $r \approx 700\,a$ and $r \approx 1800\,a$.

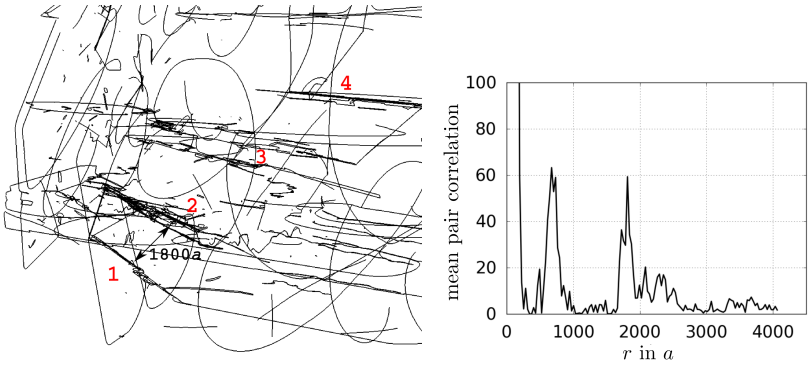

(a) (b)

Figure 3.26: (a) Slip band pattern formation in setup 2a [110] crystal orientation. The well-separated dislocation bundles are designated by red numbers from 1-4. (b) Mean pair correlation function for spatial analysis of the given structure in (a) (El-Achkar und Weygand, 2019).

The analysis of a different random initial configuration is shown in figure G.1 of the appendix. Evolution of the surface is provided in figure H.3 of the appendix.

Rotation around tensile axis

Two different setups are examined to demonstrate the influence of the rotation of the crystal system around the tensile axis (figure 3.27). In both setups the tensile axis is along $\boldsymbol{e_{b_4}}$ and $\boldsymbol{e_{b_3}}$ in setup 2b meaning that $\boldsymbol{b_1}$, $\boldsymbol{b_2}$, $\boldsymbol{b_5}$ and $\boldsymbol{b_6}$ are symmetric w.r.t. the free surface and in setup 2c $\boldsymbol{n_1} = (00\bar{1})$ such that $\boldsymbol{b_5}$ and $\boldsymbol{b_6}$ have a zero surface component (table 3.2).

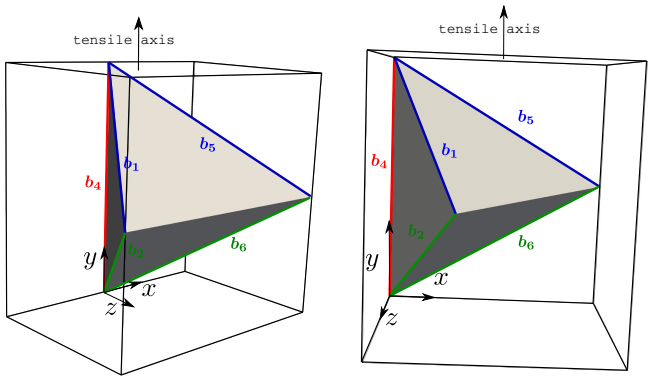

(a) (b)

Figure 3.27: Rotated [110] crystal orientations: (a) Setup 2b with $\boldsymbol{e_{b_4}} = [010]$ and $\boldsymbol{e_{b_3}} = [100]$, and (b) setup 2c with $\boldsymbol{e_{b_4}} = [010]$, $\boldsymbol{b_5}$ and $\boldsymbol{b_6}$ have no free surface component.

In figure 3.28 the final dislocation density distribution per glide system is shown for both setups. It is obvious that in setup II the dislocation density in glide system 4, 6, 7 and 9 belonging to Burgers vectors $\boldsymbol{b_1}$, $\boldsymbol{b_5}$, $\boldsymbol{b_2}$ and $\boldsymbol{b_6}$ respectively is equally distributed[2]. On the other hand, in setup III glide systems 4 and 7 ($\boldsymbol{b_1}$ and $\boldsymbol{b_2}$) show up to almost 1.8 times higher dislocation density on average than systems 6 and 9 ($\boldsymbol{b_5}$ and $\boldsymbol{b_6}$).

Surface contour plots of both setups are given in figures H.4 and H.5 of the appendix.

[2] Glide system numbering can be found in figure J.1 of the appendix

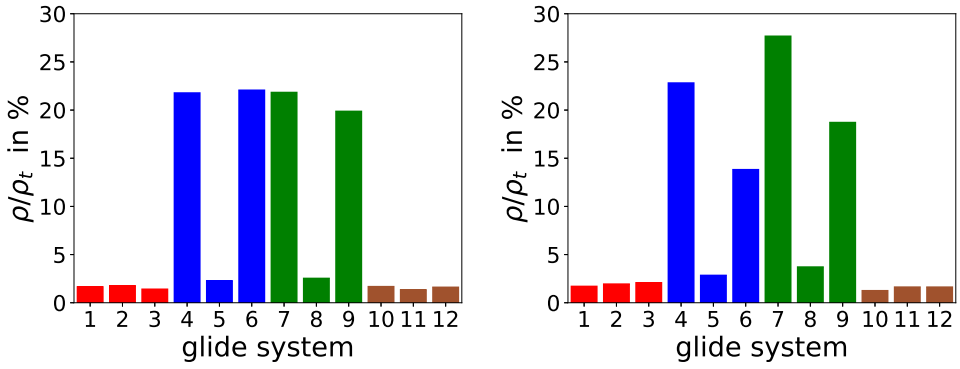

(a) (b)

Figure 3.28: Distribution of the fraction of the final dislocation density ρ per glide system w.r.t. the total dislocation density ρ_t for [110] crystal orientation setups (a) 2b and (b) 2c.

3.1.3. [982]-tensile axis orientation

The sensitivity of a 10 degree rotation away from the [110] crystal orientation is investigated. The tensile axis is chosen as [982] which is the y-axis in laboratory frame with $[\bar{2}21]$ pointing in x-direction. Glide system 9 (Burgers vector $\boldsymbol{b_6}$) experiences in this crystal orientation the maximum Schmid factor of 0.45. Eight different simulations of two different initial dislocation densities are conducted with an initial dislocation microstructure consisting of FR sources with lengths $4745\,a$. The sources are embedded in the dodecahedron of figure 3.1(c) with the same boundary conditions using several plastic strain amplitudes.

Full glide system simulation

In setup 3a, the initial microstructure consists of randomly distributed FR sources in all glide systems (table 3.3). Figure 3.29(a) shows the evolved microstructure after 10 cycles for an initial dislocation density $\rho_t = 4.5 \times 10^{11}\mathrm{m}^{-2}$ and applied plastic strain amplitude of $\Delta\varepsilon_{\mathrm{pl}}/2 = 0.01\%$. Obvious are several clusters of very small-size prismatic loops (shown in blue dotted squares) and several dislocation bundles aligned along $\boldsymbol{b_4}$. If compared to setup 2a for the pure [110] orientation microstructure (figure 3.26(a)), the structure shows no clear pattern and very little alignment along the main edge direction $[\bar{1}\bar{2}1]$ in the crystal frame with Burgers vector $\boldsymbol{b_6}$ (yellow solid line). The evolution of the surface of this setup is shown in figure H.6 of the appendix. Increasing the dislocation density by three (setup 3b in table 3.3) and keeping the same plastic strain amplitude shows a higher dislocation

Setup	Tensile axis y	Complementary axis x	Microstructure	Plastic strain amplitude
3a	[982]	[$\bar{2}$21]	random distribution of FR sources $\rho_t = 4.5 \times 10^{11}\mathrm{m}^{-2}$	$\Delta\varepsilon_{\mathrm{pl}}/2 = 0.01\%$
3b	[982]	[$\bar{2}$21]	random distribution of FR sources $\rho_t = 13.5 \times 10^{11}\mathrm{m}^{-2}$	$\Delta\varepsilon_{\mathrm{pl}}/2 = 0.01\%$
3c	[982]	[$\bar{2}$21]	random distribution of FR sources $\rho_t = 13.5 \times 10^{11}\mathrm{m}^{-2}$	$\Delta\varepsilon_{\mathrm{pl}}/2 = 0.084\%$
3d	[982]	[$\bar{2}$21]	54 dislocations in planes $\boldsymbol{n_3} = \frac{1}{\sqrt{3}}(\bar{1}\bar{1}1)$. 16 dislocations in the rest $\rho_t = 1.35 \times 10^{12}\mathrm{m}^{-2}$	$\Delta\varepsilon_{\mathrm{pl}}/2 = 0.01\%$
3e	[982]	[$\bar{2}$21]	random distribution of FR sources only in glide system 9 $\rho_t = 1.35 \times 10^{12}\mathrm{m}^{-2}$	$\Delta\varepsilon_{\mathrm{pl}}/2 = 0.084\%$

Table 3.3: Setups' nomenclature for a [982]-tensile axis orientation.

density with more dislocation bundles along $\boldsymbol{b_4}$ (green dotted region in figure 3.29(b)). The evolution of the dislocation density shows that the dislocation density is around only 1.3 times higher than the previous case despite the initial difference in density. In this setup, several dislocation dipoles and prismatic loops align along [$\bar{1}\bar{2}$1] and can be seen in the figure parallel to the yellow lines. The relaxation of the structure (figure 3.29(c)) preserves most of its constituents. On the other side, the increase of plastic strain strain amplitude by 8.4 (setup 3c in table 3.3) shows an extreme intensification of the $\boldsymbol{b_4}$-aligned dislocations alongside dislocations of all orientations (figure 3.29(d)).

Special glide system selection

Glide systems not belonging to glide system 9 with maximum Schmid factor are reduced in a two-step manner:

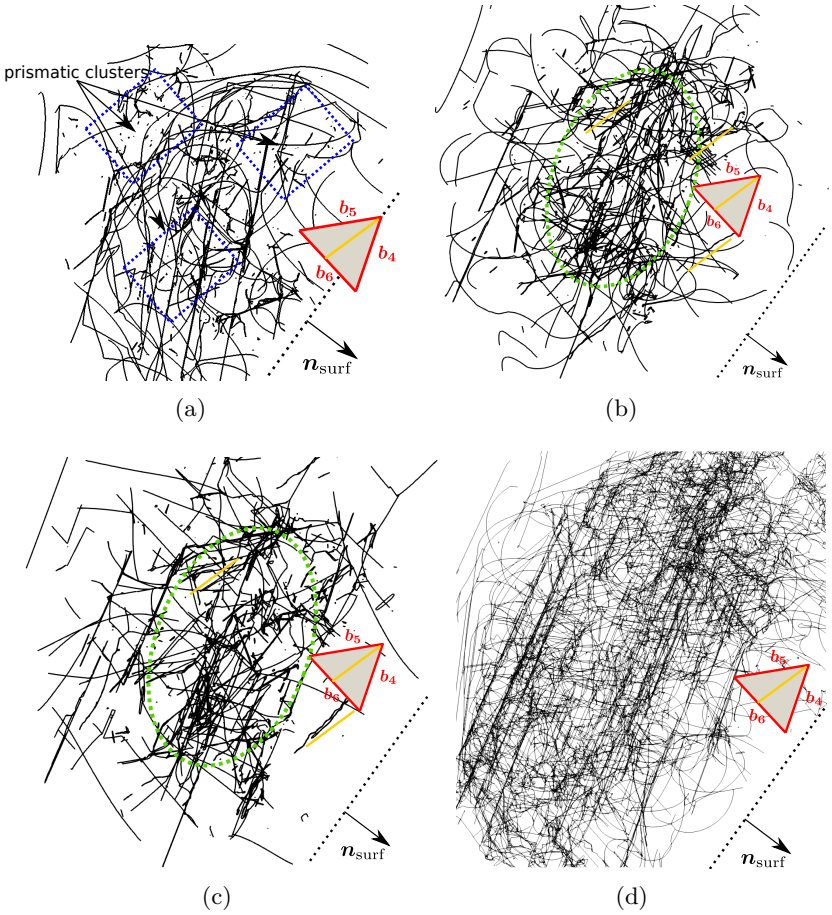

Figure 3.29: Dislocation microstructure of a [982] crystal orientation with all glide systems for a plastic strain amplitude of $\Delta\varepsilon_{pl}/2 = 0.01\%$ for (a) setup 3a with $\rho_t = 4.5\times10^{11}\mathrm{m}^{-2}$ after 10 cycles and (b-c) setup 3b with $\rho_t = 1.35\times10^{12}\mathrm{m}^{-2}$ after 8 cycles at load maximum and 9 cycles after relaxation respectively. (d) Microstructure for setup 3c a larger plastic strain amplitude of $\Delta\varepsilon_{pl}/2 = 0.084\%$ after 1 cycle. The blue regions indicate clusters of prismatic loops. The green ellipses contain dislocations that are aligned along $\boldsymbol{b_4}$ and the yellow solid lines represent directions along the $[\bar{1}\bar{2}1]$ direction.

- In setup 3d (table 3.3), the number of dislocations not belonging to the glide plane with normals vector $\boldsymbol{n_3}$, which contains glide system 9, is minimized. The initial dislocation density is $\rho_t = 1.35\times10^{12}\mathrm{m}^{-2}$ contains FR sources of lengths $4745\,a$ that are distributed in glide planes accordingly: 6 in $\boldsymbol{n_1}$, 6 in $\boldsymbol{n_2}$, 54 in $\boldsymbol{n_3}$ and 6 in $\boldsymbol{n_4}$. The plastic strain amplitude is $\Delta\varepsilon_{pl}/2 = 0.01\%$.

- In setup 3e (table 3.3), only glide system 9 with maximum Schmid factor is considered while other glide systems are discarded. The initial dislocation density is chosen as $\rho_t = 1.35\times10^{12}\mathrm{m}^{-2}$ and the applied plastic strain amplitude $\Delta\varepsilon_{pl}/2 = 0.084\%$. The latter is chosen higher than in setup 3d to ensure the

development of a pronounced pattern since only one glide system is involved, i.e. a reduction in junction types (only cross-slip and collinear are possible) ergo dislocation density compared to setup 3d .

Figure 3.30 shows the final dislocation microstructure. In setup 3d (figure 3.30(a)), numerous dislocation dipoles (yellow lines) appear alongside with dislocation alignment along $\boldsymbol{b_4}$ (as above). For setup 3e (figure 3.30(b)), pronounced dipolar bundles

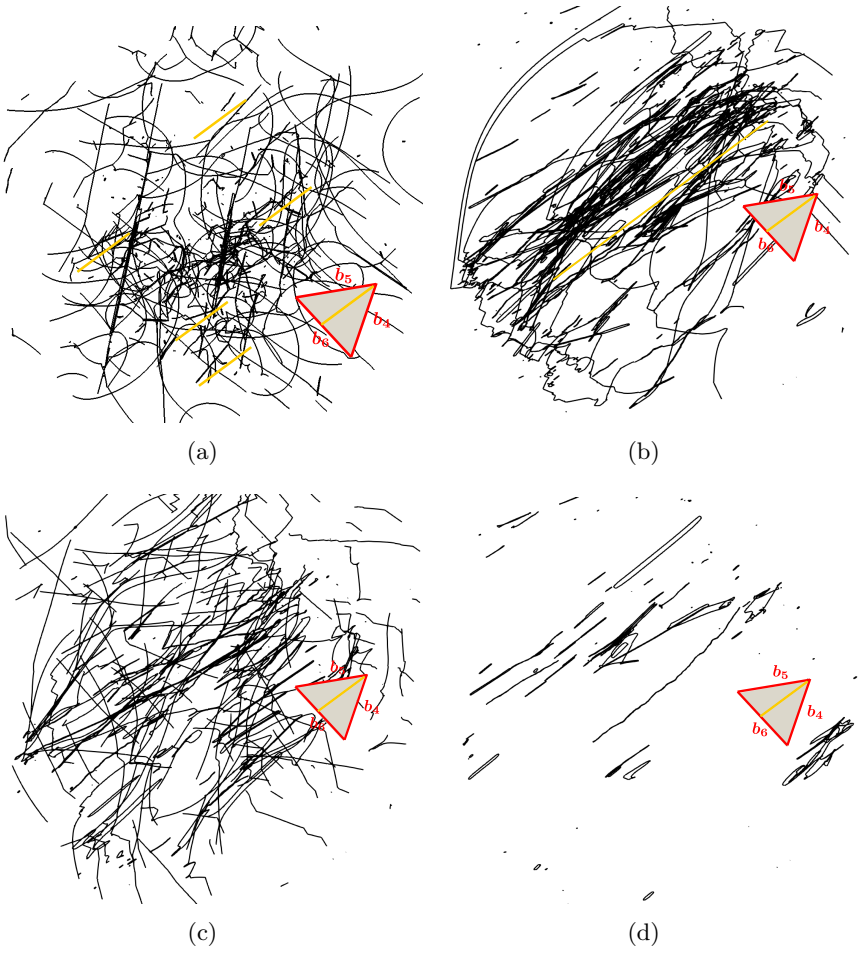

Figure 3.30: Microstructure of the [982] crystal orientation for (a) setup 3d (see text) after 17 cycles, (b) setup 3e after 3 cycles, (c) relaxing setup 3e and (d) removing the pinning restriction of the FR sources from (c) and connecting them.

appear and comprise nearly all the dislocation microstructure. Upon unloading and relaxation (figure 3.30(c)), the overall structural features are preserved, however, the dislocation density decreases up to almost 4.7 times. An extension of the relaxation is FR source removal. The latter is achieved by connecting the pinning points of the source to form a connected closed loop followed by unpinning the points. Figure 3.30(d) shows the microstructure if the process is carried out directly after the regular

relaxation process. The microstructure appears to be quite vacant and only several prismatic loops which are all aligned along $[\bar{1}\bar{2}1]$ are left.

The surface of the dipolar microstructure of setup 3e (magnified by a factor of 500) from figure 3.30(b) is shown in figure 3.31(a) with the microstructure underneath. It demonstrates well-defined embryonic extrusions along Burgers vector $\boldsymbol{b_6}$ with a rough central peak shown in figure 3.31(b). The location of the largest peak correlates

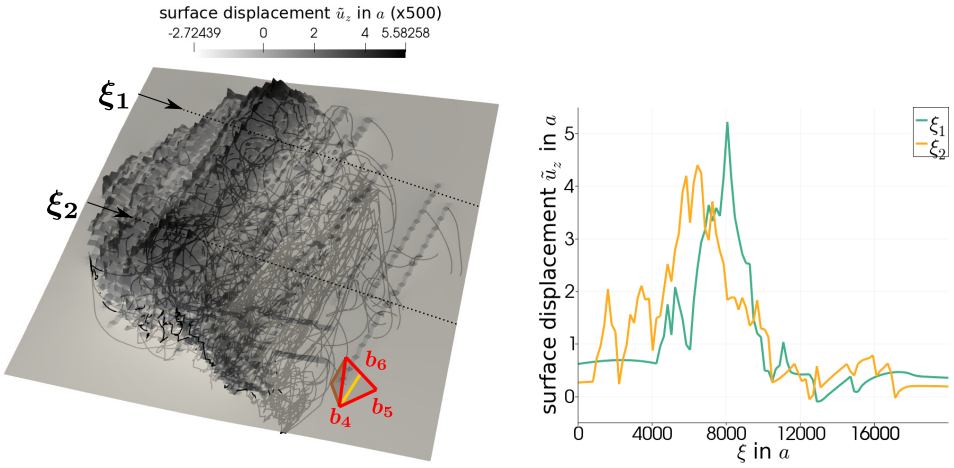

(a) (b)

Figure 3.31: (a) Magnified surface displacements of setup 3e after 3 cycles (unloaded) with the dislocation microstructure from figure 3.30(b) underneath. (b) Plot of the surface displacement along ξ_1 and ξ_2 from (a).

with the position of the highest density region from figure 3.30(b). The calculated irreversibility factor from the surface and bulk yields $p = 0.01$. Additional contour plots at load maxima can be seen in figure H.7 of the appendix.

3.2 Fatigue in *bcc* metals

The simulation model consists of a large spherical inclusion (compared to the simulation domain)[3] which mimics a non-metallic oxide with isotropic elastic material properties ($\mu_P = 154$ GPa and $\nu_P = 0.36$) embedded in a softer isotropic iron matrix ($a = 0.287496$ nm, $\mu = 77$ GPa and $\nu = 0.3$). The grid resolution in `ABAQUS` around the inclusion is chosen as $100a$. The remaining numerical parameters such as the mass per unit length m_0 and drag coefficient D are chosen as for *fcc*. The results below correspond to simulations of a single crystal and polycrystal.

[3] Depending on the heat treatment the size of, for example Al_2O_3 inclusions in a steel matrix SCM440, can vary between 8-33 μm (Jeddi und Palin-Luc, 2018).

3.2.1. Single crystal

The simulation domain consists of a cube of side length 7500 a, where an inclusion of radius R_p is embedded in the center. Dislocations can exit all the surfaces of the cube and cyclic tension and compression boundary conditions (as in section 3.1.1) using total strain control ($\dot{\varepsilon} = 5000\,\mathrm{s}^{-1}$) are applied to the top y surface.

[19$\bar{1}$]-tensile axis orientation

A double slip orientation [19$\bar{1}$], 9° away from [010], is chosen as the tensile axis (see figure 3.32). The dislocation microstructure consists of FR sources of lengths 1000 a such that the total dislocation density $\rho_t = 5.7 \times 10^{11}\mathrm{m}^{-2}$. All dislocations are populated in glide system 1 with the highest Schmid factor S and cycled under a total strain amplitude of 0.14%. The radius of the inclusion is set to a large value of $R_p = 2000\,a$ compared to the total volume ($\approx 1/12$). Using the commercial software `ABAQUS`, the elastic stress field $\boldsymbol{\sigma}^{\mathrm{el}}$ is calculated for each time step and stored so that it can be interpolated onto dislocations in the DDD part (section 2.1.4). The friction stress is chosen as $\tau' = 80$ MPa (section 2.1.5), slightly smaller than the critical bow-out radius of around 133 MPa. In Ashby und Johnson (1969) lower- and upper bounds are given for critical misfit values to nucleate a dislocation. Accordingly, the misfit strain is set as $e_C^* = 0.2\%$.

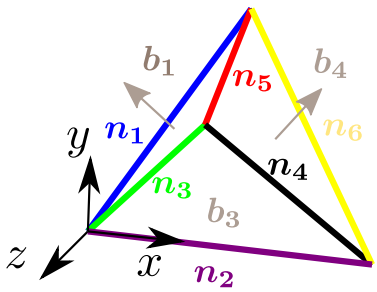

Figure 3.32: Inverted Thompson tetrahedron showing the [19$\bar{1}$]-tensile axis (y-direction) orientation.

Snapshots of the dislocation microstructure are shown for the first- and third cycle for load maximum in figure 3.33. The microstructure can be dissected into several components:

- Orowan loops winding around the inclusion which can be clearly seen in a section perpendicular to $\boldsymbol{n_1}$ (figure 3.33(b)).

- Elongated dipolar dislocations which extend from the inclusion to the free surface (figure 3.33(b)) and are marked as regions IV, V and VI in figure 3.33(c).
- Hexagonal prismatic loops that wrap around the inclusion and span all three glide planes can be seen in a section perpendicular to $\boldsymbol{b_1}$ in figure 3.33(a).
- Free prismatic loops such as region III in figure 3.33(c).
- Dipolar clusters seen in regions I and II in figure 3.33(c).
- Random dislocations which belong to screw and mixed types.

During the first three cycles, a dislocation density increase is observed which is associated with an increase in elongated dipolar dislocations and formation of dipolar clusters. A zoom into the clustered region (figure 3.33(e)) shows numerous numbers of prismatic loops of various shapes. Regions I and II (figure 3.33(c)) exhibit a symmetry with respect to a line passing through the inclusion center and parallel to the $\boldsymbol{b_1} \times \boldsymbol{n_3} = [\bar{2}\bar{1}1]$ direction. Figure 3.33(f) shows that the microstructure has a bias towards edge dislocations.

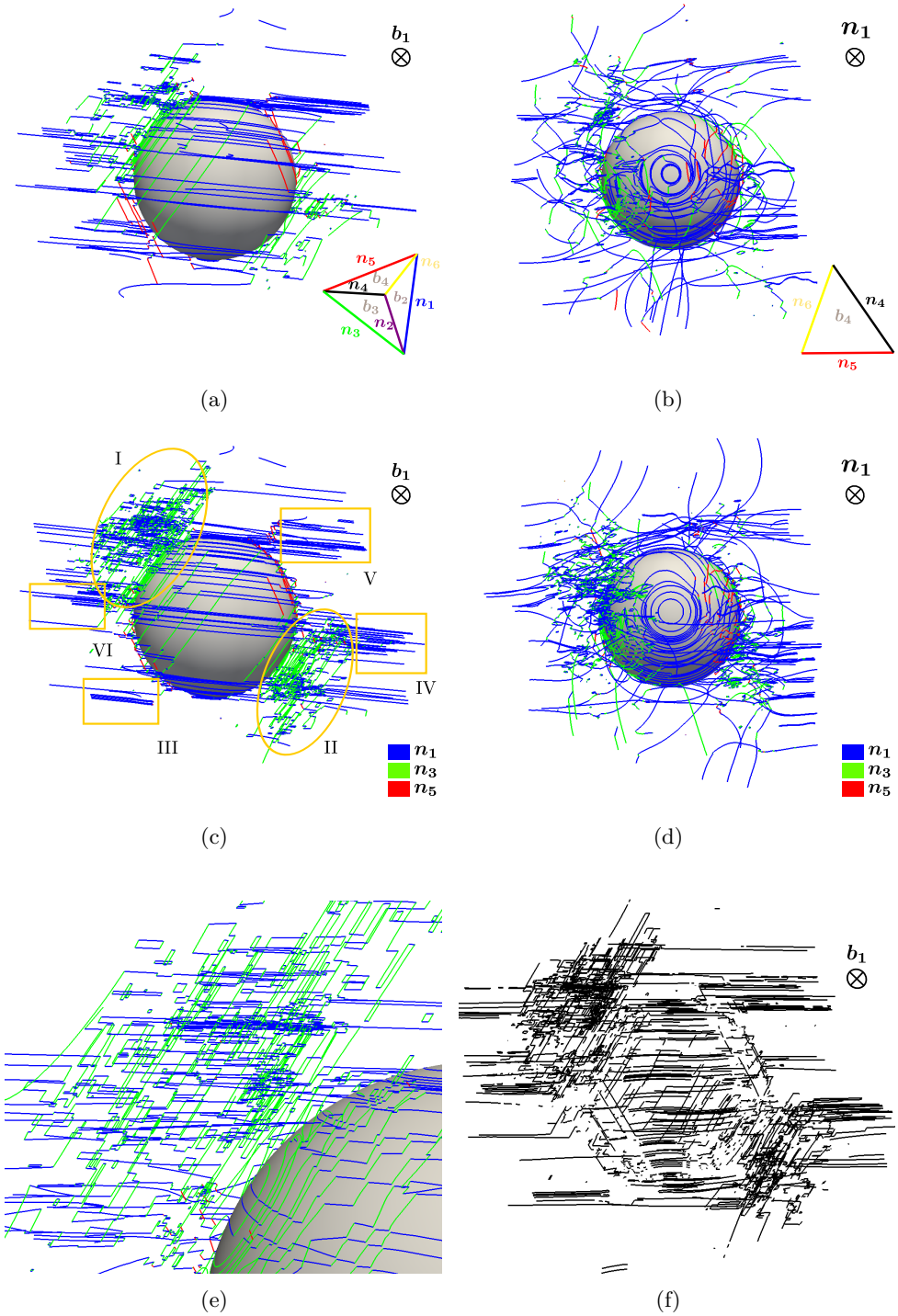

Figure 3.33: Evolved dislocation microstructure for a $[19\bar{1}]$ orientation for two different perspectives at load maximum in the (a-b) first cycle and (c-d) third cycle. (e) Magnification of zone I from (c). (f) Filtered microstructure from (c) according to edge type dislocations. Colors correspond to different glide planes (numbering is given in table J.1).

The analysis of volumetric von Mises plastic strain in voxels of side-lengths 500 a shows that plastic strain is highly localized in regions I and II (figure 3.34(a)). {112} sections of different depths (figures 3.34(b) and 3.34(c)) show that plastic strain extends throughout the whole volume in fine localized bands, while the rest of the volume shows only small values of plastic strain.

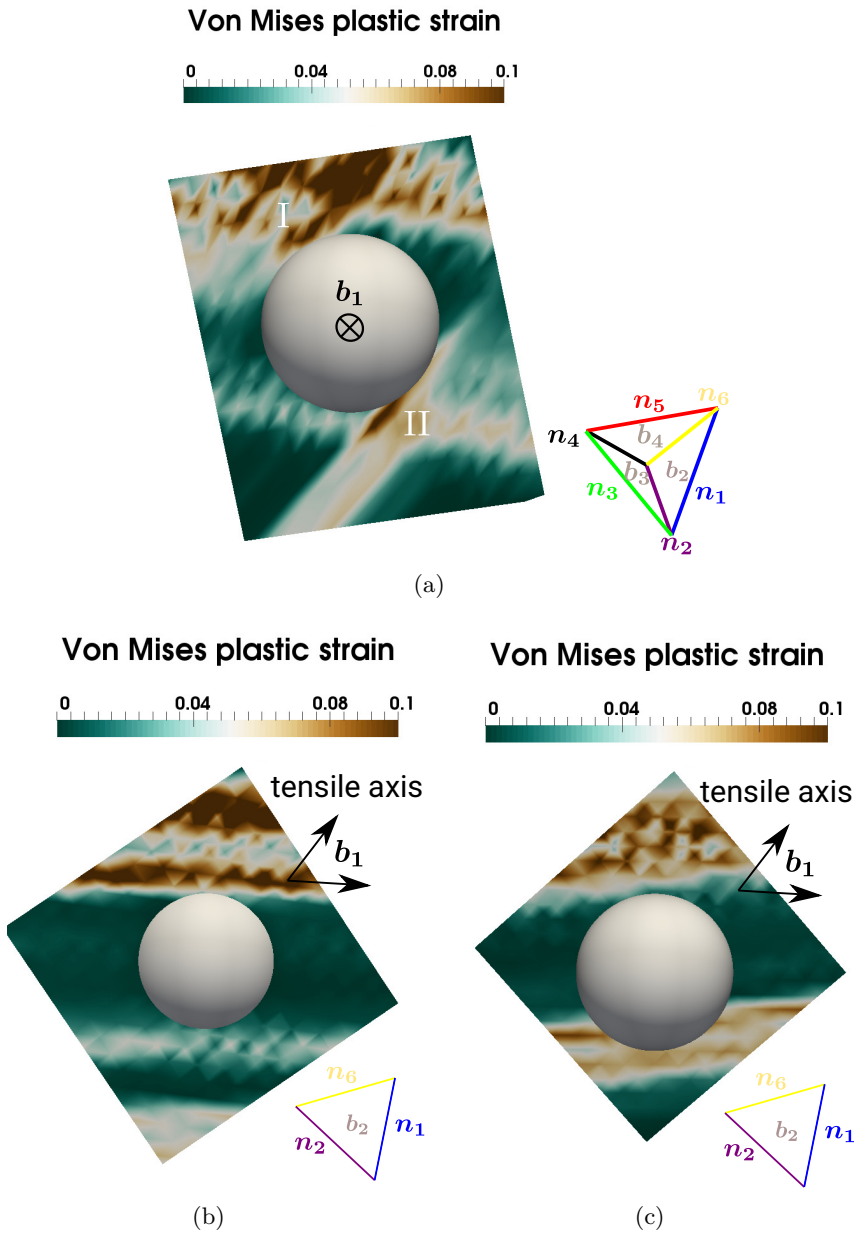

Figure 3.34: Distribution of the von Mises plastic strain at load maximum of the third cycle in (a) $\boldsymbol{b_1}$ and (b-c) {112} cross-sections. In (a) the cut is taken from the center of the volume. The planes' depths are 1800 a and −2000 a away from the center in (b) and (c) respectively. The voxel side-lengths for plastic strain evaluation are 500 a.

Investigation of the lattice misorientation angle ω_{mis} for the plastic rotation vector (calculation according to section K of the appendix) w.r.t. to a zero reference rotation shows in a section perpendicular to $\boldsymbol{b_1}$ highest misorientation $\omega_{\text{mis}} \approx 0.25°$ above and below the inclusion (figure 3.35(a)). In a {112} section (figure 3.35(b)), the largest values seen in figure 3.35(a) are found only in a small region. However, high ω_{mis} values are seen along $\boldsymbol{b_1}$ in a large area of approximately inclusion size which extend from one free surface to another.

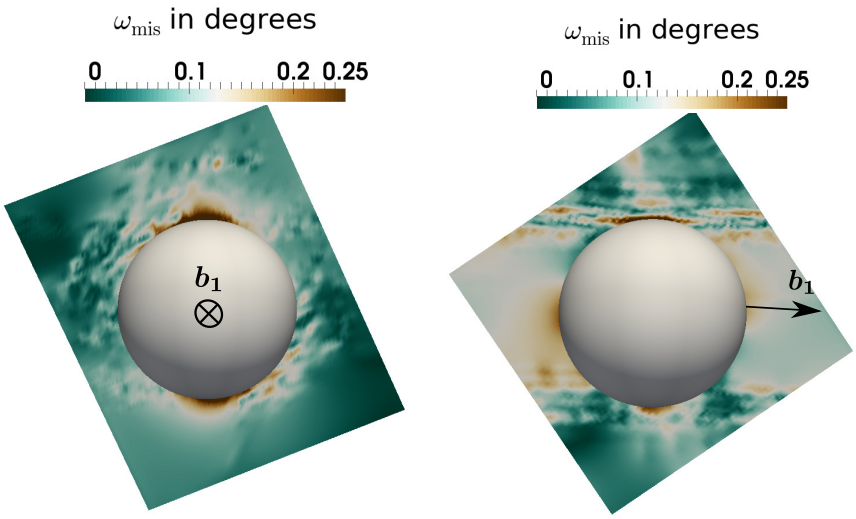

(a) (b)

Figure 3.35: (a) $\boldsymbol{b_1}$- and (b) {112} central cross-sections showing the misorientation angle ω_{mis} distribution. The voxel side-lengths for evaluation are $500\,a$.

Study of inclusion intrinsic properties The influence of the inclusion properties (section 2.1.4) on the development of the microstructure in figure 3.33 is studied. To magnify the effect of each property, several setups with individual inclusion attributes are simulated. In all setups, a single FR source of length $2000\,a$ with center coordinates $(6105, 3407, 5996)^{\mathrm{T}}\,a$ is inserted into an elastic cube of side-length $7500\,a$. An inclusion of radius $R_p = 2000\,a$ is embedded into the center of the domain and the total strain amplitude is set to $\Delta\varepsilon_{\text{tot}}/2 = 0.12\%$. The boundary conditions are the same as above. Since the friction stress is not an investigation parameter, it is set to a fairly low value of $\tau' = 20$ MPa (almost 3 times smaller than the critical bow-out radius) to accelerate the simulation.

The first study compares the behavior of two perfectly fitting isotropic spherical inclusions with one having the same material properties as the matrix and the other the different elastic constants $\mu_P = 154$ GPa and $\nu_P = 0.36$ (as above). Figure 3.36(a)

shows the dislocation density evolution as a function of cycles for both setups. It can be seen that the dislocation density is systematically higher for the setup with the modulus-induced stress field $\boldsymbol{\sigma}^{\mathrm{el}}$. Nonetheless, both setups show almost full reversibility of the dislocation density upon load reversal. For the applied strain amplitude, the obstacle hinders dislocation motion and leads to the formation of Orowan loops. Further dislocations arriving at the inclusion experience a pile-up stress leading to stresses higher in the cross-slip plane than in the primary plane, thus causing screw-type segments to cross-slip (figure 3.36(b)). The inclusion with different elastic properties than the matrix shows more Orowan loops and cross-slip events and the development of several prismatic loops (figure 3.36(c)).

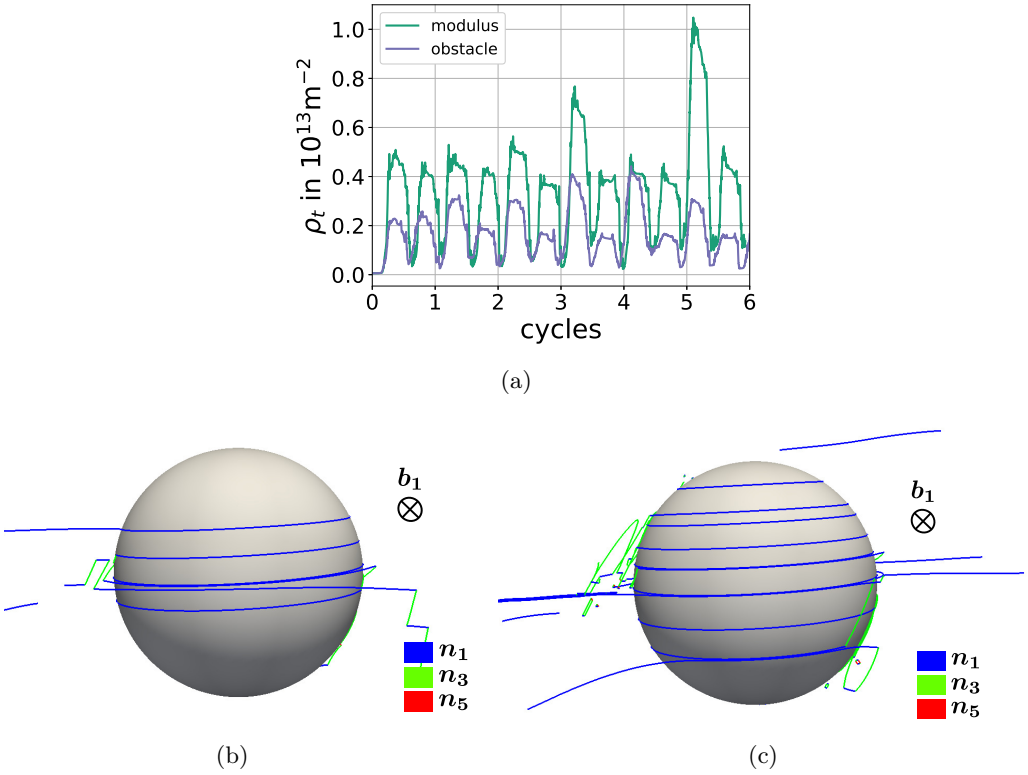

(a)

(b)

(c)

Figure 3.36: Comparison of the behavior of a spherical obstacle with that of an inclusion that has different elastic properties than the matrix. (a) Dislocation density evolution. Snapshots of the dislocation microstructure during the second cycle (maximum loading) for the (b) spherical obstacle and (c) the inclusion with the modulus-induced stress field $\boldsymbol{\sigma}^{\mathbf{el}}$. Colors correspond to different glide planes (numbering is given in table J.1).

In a third setup, the influence of three misfit strains $e_C^* = 0.1\%$, $e_C^* = 0.2\%$ and $e_C^* = 0.3\%$ is examined. Here the inclusion has the same elastic properties as the matrix. Figure 3.37(a) shows the evolution of the dislocation density for the setups. It is observed for all cases that the dislocation density ρ_t increases gradually and

barely decreases during unloading and that its magnitude is proportional to the misfit strain e_C^*. The developed dislocation microstructure of the three different misfit strain is shown in figures 3.37(b), 3.37(c) and 3.37(d). In contrast to the previous setups, the appearance of dislocations belonging to a third plane with normals $\boldsymbol{n_5}$ is visible with a fraction which increases upon increasing e_C^*. The dislocations form hexagonal prismatic loops that show extreme stability upon unloading.

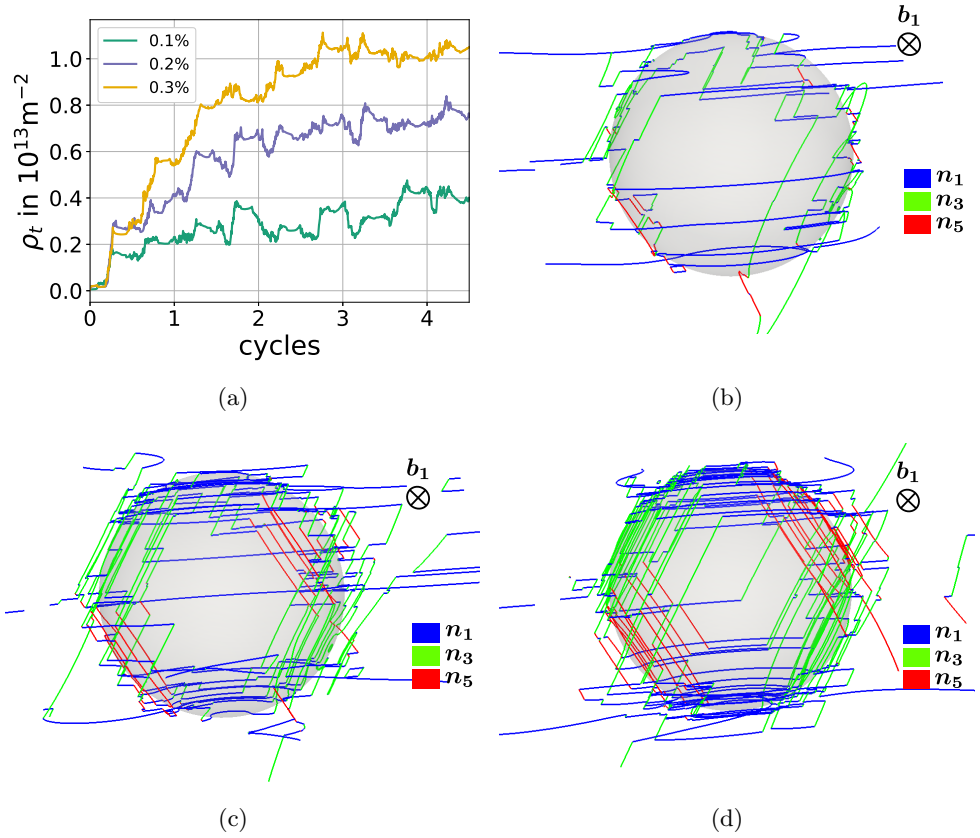

Figure 3.37: (a) Dislocation density evolution for a total strain controlled simulation with $\varepsilon_{\text{tot}} = 0.12\%$ for different misfit strains e_C^*. Snapshot of the microstructure in a section perpendicular to $\boldsymbol{b_1}$ after 4.5 cycles for (b) $e_C^* = 0.1\%$, (c) $e_C^* = 0.2\%$ and (d) $e_C^* = 0.3\%$. Colors correspond to different glide planes (numbering is given in table J.1).

To understand the formation of hexagonal prismatic loops, a simulation of the misfit stress field with no external stresses is performed. In the setup a smaller inclusion radius $R_p = 1250\,a$ with a very high misfit strain $e_C^* = 1.3\%$ (to activate a dislocation) is used. The microstructure consists of a single FR source of length $1000\,a$ belonging to glide system 10 ($\boldsymbol{b_4}$,$\boldsymbol{n_5}$) and positioned at a distance of $2450\,a$ away from the inclusion. The results show perfectly formed hexagonal prismatic loops (figure 3.38) which develop analogously to the Hirsch mechanism for *fcc*

materials (Humphreys und Hirsch, 1970) and similar to the ones previously observed in Munday et al. (2016).

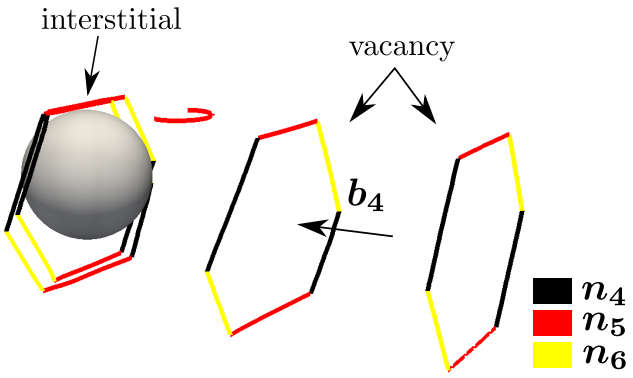

Figure 3.38: Formation of hexagonal prismatic loops of interstitial type, around an inclusion, and vacancy type which get repelled away.

Radius variation The previous simulations were performed for a constant inclusion radius and misfit. Figure 3.39 shows the dislocation density evolution for three different radii $R_p = 2000\,a$ (above simulation), $R_p = 1625\,a$ and $R_p = 1250\,a$ for $e_C^* = 0.2\%$ and $e_C^* = 0$. For an inclusion with no misfit, the dislocation density evolution is similar for the three examined radii and shows almost full reversibility upon unloading. On the other hand, for $e_C^* = 0.2\%$ the dislocation density for the smallest radius is even higher than for the largest radius without a misfit. The other two radii $R_p = 2000\,a$ and $R_p = 1625\,a$ show up to 3 times higher dislocation densities. It is observed that for a misfitting inclusion the dislocation density, depending on the radius, stays at a large value upon unloading.

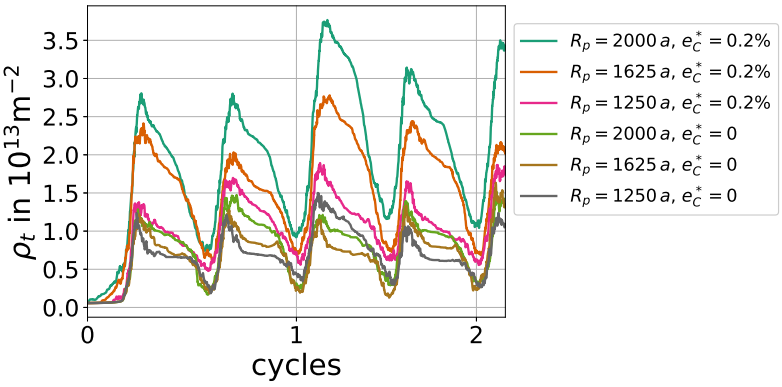

Figure 3.39: Comparison of the dislocation density evolution for different radii $R_p = 2000\,a$, $R_p = 1625\,a$ and $R_p = 1250\,a$ with- and without a misfit.

[010]-tensile axis orientation

To test the influence of other glide systems, a [010] multislip loading axis is used. All numerical parameters and boundary conditions are chosen as above with the only difference that all glide systems are included yielding a total dislocation density of $\rho_t = 10^{12}\mathrm{m}^{-2}$. For the above chosen total strain amplitude of 0.14%, the dislocation density during loading rapidly reaches $\rho_t = 8 \times 10^{13}\mathrm{m}^{-2}$ so that the simulation becomes very computationally expensive. Therefore, instead a slightly smaller strain amplitude of 0.12% is used.

The dislocation density evolution is shown until load maximum of compression of the first cycle in figure 3.40. Surprisingly, ρ_t remains constant after unloading and continues increasing during compression to reach $\rho_t = 7.5 \times 10^{13}\mathrm{m}^{-2}$ where it becomes very cumbersome to compute further steps of simulation. Microstructures for point A and B from the latter figure are shown in figure 3.41. The microstructure while unloaded (point A) is quite complex: a stable dislocation network development is observed on top- and left of the inclusion (figure 3.41(a)) which becomes denser during compression (figure 3.41(c)).

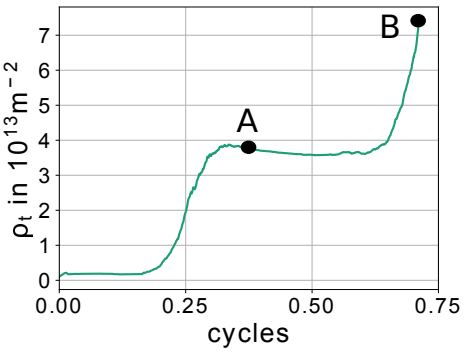

Figure 3.40: Dislocation density evolution in a [010]-tensile axis orientation using all glide systems.

3.2.2. Polycrystal

A polycrystal is modeled as an elastic cube of side-length 20000 a containing 64 grains and a spherical inclusion about twice as large in volume as a grain of radius $R_p = 4000\,a$ embedded at the center. The geometrical information of different grains is constructed using Voronoi Tesselation with the program `Voro++` (Rycroft, 2009). For each grain a random crystallographic orientation is chosen. The incorporation of grains into DDD is explained in section 2.1.3. The boundary conditions are shown

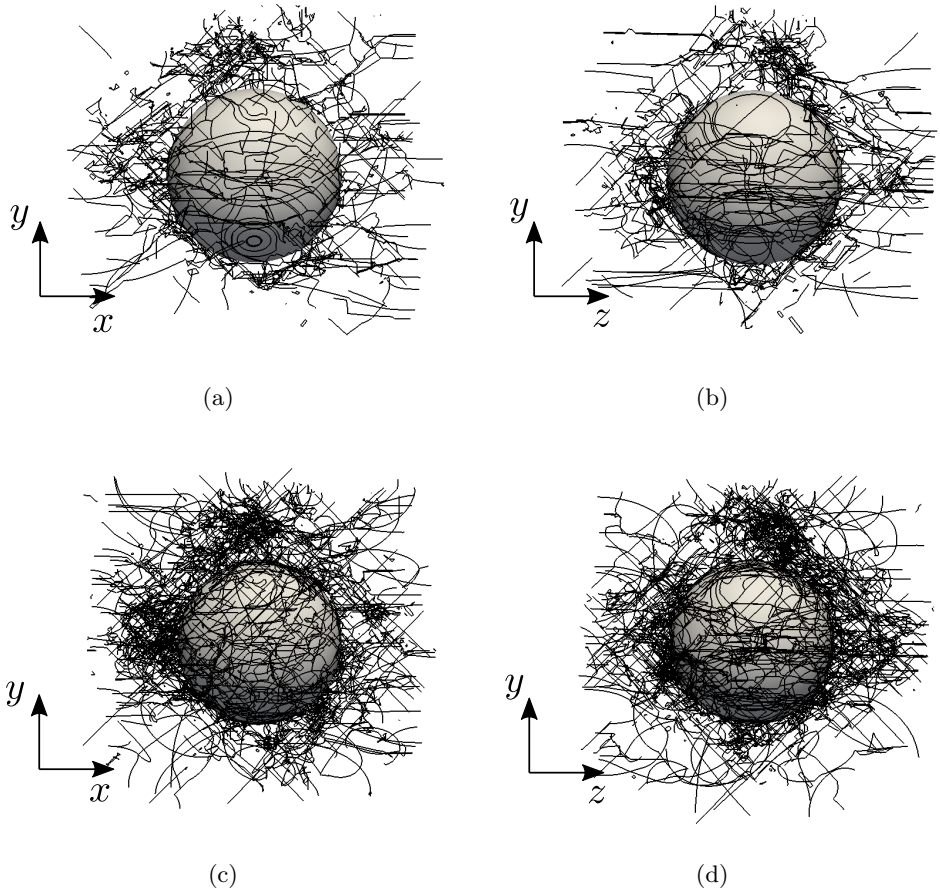

Figure 3.41: (a-d) Snapshots of the dislocation microstructure in a [010]-tensile axis orientation for points A and B (figure 3.40) for different perspectives.

in figure 3.42: The cyclic boundary condition of total strain amplitude 0.12% is applied to the top y-surface, whereas the bottom y surface is fixed at $u_y = 0$. The remaining degrees of freedom are traction free and dislocations can escape the volume from the cube outer surfaces. The initial dislocation microstructure consists of 375 dislocations of lengths $2000\,a$ which yield $\rho_t \approx 10^{12}\mathrm{m}^{-2}$. The misfit strain is chosen as $e_C^* = 0.2\%$.

At load maximum of the first cycle, most grains show dislocation pile-ups against grain boundaries with several cross-slip events (figure 3.43(a)). After three cycles, many dislocations far away from the inclusion have moved back. However, around the inclusion, several grains show a residual irreversible structure, which at this stage of cycling is still relatively small.

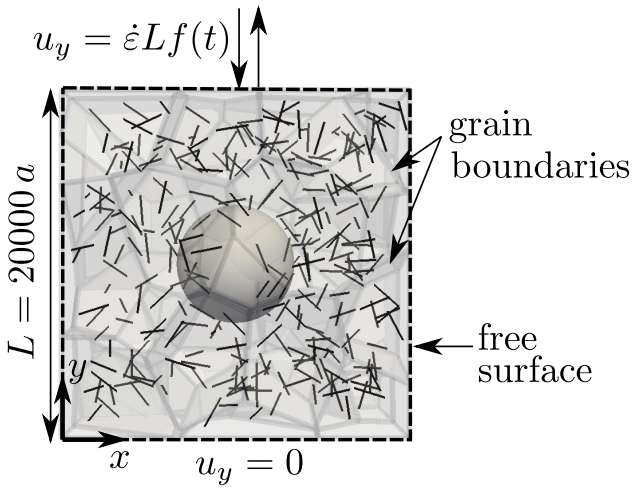

(a)

Figure 3.42: Initial- and boundary conditions of the simulated polycrystal.

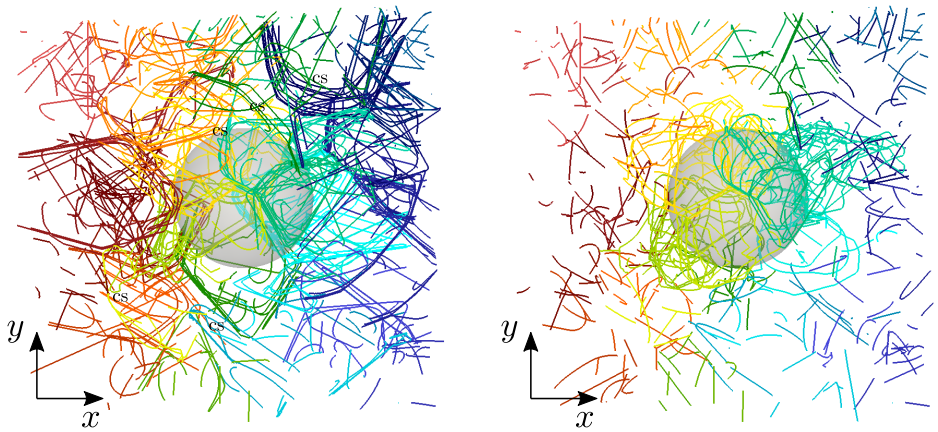

(a) (b)

Figure 3.43: Snapshot of the dislocation microstructure for the polycrystal (a) at load maximum of the first cycle (several selected cross-slip events are denoted to by cs) and (b) in the third cycle while unloaded (dislocation density minimum). Dislocations of the same grain obtain the same color.

For a detailed visualization of the irreversibility around the inclusion, the von Mises plastic strain is averaged in planes along the [001]-direction that are $63\,a$ apart. In figure 3.44(a) the plastic strain distribution is shown for the first three cycles during relaxation. Upon increasing the number of cycles, an obvious increase in plastic strain is observed for all cuts, especially for the ones in the direct vicinity of the inclusion (right and left) and ones located at the center of the inclusion showing

peak values. Similarly, the averaged dislocation density is plotted along z-planes in figure 3.44(b). Here the deviation of the dislocation density is even more pronounced around the inclusion domain when increasing the number of cycles.

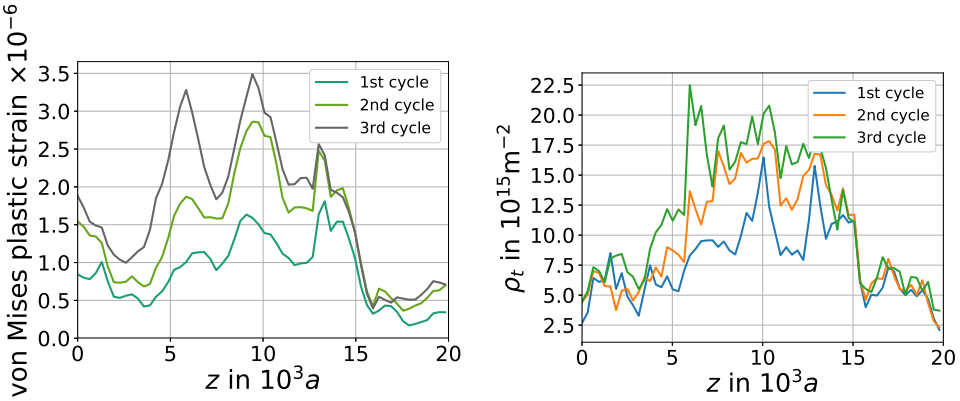

(a) (b)

Figure 3.44: Plot along [001] during relaxation of averaged (a) von Mises plastic strain and (b) dislocation density in z-planes (separation distance of 63 a).

The analysis of volumetric von Mises plastic strain using voxels of side-lengths 1250 a shows in central [100]-cuts grains that are highly active and result in significant plastic strain (figure 3.45). An asymmetry between grains that are active during tension and compression is visible and that plastic strain is rather continuous and penetrates through grain boundaries. For all stages of a cycle it can be seen that after increasing the number of cycles the area of plastic strain increases.

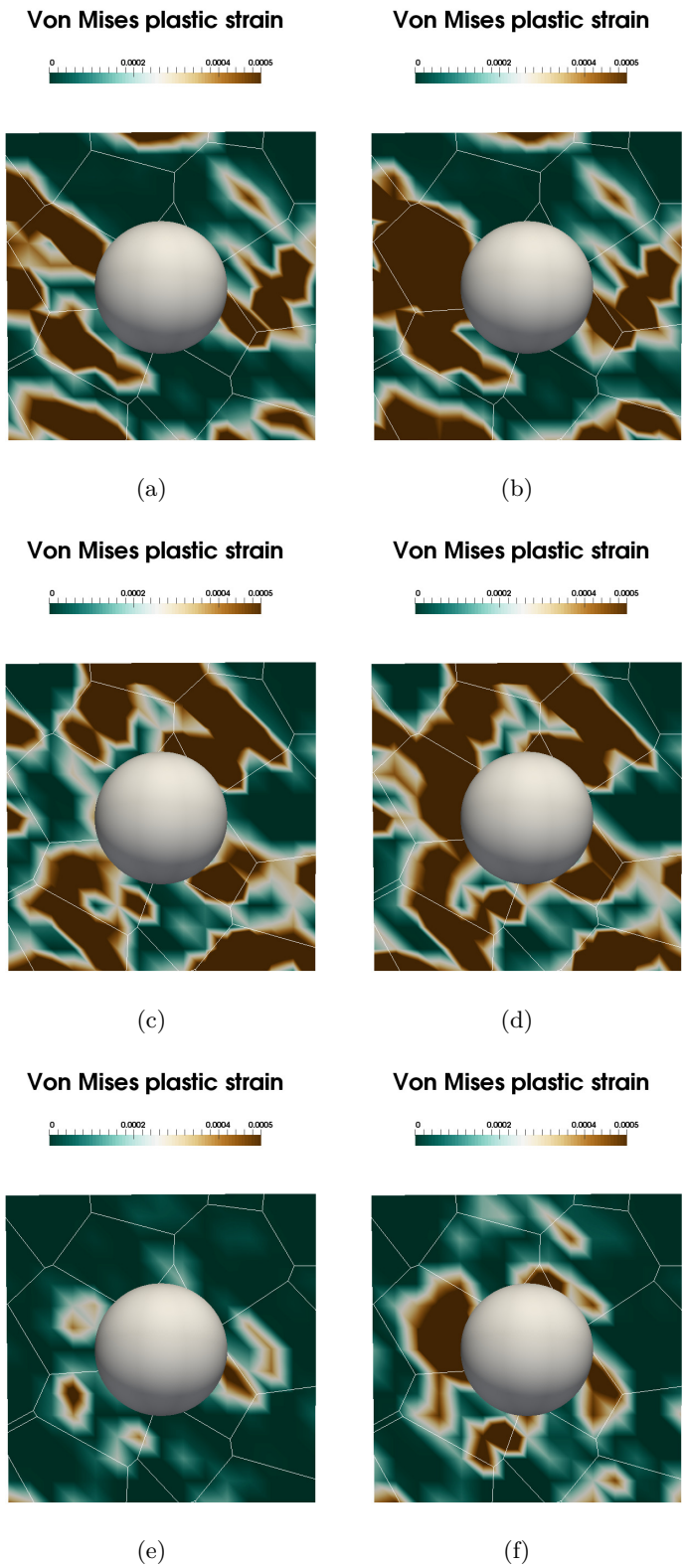

Figure 3.45: [100]-cuts taken from the center of the volumetric von Mises plastic strain using voxels of side-lengths $1250\,a$ for different stages of the first and third cycle: (a-b) maximum tension, (c-d) maximum compression and (e-f) relaxation after tension (dislocation density minimum). The white lines represent grain boundaries.

4. Discussion

4.1 Fatigue in *fcc* surface grains

4.1.1. Irreversibility as a consequence of grain shape and Burgers vector orientation

Grain morphology

The role of grain morphology is scrutinized in section 3.1.1 for a single FR source with Burgers vector orientation $\boldsymbol{b_1} = a/2[0\bar{1}1]$ which is embedded either in a cuboidal- (setup 1a) or truncated dodecahedral (setup 1c) surface grain (surface normal $\boldsymbol{n}_{\text{surf}} = [001]$) and the following observations are made:

- After the first bow-out of the initial FR source, cross-slip occurs at one grain boundary parallel to $\boldsymbol{b}$ in the truncated dodecahedral grain and at two grain boundaries in the cuboidal grain.
- Despite no significant differences when comparing dislocation densities, dislocation reactions consisting of cross-slip and collinear junctions are higher for the cuboid than for the dodecahedron (figure 3.2). The same trend can be seen for the number of prismatic loops which are almost 8 times higher for the cuboid. The same trend applies for the mean plastic strain which is 2-3 times smaller in the case of the dodecahedron.
- For the same initial- and boundary conditions a cuboidal bulk grain (setup 1d) behaves almost fully reversible (figure 3.3).

The orientation of grain boundaries with respect to the Burgers vector plays a crucial role in the irreversibility behavior of the dislocation microstructure. If multiple grain boundaries are oriented parallel to $\boldsymbol{b}$ then cross-slip can occur at these sites and result in a volume-spread microstructure with many reactions, prismatic loops and high plastic strain as seen for the cuboid. On the contrary, if grain boundaries

are hardly aligned along a screw orientation, then the microstructure is rather planar showing grain boundary pile-ups and strong reversibility. The high number of collinear reactions results in dislocation density annihilation and thus an almost equal dislocation density for the cuboid and dodecahedron. Since the number of cross-slip reactions is higher for the cuboid, the number of prismatic loops, which are formed frequently by the intersection of a cross-slipping dislocations with a dipole, is consequently higher.

Another important aspect is the vicinity of the grain w.r.t. the free surface. The simulation of a cuboidal bulk grain shows that due to the grain symmetry w.r.t. the crystal orientation the evolved microstructure leaves no irreversible parts when unloading. As a matter of fact, the forward and backward reversible dislocation motion is repeated in the simulated cycles in contrast to a surface grain. In the latter, dislocation loops can exit the surface, whereas their counter part can stay in the volume and leads in the unloading scenario to an asymmetry, i.e. irreversibility. This agrees with the fact that surface grains of ductile *fcc* metals are characteristic for crack initiation rather than bulk grains due to their high irreversibility (Mughrabi, 2009).

These findings reveal the three-dimensional nature of plastic irreversibility in grains, which should be taken into account in modeling aspects or for electron backscatter diffraction (EBSD) measurements in order to give a complete picture of fatigue damage.

Burgers vector orientation

Multislip orientations In a cuboidal surface grain (surface normal $\boldsymbol{n}_{\mathrm{surf}} = [001]$), the role of the initial Burgers vector orientation w.r.t. the free surface of a single FR source is investigated in section 3.1.1. The two examined cases are: setup 1a where $\boldsymbol{b_1} = a/2[0\bar{1}1]$ has a large surface component and setup 1b where $\boldsymbol{b_2} = a/2[110]$ has none (table 3.1).

Since $\boldsymbol{b_2}$ is parallel to the free surface, pile-ups only at one grain boundary parallel to the Burgers vector lead to numerous cross-slip events (figure 3.4). Although the dislocation density evolution for both setups is almost indistinguishable (figure 3.2), the number of prismatic loops for $\boldsymbol{b}$ parallel to the free surface are 2-3 times higher and the number of collinear reactions are up to 3 times higher than for $\boldsymbol{b}$ perpendicular to the free surface. This can be directly seen in the evolved microstructures in figure 3.4: Setup 1a ($\boldsymbol{b}$ has a large free surface component) shows a step-like structure, whereas setup 1b ($\boldsymbol{b}$ parallel to the free surface) is a localized structure which mostly consists

of prismatic loops of various sizes. Since prismatic loops move along a glide cylinder perpendicular to $\boldsymbol{b}$, almost half of the loops exit the free surface in setup 1a while most them remain in the volume in setup 1b. The large number of collinear reactions observed in setup 1b ($\boldsymbol{b}$ parallel to the free surface) is related to prismatic loop formation and annihilation that keeps the dislocation density almost equal when comparing the cases. The plastic strain distribution (figure 3.5) shows large values of plastic strain along channels of prismatic loops (along $\boldsymbol{b}$) and the spread-out strain in the volume in setup 1a compared to a localized distribution in setup 1b ($\boldsymbol{b}$ parallel to the free surface).

For the case where $\boldsymbol{b}$ has a large free surface component, prismatic loops that leave the free surface cause a roughening of the free surface (figures 3.6 and 3.7). The step-like nature of the surface in early cycles changes to a surface with sharp peaks that are located along prismatic channels along the Burgers vector. The RMS as well as minimum/maximum displacements show an increase during cycling which correlate well with the surface topology observed in the contour plots.

The observations agree with the Essmann-Gösele-Mughrabi (EGM) model (Essmann et al., 1981) that shows that extrusions appear in surface grains with Burgers vector orientation with a large surface component. On the other hand, interior grains with a Burgers vector parallel to the surface can nucleate a PSB which is unable to cross the grain boundaries.

The combination of all Burgers vectors in a [010]-tensile axis orientation using many initial FR sources (setup 1e in figure 3.9) shows three types of glide systems: those containing the largest dislocation density concentration which belong to Burgers vectors with a large free surface component ($\boldsymbol{b_2} = a/2[011]$ and $\boldsymbol{b_5} = a/2[01\bar{1}]$). These systems are followed by glide systems with a medium dislocation density belonging to Burgers vectors parallel to the free surface ($\boldsymbol{b_3} = a/2[\bar{1}10]$ and $\boldsymbol{b_4} = a/2[110]$). Both types of glide systems have an equivalent macroscopic Schmid factor of $S = 0.41$ and as seen before glide systems with $\boldsymbol{b}$ parallel to the free surface show even higher plastic activity than glide systems with $\boldsymbol{b}$ perpendicular to the free surface if treated individually (figure 3.2). Last but not least are glide systems ($\boldsymbol{b_1} = a/2[\bar{1}01]$ and $\boldsymbol{b_6} = a/2[101]$) which have a Schmid factor of $S = 0$ and are almost inactive. Nonetheless, when the crystal system is rotated about the tensile axis (figure 3.8), such that $\boldsymbol{b_2}$, $\boldsymbol{b_3}$, $\boldsymbol{b_4}$ and $\boldsymbol{b_5}$ are symmetric w.r.t. the free surface (setup 1f), then the dislocation density is almost equivalently distributed among the latter Burgers vectors that have $S = 0.41$. This leads to a higher number of Lomer junctions (figure 3.10) since all the glide systems required for the formation of $\boldsymbol{b_1}$- and $\boldsymbol{b_6}$ type junctions are involved (figure J.2 of the appendix). The rotation of the crystal

system also leads to different slip patterns on the free surface. The geometry of the markings can be directly correlated with the intersection of the crystal with the surface resulting in block-like structures or triangular patterns. Another consequence of the increased slip activity in this setup is a rougher surface.

To understand whether the observed glide system activity dependence on the Burgers vector's orientation w.r.t. free surface is a general property or a special feature of the examined geometry or cyclic load, a deeper analysis is conducted using four setups shown in figure 4.1: Cyclic loading of a fully embedded bulk truncated dodecahedron (figure 4.1(a)) and a cuboidal grain which has two free surfaces that are in z-direction (figure 4.1(b)), a tensile test of the dodecahedron studied above (figure 4.1(c)) and of a pillar with free surfaces (figure 4.1(d)). The dislocation density distributions are given in figure 4.2. Eliminating the free surface from the dodecahedron (figure 4.1(a)) results in an almost equal dislocation density distribution among glide systems with $S = 0.41$. An additional free surface (figure 4.1(b)) causes the dislocation density for glide systems, where $\boldsymbol{b}$ is parallel to the free surface and $S = 0.41$ to be negligible and reach a level similar to systems with $S = 0$, an indication that the effect is even magnified by introducing an extra free surface. A tensile test of the truncated dodecahedron with a free surface (figure 4.1(c)) shows a similar behavior as for cyclic loading (screenshots of the microstructures are given in figure M.1 of the appendix). The tensile loaded pillar (figure 4.1(d)) behaves as the cyclically loaded bulk grain.

Upon changing the tensile axis to [110] (section 3.1.2), the same behavior can be observed where the dislocation density is almost equally distributed among systems that are symmetric w.r.t. the free surface (setup 2b in figure 3.28) and drops in systems that a high Schmid factor but a zero surface component (setup 2c in figure 3.28).

This means that in multislip loading conditions in surface grains the distribution of dislocation density among glide systems is controlled by the orientation of the Burgers vector w.r.t. the free surface. It is a general feature of both monotonic and cyclic load (figure 4.2(c)) and can be amplified by introducing an additional free surface (figure 4.2(b)). The influence of the free surface w.r.t. to glide system activity can be also observed in a [210] double slip orientation (section E of the appendix).

The comprehension of the physical mechanism of the underlying phenomenon requires an investigation at the microstructural level. In this analysis, isolated simulations of separate dislocations with Burgers vectors $\boldsymbol{b_5} = a/2[01\bar{1}]$ (large surface component)

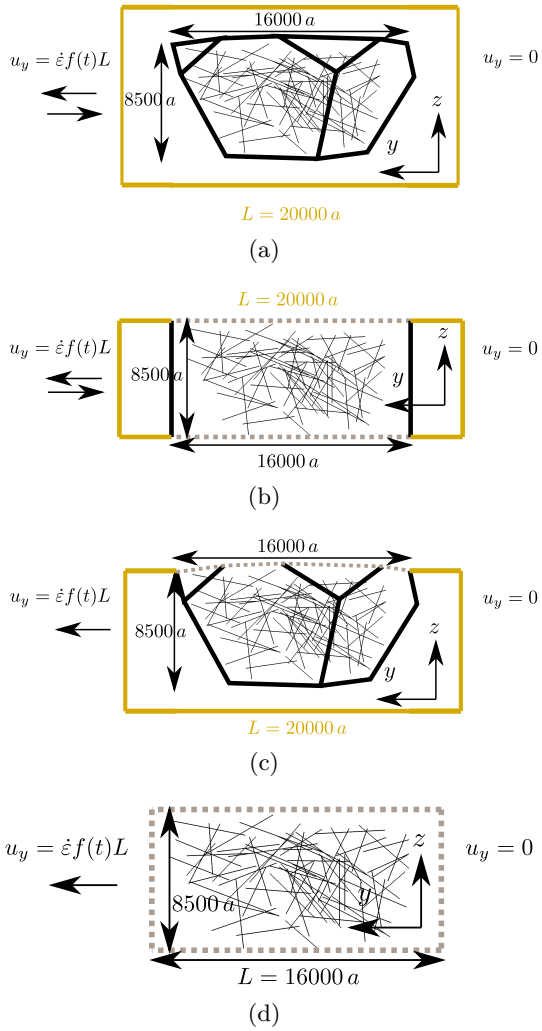

Figure 4.1: Cyclic boundary condition for a (a) fully embedded dodecahedron and (b) cuboid with two free surfaces in z-direction. Tensile boundary condition for (c) the dodecahedron from figure 3.1(c) and (d) a pillar. The yellow box represents the total elastic volume, dotted lines free surfaces and dark bold lines grain boundaries.

and $\boldsymbol{b_4} = a/2[110]$ (no surface component) embedded in a truncated surface dodecahedron (figure 3.1(c)) in a [010] tensile orientation are performed. The simulations consist of two sources of lengths $4745\,a$ containing both slip systems that belong to the respective Burgers vector. The boundary conditions and geometry are the same as in figure 3.1(c) with a controlled plastic strain amplitude of $\Delta\varepsilon_{\mathrm{pl}}/2 = 0.01\%$. When both systems are isolated, then Burgers vector $\boldsymbol{b_4}$ with no surface component shows at maximum load of the first cycle a higher length of collinear reactions (figure 4.3(a)). This is a similar observation to the surface cuboid using a total strain control simulation (figure 3.2(b)). For Burgers vector $\boldsymbol{b_4} = a/2[110]$, which points

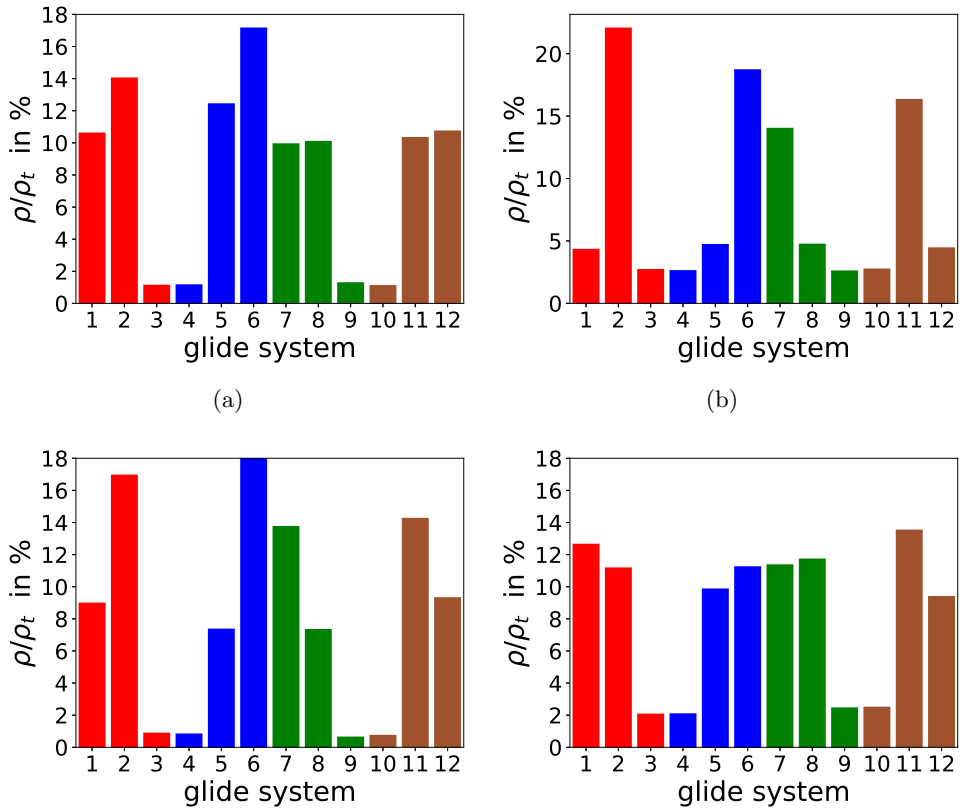

Figure 4.2: Distribution of the fraction of the final dislocation density ρ per glide system w.r.t. the total dislocation density ρ_t for [010] crystal orientation for setups from figures (a) 4.1(a), (b) 4.1(b), (c) 4.1(c) and (d) 4.1(d). Glide systems belonging to the same glide plane obtain the same color.

into the direction of grain boundaries, dislocations result in a localized plastic slip distribution (figure 3.5) such that during their forward and backward motion, they are confined by grain boundaries and are more probable to annihilate than in the case of $\boldsymbol{b_5} = a/2[01\bar{1}]$ which points to the free surface. Due to the higher annihilation reactions and length $\boldsymbol{b_4}$ Burgers vector requires longer time to reach the same dislocation density as $\boldsymbol{b_5}$. This is seen in the change of frequencies of the dislocation density evolution for the isolated systems (figure 4.3(b)). This means that during the loading stage of a plastic strain controlled simulation involving both Burgers vectors, glide systems with Burgers vectors with a large free surface component can reach the required plastic strain faster than glide systems with Burgers vectors with a small free surface component and hence, unloading occurs before any significant contribution of the latter.

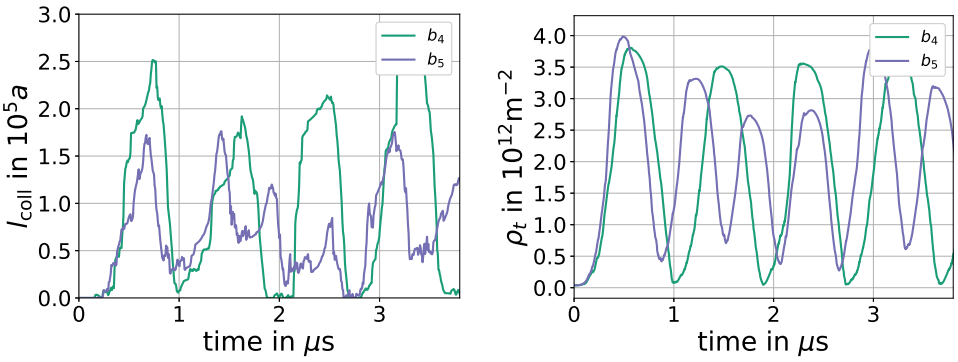

(a) (b)

Figure 4.3: Comparison of the evolution of the (a) length of collinear reactions and (b) dislocation density for two isolated simulations with one containing Burgers vector $\boldsymbol{b_4} = a/2[110]$ and the other $\boldsymbol{b_5} = a/2[01\bar{1}]$. Each simulation contains two sources which belong to slip systems 1 and 12 in the $\boldsymbol{b_4}$ case and slip systems 2 and 6 in the $\boldsymbol{b_5}$ case.

Using the above information, the dislocation density distribution of setup 1e (figure 3.9(a)) can be explained from its microstructural evolution (figure 4.4). In the figure, only dislocations of Burgers vectors $\boldsymbol{b_4}$ (parallel to the free surface) and $\boldsymbol{b_5}$ (with a large free surface component) are shown and colored accordingly. Two dislocations belonging to Burgers vector $\boldsymbol{b_4}$ are labeled as 1 and 2 and tracked during loading stages in the first and second cycle. The previously mentioned frequency variation in the dislocation density due to higher annihilation for Burgers vectors parallel to the free surface can be observed during the second cycle (figure 4.4(c)): Dislocations 1 and 2 are in the early stages of bowing out, whereas $\boldsymbol{b_5}$ dislocations have evolved further. In figure 4.4(d), dislocations 1 and 2 are seen to move backward, opposing the direction of the sufficiently high external stress, due to a backstress from $\boldsymbol{b_5}$ dislocations. This means that the backstress is an additional factor which contributes in diminishing the activity of glide systems with a Burgers vector parallel to the free surface.

It is apparent that the macroscopic Schmid factor is not solely responsible for slip activity in surface grains but both its combination with the crystal system orientation w.r.t. the free surface (normals vector $\boldsymbol{n}_{\text{surf}}$). The results show that dislocation density distribution in glide systems varies continuously for a rotation around the tensile axis (figure F.1): The dislocation density is maximum for systems with a high Schmid factor S and a large free surface component of the Burgers vector and intermediate (almost half) for systems with the same Schmid factor but a Burgers vector parallel to the free surface. The activity of the latter increases upon increasing the free surface component until all systems with the same Schmid factor $S = 0.41$

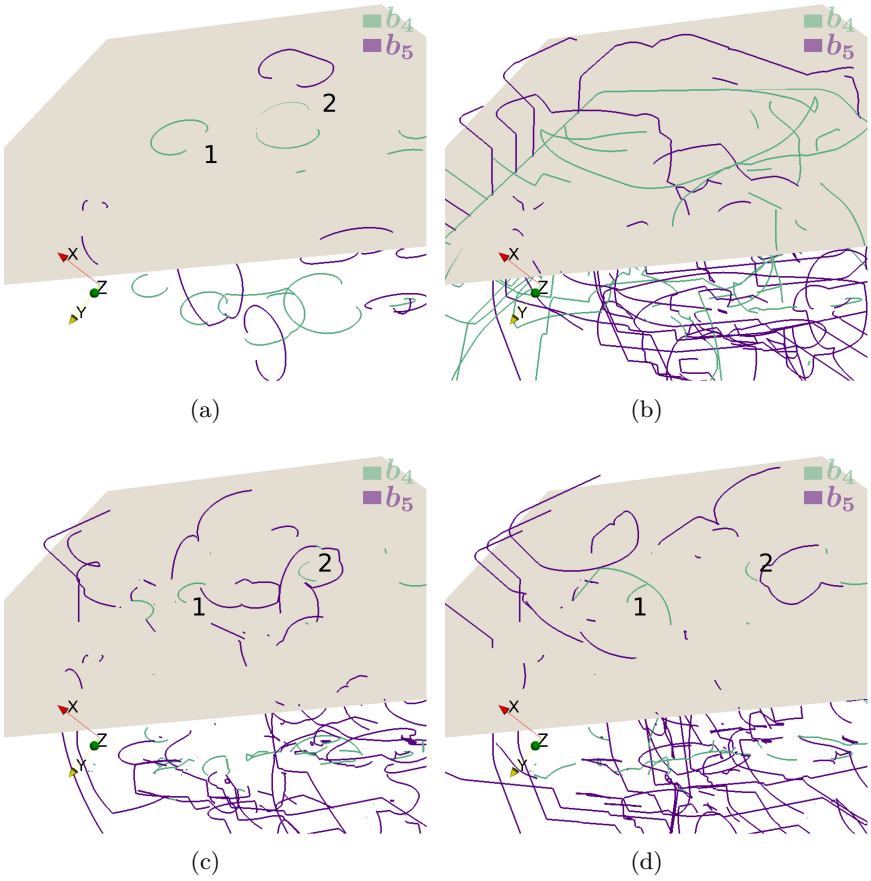

Figure 4.4: Visualization of the backstress experienced by dislocations belonging to Burgers vector $\boldsymbol{b_4}$. The full dislocation microstructure is filtered according to Burgers vectors $\boldsymbol{b_4}$ and $\boldsymbol{b_5}$ during (a) early stages of loading and (b) loading maximum of the first cycle. (c-d) Temporal evolution in the loading stage of the second cycle.

are symmetric w.r.t. free surface, thus have equal dislocation densities. Systems with a zero Schmid factor $S = 0$ have a negligible contribution to dislocation density independent of their orientation. Therefore, as an indicator for glide system activity, the absolute value of the free surface component of the Burgers vector $|\boldsymbol{e_b} \cdot \boldsymbol{n}_{\text{surf}}|$ alongside with the Schmid factor S need to be taken into account

$$S' = S\,|\boldsymbol{e_b} \cdot \boldsymbol{n}_{\text{surf}}| \tag{4.1}$$

where S' is the modified Schmid factor. Highly active systems of setup 1e (figure 3.9) have $S' = S = 0.41$, intermediate systems $S' = 0$ and $S = 0.41$ and almost inactive systems $S' = S = 0$. So only if S' of a considered slip system is high, then the slip system is highly active. Otherwise, if S' is small but S is high, medium dislocation densities are expected.

Conclusively, in an experiment or a simulation the tensile axis orientation alone is not sufficient to understand slip system activity and even surface deformation, but the entire crystal orientation w.r.t. free surfaces is necessary. For instance, authors such as Man et al. (2002, 2009) provide a detailed description of their crystallographic orientations, i.e. both the Burgers vector- and slip plane orientation w.r.t. the free surface. In their studies, many '*anomalous*' grains with high Schmid factors show no persistent slip markings. The authors attribute the aspect to the small angle between the Burgers vector and the free surface, and due to the size and orientation of neighboring grains which can reduce the effective Schmid factor. As a matter of fact Sauzay (2007), Sauzay und Man (2008) show using anisotropic elasticity that the classical Schmid factor measured in EBSD can be reduced by 24% due to surrounding grains. They also provide examples of several studies of surface grains having the same Schmid factor but show different dislocation microstructures and slip surface markings (Winter et al., 1981, Man et al., 2002, Blochwitz et al., 1996). The discrepancies can be explained in the present work by the modified Schmid factor S', which controls slip activity, and the rotation around the tensile axis. A detailed explanation of the dislocation microstructure dependency on the crystal orientation is investigated in the section below.

4.1.2. Heterogeneous pattern formation for large amplitudes

Analysis of the dislocation microstructure of the simulated setups reveals various patterns controlled by the crystallographic orientation. The results are discussed below.

[010]-tensile axis

For a single initial FR source, the tensile axis [010] yields, depending on the $\boldsymbol{b}$ orientation, different microstructures (figure 3.4). These were discussed in section 4.1.1. However, when all glide systems are involved, the result is a cellular structure (figure 3.11). The result agrees with the structures observed in the literature, i.e. not forming PSB-like structure but rather cells (figure 1.1). The cell structure is analyzed using the box-counting technique from Hähner et al. (1998a) to estimate its intrinsic properties. Although the domain area at hand is 13 times smaller than that in Hähner et al. (1998a), the largest cell-size of $900\,a$ is comparable. Nonetheless, it is an inequitable comparison, not only due to the domain and cell sizes, but also because of the monotonic large strain tension test in the experiment in contrast to a cyclic loading with rather small strain amplitude. In Plumtree und Pawlus

(1988) an empirical inverse relationship between the cell size and saturation stress is developed

$$\frac{\sigma_s - \sigma_b}{E} = A\frac{b}{\lambda_s} \tag{4.2}$$

where σ_s is the saturation stress, σ_b the backstress (≈ 3.1 MPa at room temperature), λ_s the linear intercept cell size and A an empirical material constant ≈ 7.8 for Al. For setup 1e, the cell size according to equation 4.2 is $\lambda_s \approx 3000\,a$ almost three times bigger than in the simulation (figure 3.11(b)). The latter aspect can be attributed to the small simulation volume relative to experiments, which confines the cell-size to the grain volume. As a matter of fact, Hussein und El-Awady (2016a,b) show using DDD simulations a proportionality between dislocation cell size and crystal size.

To understand the three-dimensional nature of the cell structure, the spatial analysis extends into filtering the edges of the dislocation structure along $\langle 110\rangle$, $\langle 112\rangle$ and $\langle 122\rangle$ directions (details in section 2.2.4). Figure 4.5(a) shows the fraction of the dislocation density in each of these directions. It is observed that after 4 cycles the fractions reach a steady state: almost 50% of the total dislocation density is aligned along $\langle 110\rangle$, $\approx 32\%$ along $\langle 112\rangle$ directions and $\approx 18\%$ along $\langle 122\rangle$ directions. For the largest graph component χ, $\langle 110\rangle$ oriented dislocations reveal (figure 4.5(b)) a bias for certain directions: After 8 cycles the structure shows almost no alignment along $\boldsymbol{b_5} = a/2[01\bar{1}]$ and $\boldsymbol{b_2} = a/2[011]$ directions and the largest component is aligned along the remaining $\langle 110\rangle$ directions which mainly belong to Burgers vector $\boldsymbol{b_2}$ and $\boldsymbol{b_5}$ (figure 3.9(a)). This contradicts DDD observations by Madec et al. (2002) for tensile tests on pillars along the [001]-direction, which report dislocation alignment along all $\langle 110\rangle$ directions.

To understand the bias in directional alignment mentioned above, $\langle 110\rangle$ oriented dislocations are examined according to junction percentage (figure 4.5(c)). The figure shows an increasing fraction of the total dislocation density belonging to junctions that reaches a maximum of 30% at the end of the simulation. This observation leads to the hypothesis that dislocation density is higher around Lomer junctions than random dislocations, due to the stability of Lomer junctions. Indeed, figure 4.6(a) shows the excess dislocation density around Lomer junctions compared to regular dislocation (according to equation 2.20). An excess in dislocation density of $\approx 27\%$ is found around Lomer junctions for $r = 200\,a$ with a drop in this measure for larger radii. However, to explain the previously observed dislocation alignment along specific directions, the final distribution of Lomer junction density per junction Burgers vector with respect to the total Lomer junction density (figure 4.6(b)) is examined. It is clear that Lomer junctions with parallel Burgers vectors $\boldsymbol{b_1}$ and $\boldsymbol{b_6}$

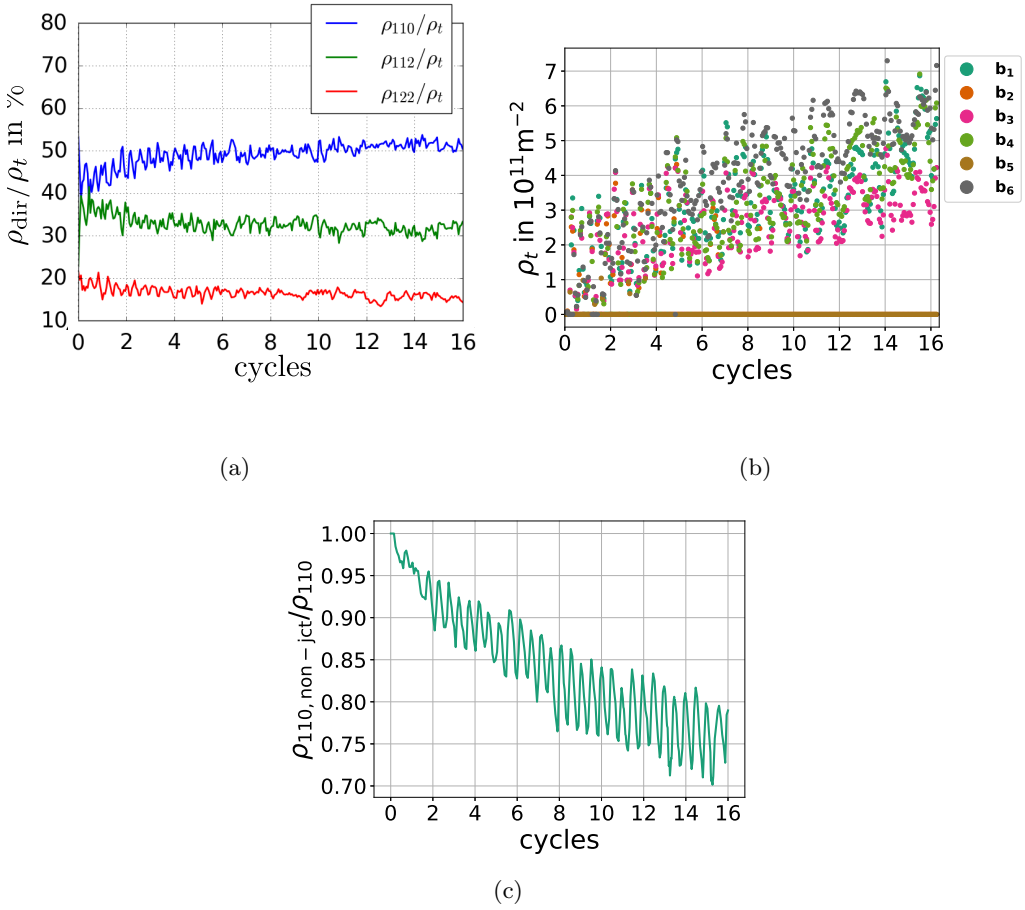

Figure 4.5: Directional analysis for $\Delta\varepsilon_{\mathrm{pl}}/2 = 0.01\%$. (a) Fraction of the dislocation density along binned directions. (b) Evolution of the dislocation density according to its alignment along $\langle 110 \rangle$ directions. (c) Fraction of non-junction dislocation density in $\langle 110 \rangle$ direction w.r.t. the total dislocation density in $\langle 110 \rangle$ direction. Adapted from El-Achkar und Weygand (2019).

(glide systems with Schmid factor $S = 0$) contain the highest Lomer density and correspond to dislocation alignment along opposite parallel directions $\boldsymbol{b_6}$ and $\boldsymbol{b_1}$ respectively. Smaller densities are contained in Lomer junctions of Burgers vectors $\boldsymbol{b_3}$ and $\boldsymbol{b_4}$, which have no surface component but a high Schmid factor. Finally ignorable dislocation densities are seen for Lomer junctions of Burgers vectors $\boldsymbol{b_2}$ and $\boldsymbol{b_5}$, which have a large surface component and a high Schmid factor. The reason for this distribution can be explained by the dislocation density distribution for regular dislocations (figure 3.9(a)) and the required combination of Burgers vectors to form specific Lomer junctions (figure J.2 of the appendix): $\boldsymbol{b_1}$ and $\boldsymbol{b_6}$ Lomer junctions contain the largest density because they result from the reaction of glide systems

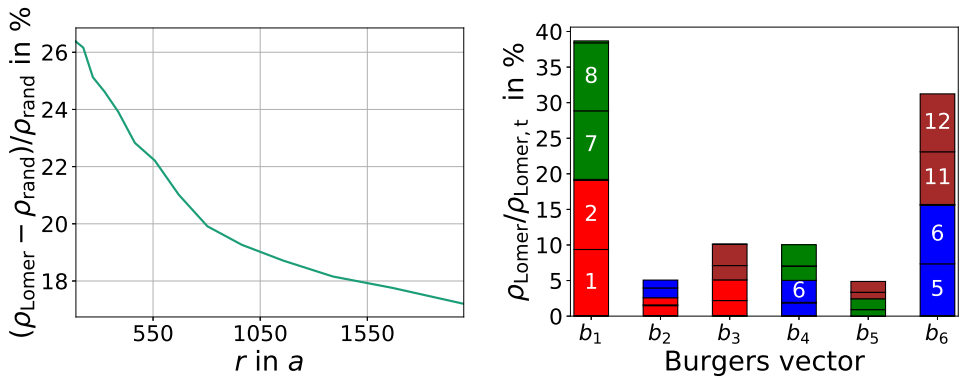

(a) (b)

Figure 4.6: Role of Lomer junctions for $\Delta\varepsilon_{pl}/2 = 0.01\%$. (a) Excess dislocation density around Lomer junctions (ρ_{Lomer} and ρ_{rand} are dislocation densities around Lomer junctions and random dislocations respectively). (b) Final Lomer junction density distribution ρ_{Lomer} per junction Burgers vector with respect to the total Lomer junction density $\rho_{Lomer,t}$. Glide systems belonging to the same glide plane obtain the same color. Adapted from El-Achkar und Weygand (2019).

with the largest dislocation density (high Schmid factor S and $\boldsymbol{b}$ with a large surface component) with glide systems with intermediate dislocation density (high Schmid factor S and $\boldsymbol{b}$ parallel to the surface). $\boldsymbol{b_3}$ and $\boldsymbol{b_4}$ Lomer junctions have smaller densities due to the reaction of glide systems with the largest dislocation density and glide systems with a Schmid factor $S = 0$. The remaining Lomer junctions $\boldsymbol{b_2}$ and $\boldsymbol{b_5}$ are a result of the reaction of glide systems with intermediate dislocation density and ones with $S = 0$. Therefore, the underlying dislocation alignment observed above (figure 4.5(b)) can be correlated with the distribution of Lomer junctions (figure 4.6(b)) and is another implication of the crystallographic orientation w.r.t. free surface. More specifically, a critical number of cycles is required for stable Lomer junctions to form along the predominantly mentioned directions as a result of the total crystallographic orientation. Eventually, regular dislocations moving in the vicinity of such junctions get trapped into the structure and align accordingly.

Lomer junctions are observed in several experimental studies which involve multi- or double slip loading conditions, where at least two glide systems that have the highest Schmid factors result in a Lomer reaction. Such reactions are reported to posses high stability according to Li et al. (2009). Both in Gong et al. (1997) and Jin und Winter (1984a) with respective [001] and [$\bar{1}$12]-tensile axis orientations, the authors attribute the formation of Lomer junctions as the cause to the observed early rapid hardening. Gong et al. (1997) report that due to errors in processing and testing, it is experimentally difficult to obtain an exact [001] orientation, therefore

a primary slip system would be initially established. Hence, the sensitivity of the microstructure to a 10° misalignment is studied.

[110]-tensile axis

The observed pattern in figure 3.26(a) (setup 2a) has a PSB-like nature. Four well-organized bundles of edge dislocations are seen and in between them are bowed-out screw dislocations in a region of less dislocation density. Intrinsic spacings between the bundles were described using a developed correlation function (equation 2.19) and show well-defined correlations. The structure is similarly formed by stable junctions as the [010] pattern, however, here only four glide systems are involved. The reaction-product of such glide systems yields a Lomer junction in $\boldsymbol{b_3}$ direction. The rotation of the crystal system around the tensile axis determines the spatial orientation, i.e. the alignment of the slip bands. Again the surface deformation is strongly influenced (figures H.3 and H.4 of the appendix) and changes from parallelogram patterns to well-defined block structure. The appearance of a PSB structure around [110] axis has been vastly shown in experiments (figure 1.1(b)).

[982]-tensile axis

The orientation [982] is a 10° rotation from [110]. It is the chosen orientation in Basinski et al. (1969) which examine early stages of fatigue in copper crystals. When all glide systems are considered in the simulation (figure 3.29), the structure is a mixture of Lomer junctions aligned along $\boldsymbol{b_4}$ direction (and dislocations trapped in the vicinity) and dislocation dipoles with $\boldsymbol{b_6}$ Burgers vector aligned along $[1\bar{2}1]$ (or $[0\,11\,\bar{9}]$ in laboratory frame) that belong to the slip system with highest S. The presence of very small prismatic loops that form in certain clusters is also seen. As a whole the pattern represents a combination of a multislip structure alongside with dipoles as in single slip. By increasing the loading amplitude, the multislip structure becomes even more transparent. In Basinski et al. (1969), the early few cycles (stage I) describe dense patches with some segments lying on $\langle 110 \rangle$ directions and some parallel to $[1\bar{2}1]$ with no predominant direction. The authors compare the microstructure to that developed during monotonic loading.

However, as discussed above, an exact crystallographic orientation is experimentally hard to achieve (Gong et al., 1997). In Jin und Winter (1984a), although the loading conditions are double slip ($[\bar{1}12]$ loading), the predominance of one slip system is reported. The cell structure shown by Lukáš et al. (1968) in a crystal oriented for

single single contains all six Burgers vectors, however, the majority of dislocations belong to only one Burgers vector. For this reason, glide system 9 (highest S) is kept, whereas the initial dislocation density of other systems is minimized. The microstructure shows an increase in dipoles, yet $\boldsymbol{b_4}$ alignment is still visible due to junction formation (figure 3.30(a)). When only glide system 9 is considered as the initial microstructure, then the result, i.e. veins consisting of edge dipoles, is comparable to the experimental results from Basinski et al. (1969) (figure 4.7). Although in the experiment, the microstructure appears cellular, the salient features which are seen also in cross-glide foils, i.e. densely packed dipolar bundles along $[1\bar{2}1]$, are captured in the simulation. The microstructure loses similarity to one deformed during monotonic loading.

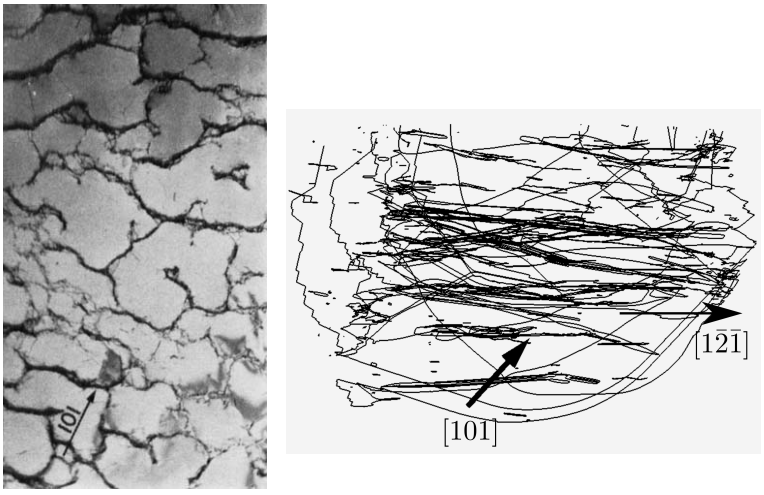

(a) (b)

Figure 4.7: (a) Early stages of the microstructure in the primary glide plane (cross-section width $\approx 14\,\mu$m) (courtesy of Basinski et al. (1969)). Reprinted with permission. (b) Simulation showing dipolar structure along $[1\bar{2}1]$ (Adapted from El-Achkar und Weygand (2019)).

The relaxation process (figure 3.30(c)) shows that the microstructure attains the formed pattern. In the single glide system scenario, if the FR sources are eliminated by connecting them and removing the pinning restriction (figure 3.30(d)), then only prismatic loops remain. However, this technique strictly depends on the prior history- and stage of loading. For example, if FR source elimination is directly followed by relaxation (as here), then most of the dislocations exit the free surface or annihilate. But if the FR source removal is followed by a small loading stage, then the proceeding relaxation process is smooth and the structure is preserved. A similar observation is reported in Winter (1975), Holzwarth und Essmann (1993) regarding tensile pre-

deformation preceding fatigue loading causing a more homogeneous distribution of PSBs.

4.1.3. Microstructure evolution dependency on strain amplitude

Since only early stages of fatigue can be simulated using DDD, the distinction between different fatigue regimes (low, high and very high cycle) is done at the level of applied plastic strain amplitude.

In figure 3.12, slopes of the dislocation density evolution curves, which are coarse indicators of underlying irreversibility, are examined for different applied plastic strain amplitudes in a [010] crystal orientation (setup 1e). The dislocation density increase per cycle for amplitudes between 0.002% and 0.01% follows a linear fit with the imposed amplitude, whereas for an amplitude below 0.002% there is no significant change in the density slope. Therefore, the plastic strain amplitude $\Delta\varepsilon_{\mathrm{pl}}/2 = 0.001\%$ is considered here as a transition to the VHCF amplitude-domain.

In the following, two extreme cases of applied plastic strain amplitudes are discussed: $\Delta\varepsilon_{\mathrm{pl}}/2 = 0.01\%$ and $\Delta\varepsilon_{\mathrm{pl}}/2 = 0.001\%$ which are denoted to as the large and small amplitude respectively.

Stress–strain behavior

The stress-plastic strain curve (figure 3.13) shows a hysteresis loop for both amplitudes indicating that irreversible dislocation motion occurs leading to energy storage in the resulting dislocation structure. Furthermore the plastic strain overshoots the prescribed values. There are two reasons for this behavior: the loading is applied in a saw-tooth fashion and the sign of the imposed strain rate is changed once the absolute value exceeds the imposed plastic strain amplitude. This sudden change and the high applied strain rate give rise to a number of dislocations which can glide further as the stress level is still sufficiently high.

Note that in VHCF experiments (Bathias, 1999, Straub et al., 2015), very high frequencies in the kHz regime are used to reach the required number of cycles. Therefore, this effect might be present in experiments too, but this is very difficult to assess as the time resolved deformation and loading conditions of single surface grains are not accessible experimentally. To quantify the magnitude of the overshoot in plastic strain, a corresponding number of dislocations sweeping a cross-section in the middle of the grain is calculated: 4 dislocations (10% additional dislocations)

for the larger amplitude and 1 dislocation (2.5% additional dislocations) for the smaller amplitude can produce the corresponding plastic overshoot. The observed overshoot in plastic strain will therefore not change the fundamental behavior. The effective stress amplitudes of about 55–75 MPa and total strain amplitudes in the range of 0.085%–0.12% reached in the simulations are both within the range of experimentally studied fatigue life curves for coarse grained and ultra-fine grained Al (Höppel, 2006).

Dislocation network characteristics from the graph analysis

Dislocation microstructures under fatigue conditions obtained by different plastic strain amplitudes show at the local scale common features, like the formation of dipoles, prismatic loops and the role of Lomer junctions serving as anchor points for dislocation accumulation. This is characterized by a number of statistical measures with similar evolutions but different absolute numbers, e.g. more or less pronounced two stage regime, with an incubation number of cycles followed by a linear increase of the statistical measures with number of cycles in the investigated range. On the overall scale, the developed dislocation microstructure (figure 3.14) is qualitatively different: for large amplitude, structure formation at early stages is observed, occupying a large fraction of the total grain volume. Up to 70% of the dislocation density belongs to the largest component while the remainder is found in prismatic dislocation loops and dislocation debris (figure 3.16(a)). At this stage, even eliminating artificial FR sources (not shown here) by connecting their end-points and removing the pinning restriction shows almost no difference during further cycling of the dislocation network compared to keeping sources. This indicates extreme stability of the evolved dislocation network and its independence on initial dislocation sources. Applying this elimination procedure at very early stages results in a large number of prismatic loops which remain stable during further cycling and almost no increase in dislocation density occurs. On the other hand, in the small amplitude simulation, the low dislocation density is contained in the increasing number of prismatic loops and debris clusters. The largest component containing a large number of Lomer junctions shows early stage clustering.

The evolution of the number of graph components χ of the dislocation network (figure 3.15) shows a nonlinear relationship upon decreasing the prescribed amplitude. Indeed, after 10 times more cycles, the number of components for the small amplitude is approx. 2.8 times less than for the large amplitude. This phenomenon is observed also in additional microstructural measures such as the dislocation density (figure 3.17) and total number of prismatic loops (figure 3.18). Both simulation

types show that after a critical number of cycles (6- and 70 cycles for the large- and small amplitude respectively), there is a slope change in the analyzed measures. The change is very clear in the large amplitude simulation and less pronounced for the small amplitude. As can be seen from the previous data, the drastic slope change can be linked to the stability of the structure. For instance, as soon as the dislocation density of the largest component stops fluctuating heavily and the dislocation network reaches a critical spacing, then the density of edge dislocations and the number of stable prismatic loops increase at a different rate.

Dislocation dipoles characteristics

Splitting the dislocation density into different characters (figure 3.17) reveals also a turning point for the evolution of the edge dislocation density. For $\Delta\varepsilon_{\mathrm{pl}}/2 = 0.01\%$, after 6 cycles the proliferation in edge density is reflected in a microstructure of mean spacing $1/\sqrt{\rho_t} \approx 1500\,a$. A detailed analysis of these edge dislocations reveals that the edge density mainly constitutes dislocation dipoles and Lomer junctions. For $\Delta\varepsilon_{\mathrm{pl}}/2 = 0.001\%$, the growth in edge density after 70 cycles is rather slow and related to clustering around the largest component. The analysis of prismatic loops and dislocation debris (figure 3.18) shows that prismatic loops of second order and dislocation debris are extremely stable and present sites of dislocation clustering. And although the dislocation density slope vanishes for this amplitude (previously mentioned), the number of defects at the microscopic level shows no saturation.

The very large number of prismatic loops for $\Delta\varepsilon_{\mathrm{pl}}/2 = 0.01\%$ is reflected in the smoothness in average values and distribution of the prismatic shape factor p_{shape} (figure 3.19) compared to large oscillations at early stages for the small amplitude due to the small number of prismatic loops. For the large amplitude, the averaged shape factor $< p_{\mathrm{shape}} >$ increases with number of cycles, while for the small amplitude it converges to $< p_{\mathrm{shape}} > \approx 0.7$. From the distributions of $< p_{\mathrm{shape}} >$ (figures 3.19(b) and 3.19(c)), the stability of the mean value for $\Delta\varepsilon_{\mathrm{pl}}/2 = 0.001\%$ can be seen since the distributions are very similar with the exception of maximum shift from 0.7 to 0.9 corresponding to prismatic loops of aspect ratios 6 and 2.5 respectively and increase of equiaxed loops at the expense of elongated loops. These results in the early stages are in agreement with experimental findings reported by Feltner (1966) (aspect ratio of 5). In the case of the large amplitude, there is a drastic shift from a Poisson-type distribution to a cumulative-type distribution and a similar shift in maxima from 0.7 to 0.9. The latter is accompanied by a huge increase in frequency for equiaxed prismatic loops (from about 0.001 to about 0.16), leading also to an increase of the mean value. Furthermore it is found that a large number of loops formed at later

stages are extremely small having side lengths in the range of $50\,a$–$100\,a$ for both amplitudes.

The analysis of dislocation dipoles shows that the average dipole height $< h >$ increases with further cycling for the large amplitude and remains rather constant for the small amplitude (figure 3.21). The distribution of dipolar heights h is exponential, indicating also that the smallest possible distance—limited by minimal distance between parallel glide planes—is the most likely and stable one. The distribution is in contrast to the normal distribution seen in Déprés et al. (2008) but very similar to the distribution of dipolar heights in PSBs in Ni single crystals presented by Hähner et al. (1998b). In the latter work, at the lower end of the distribution and prior to the most probable height, the histogram decreases smoothly to zero due to dislocation annihilation mechanisms, not included in the DDD framework. The authors suggest that dislocation annihilation is not occurring at a critical interplanar distance and fully spontaneous but involves thermal activation leading to dislocation climb. In the present study dislocation climb is not considered and therefore the latter mechanism cannot occur. The maximum height in the experimental distribution at the highest investigated temperature (750 K) agrees with the observations of the simulations. In Antonopoulos et al. (1976), analysis of dislocation heights and lengths for Cu reveals the most common- dipolar height of 4 nm ($\approx 11.1\,a$) and length of 30 nm ($\approx 84\,a$). It is a similar distribution as in Hähner et al. (1998b). The stability and strength of the dipoles can be understood because of $h_{\max} = 11.8\,a$ is almost 3 times less than the critical height $h_{\text{crit}} = 35\,a$, for which a dipole would break apart under a total resolved shear stress of $\tau_{\text{crit}} \approx 33$ MPa. For higher number of cycles the maximal strength decreases and therefore favors larger heights. The average dipolar length $< l >$ shows similar convergence in the small amplitude case but decreases for the large amplitude to reach $250\,a$ (figure 3.22). Since elongated prismatic loops are a subset of dislocation dipoles, the distribution of dipolar lengths l shows strong similarities with the maximum loop dimension. In the models presented by Fourie und Murphy (1962), Gilman (1964) short dipoles are a consequence of high cross-slip activity, large strains or double slip orientations. The influence of cross-slip was also demonstrated in Wilsdorf und Schmitz (1962), Grosskreutz und Waldow (1963), where dipoles in aluminum were shown to be generally shorter than those formed in Cu due to the ease of cross-slip in aluminum.

Macroscopic damage analysis

The consequence of irreversible dislocation motion can be resolved at the macro-scale by characterizing surface deformation or averaged bulk plastic strain (section 2.2.5).

Examining the evolution of the maximum value of the norm of the gradient of the surface displacement field (figure 3.23) shows that this measure is very sensitive to the applied amplitude in comparison to the evolution of the mean, RMS or minima/maxima. For the large amplitude a linear increase per cycle is observed for this value as apposed to the small amplitude, where it is rather constant. This is supported by the evolution of the corresponding histograms: In the early stages the surface for the large amplitude is rather flat with a small standard deviation. However, in the later stages of the simulation, the distribution is wider (standard deviation increases) and the maximum is shifted away from zero. Although the number of vacancy- and interstitial prismatic loops are equal (figure D.2), they result in embryonic extrusions and intrusions at the surface. The observation of equal vacancy and interstitial loops has been reported by Feltner (1966). In contrast, the small amplitude shows a very narrow distribution of small surface displacements with a slight shift from zero to larger values.

The irreversibility p factor is an alternative way to describe the amount of irreversibility of a system. Since surface measurements are easy to access in experiments, they are used to determine p (Mughrabi, 2009, 1999, Weidner et al., 2010). In the current study, both bulk- and surface p increase with the applied plastic strain amplitude, which is in agreement with Mughrabi (2006) $p \propto 2\gamma_{\mathrm{pl}} y_s / b$ (y_s is the annihilation distance of screw dislocations due to cross-slip), where cyclic irreversibility is attributed to the irreversible motion of screw dislocations in PSB-channels. The $1/N_{\mathrm{cycle}}$ behavior of p is witnessed as it is directly included in formulas 2.23 and 2.24. A shift between surface- and bulk p estimations is observed, which is smallest for the largest amplitude (figure 3.24). The reason is that at smaller amplitudes, the dislocation density is also smaller, meaning that less dislocations exit the surface despite generating internal irreversible structures. Another aspect is that when the surface experiences a small localized deformation while a huge part remains undeformed, RMS poorly captures these displacements. Also the displacement fields of the formed structures are short-ranged meaning that the presence of irreversible bulk structures that do not exit the surface can be barely detected from surface measurements.

Internal irreversibility can be seen in the evolution of the irreversible plastic strain $\varepsilon_{\mathrm{pl,irre}}$[1], which shows no saturation for both amplitudes (figure H.1). This means, that if given sufficient time, the small amplitude may cause, due to the accumulation of irreversible plastic strain, a considerable surface roughness and consequently damage at the free surface. This agrees with the considerations made by Mughrabi

[1] The measure $\varepsilon_{\mathrm{pl,irre}}$ characterizes the entire defect microstructure including prismatic loops, dipoles and structures that are not separately classified but produce irreversible plastic strain

(1999) stating that the accumulation of even small irreversible random slip, with absence of PSBs, can lead to sufficiently strong surface roughening followed by a surface crack.

In comparison to experimental p values, which are available for Cu and α iron, the current estimations for Al show considerably higher values in the considered amplitude regime. Nevertheless, p required to form PSBs ($p \approx 0.2 - 0.4$ (Mughrabi, 2009)) is around 10 times higher than for the large amplitude. If the cross-slip difficulty is increased to mimic Cu, then the irreversibility decreases and p values come closer to the values observed for Cu (figure 3.24(c)). This means that the ease of cross-slip in Al is proportional to the increase in irreversibility and the high p values.

4.2 Fatigue in *bcc* metals

Fatigue in *bcc* metals containing an inclusion is controlled by a larger parameter space than in *fcc* metals. For instance, cross-slip, which is a mechanism that controls dislocation structure formation can occur on three glide planes for each Burgers vector. The influence of the phenomenological friction stress τ' is an additional numerical value which needs to be taken into account. Most importantly, the way the inclusion is modeled, three different properties can be assigned to it:

- It acts as a geometrical obstacle.
- The difference in elastic constants yields a modulus-induced stress field $\boldsymbol{\sigma}^{\mathrm{el}}$.
- It has a misfit stress field due to a misfit strain e_C^*.

The resulting microstructures in section 3.2 are analyzed below regarding the influence of these properties.

4.2.1. Influence of inclusion intrinsic properties

$[19\bar{1}]$-tensile axis orientation

The developed microstructure for a $[19\bar{1}]$-tensile axis orientation shows several features which are highlighted by different zones in figure 3.33. To explain the effect of individual inclusion properties on the evolved microstructure, the results of the

simulations of single FR sources with single inclusion properties (figures 3.36, 3.37 and 3.38) are discussed here.

In figure 3.36 the high reversibility for the obstacle and inclusion with different elastic properties than the matrix is due to the relatively small strain amplitude since only few dislocations pile-up and travel a small distance in cross-slip planes before load reversal without being able to generate a stable network. For the setup with a modulus-induced stress field $\boldsymbol{\sigma}^{\mathrm{el}}$ the dislocation density is higher (figure 3.36(a)). The increase in plasticity has two reasons: Dislocations experience higher stresses due to the stress concentration around the inclusion (figure C.1) so they get activated earlier and can move further before reversing the load. The second reason is displayed in figure 4.8: The illustration shows a cross-section for the used Burgers vector $\boldsymbol{b_1}$, taken from the center, which reveals the color of the glide plane for which the resolved shear stress is highest, i.e. a cross-slip map for screw dislocations. The map shows that the highest resolved shear stress is mainly in plane $\boldsymbol{n_1}$ except for a small area around the inclusion where the resolves shear stress is higher for plane $\boldsymbol{n_3}$. The map remains constant even at minimal load such that the first bow-out already results in cross-slip at the two zones. Hence, dislocations can freely leave the primary plane and even cross-slip multiple times to form prismatic loops. In the obstacle setup, the map is entirely colored in blue because the Schmid factor for glide system 1 is highest[2]. So not only does $\boldsymbol{\sigma}^{\mathbf{el}}$ contribute to a localized stress concentration which enhances early plastic activity, but also controls cross-slip areas and eventually the dislocation microstructure.

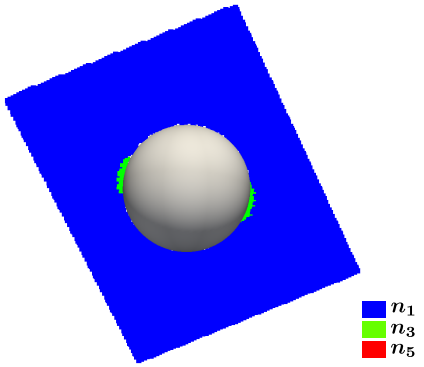

Figure 4.8: Cross-slip map in a central section perpendicular to $\boldsymbol{b_1}$ showing the plane with the highest resolved shear stress. Colors correspond to different glide planes (numbering is given in table J.1).

[2] the other equally high system belongs to a different Burgers vector which is not simulated

The other investigated inclusion property is the misfit stress field. In figure 3.37 the general evolved structure for higher misfit values are hexagonal prismatic loops which form around the inclusion and remain stable even when unloading. A simple explanation is that the misfit stress is time-invariant/constant throughout the entire simulation. Therefore, the loading saw-tooth signal, which results in an almost homogeneous stress field (same material properties), is overlapped on top of the misfit stress and depending on e_C^* the developed structure may experience significant stresses even when unloading and, hence, remain stable.

For a deeper understanding of the misfit parameter, a local stress analysis is conducted in planes perpendicular to $\boldsymbol{b_1}$. A cross-slip map in a central plane of an unloaded inclusion with $e_C^* = 0.2\%$ reveals the six-fold symmetry of the misfit stress field (figure 4.9): The stress field is radial symmetric and depending on the position, cross-slip can occur in one of the three involved glide planes. The map characteristics extend throughout the whole volume and the sign of the stress field shows that three connected positive sectors are followed by three connected negative sectors. From figure 4.9 it can be justified how cross-slip of the initial dislocation results in a

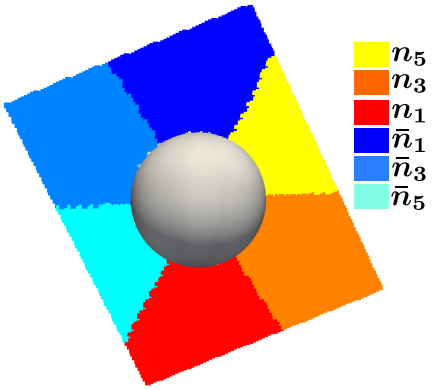

Figure 4.9: Cross-slip map of a misfitting inclusion ($e_C^* = 0.2\%$): cutting plane perpendicular to $\boldsymbol{b_1}$ showing the slip plane number with maximum resolved shear stress multiplied by the sign of the resolved shear stress.

closed loop (figure 3.38). If the sign of the misfit strain e_C^* is positive (as here), then interstitial loops form around the inclusion and are trapped by a stress gradient in the primary plane (figure 4.10), whereas vacancy loops are repelled away from the inclusion. Vice versa, if the misfit is negative, then vacancy prismatic loops develop around the inclusion.

The superposition of the misfit stress field on top of a homogeneous cyclic stress field (as in figure 3.37) is studied for two misfit strains $e_C^* = 0.1\%$ and $e_C^* = 0.3\%$ in figure 4.11. For $e_C^* = 0.1\%$ a central $\boldsymbol{b_1}$ cutting plane (figure 4.11(a)) and a $2500\,a$ cross-section away from the center (figure 4.11(b)) are analyzed for half the loading

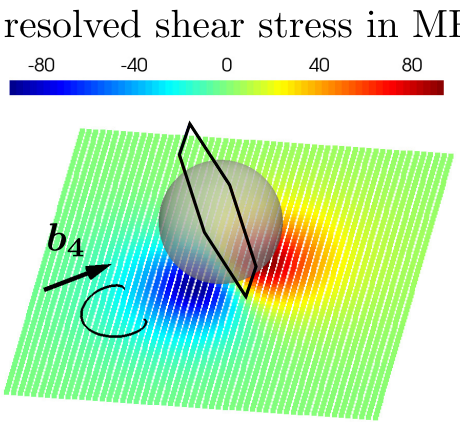

Figure 4.10: Entrapment of interstitial loops in stress gradients.

amplitude during tension. In the case of the first cutting plane, the external stress causes cross-slip to only occur on the $\boldsymbol{n_1}$ plane (highest Schmid factor), whereas for the second cutting plane an $\boldsymbol{n_3}$ region is observed on the left. For a larger misfit $e_C^* = 0.3\%$, the central cutting plane has a small $\boldsymbol{n_3}$ region (figure 4.11(c)), whereas in the second cross-section all three planes are observed with a larger $\boldsymbol{n_3}$ region than for $e_C^* = 0.1\%$ (figure 4.11(d)). In the $-\boldsymbol{b_1}$ direction (not shown here), the cross-sections show the same features but are mirrored. The observation of additional cross-slip planes for higher misfit values can be explained using Schmid factors of the underlying tensile axis orientation (figure 4.12). For each point the Schmid factor is maximum in the initial glide system 1 ($\boldsymbol{n_1}$) followed by glide systems 5 ($\boldsymbol{n_3}$) and 9 ($\boldsymbol{n_5}$). So for a small misfit $e_C^* = 0.1\%$ the misfit stress in the $\boldsymbol{n_5}$ plane is relatively small compared to the loading stress which is highest in $\boldsymbol{n_1}$ planes (figures 4.11(a) and 4.11(b)). Since the Schmid factor for $\boldsymbol{n_3}$ planes is relatively high, the superposition of the misfit stress with the external stress causes the plane to be observed for a small misfit stress. For a misfit strain of $e_C^* = 0.3\%$, the misfit stress in plane $\boldsymbol{n_5}$ exceeds the loading stress in several locations (figure 4.11(d)), hence, the observation of characteristic $\boldsymbol{n_5}$ dislocations with a high density for $e_C^* = 0.2\%$ and $e_C^* = 0.3\%$ in figure 3.37.

The observed microstructure from figure 3.33 can be explained by the above observations:

- The formation of Orowan loops is attributed to the spherical obstacle nature of the inclusion which obstructs dislocation motion and causes them to wrap around the inclusion.
- Hexagonal prismatic loops are due to the superposition of the misfit stress field and the applied stress (figure 3.38).

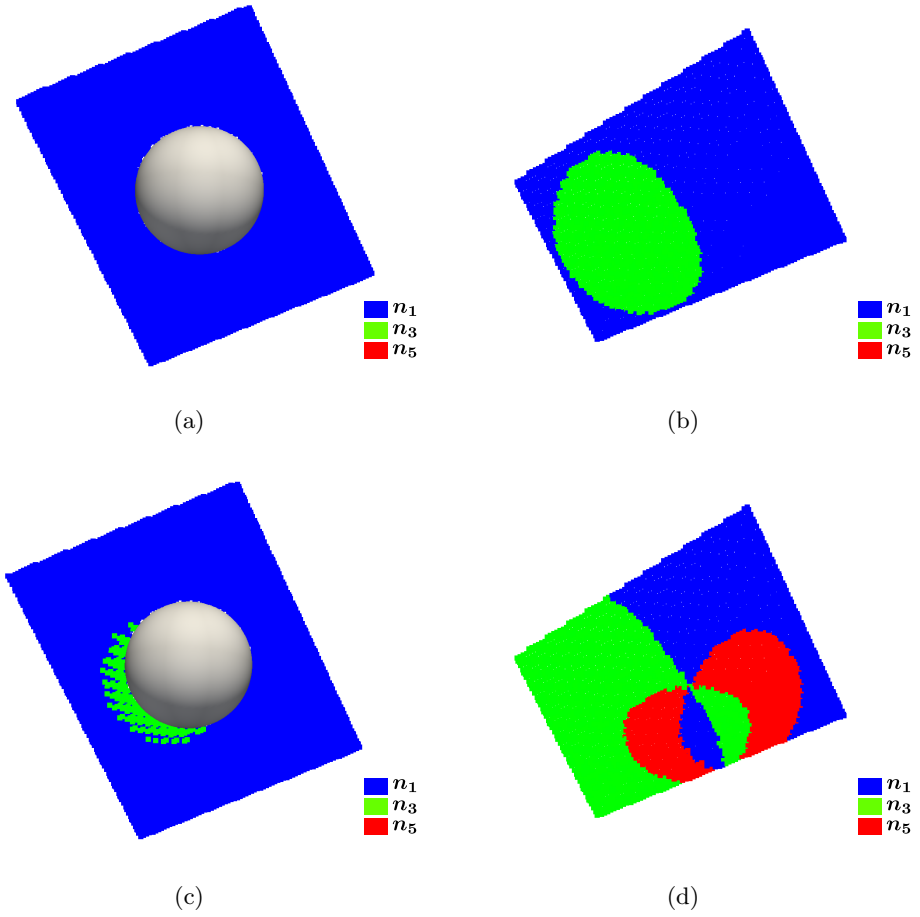

Figure 4.11: Cross-slip map (as in figure 4.9) for different misfit strains for half the loading amplitude during tension: (a-b) $e_C^* = 0.1\%$ (c-d) $e_C^* = 0.3\%$ for a for a central cross-section in (a) and (c) and 2500 a away from the center in (b) and (d).

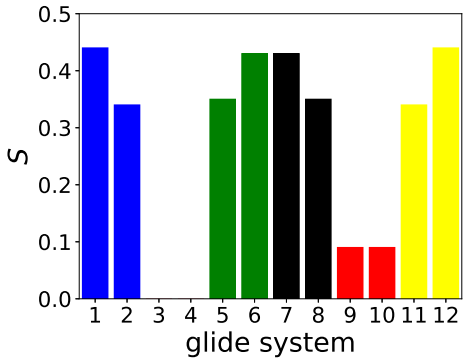

Figure 4.12: Schmid factor distribution for tensile axis $[19\bar{1}]$. Coloring is according to glide planes.

- Prismatic clusters, which accommodate the majority of the plastic strain (figure 3.34(a)), develop in regions controlled by the modulus-induced stress field (figure 4.8) and retain their stability due to the misfit stress field (figure 3.37(a)).

This means that the modulus-induced stress is largely responsible for structure formation, however the misfit stress, as seen in the dislocation density and stability of hexagonal loops, plays a key role in structure irreversibility.

In the case of elongated dipolar loops which form at the inclusion due to a regular forward and backward motion, the interaction with the inclusion misfit field is more complicated than for hexagonal loops and highly depends on the position. In figure 4.13 the interaction of an interstitial dipole is illustrated according to Humphreys und Hirsch (1970). The three-dimensional geometry of the problem is

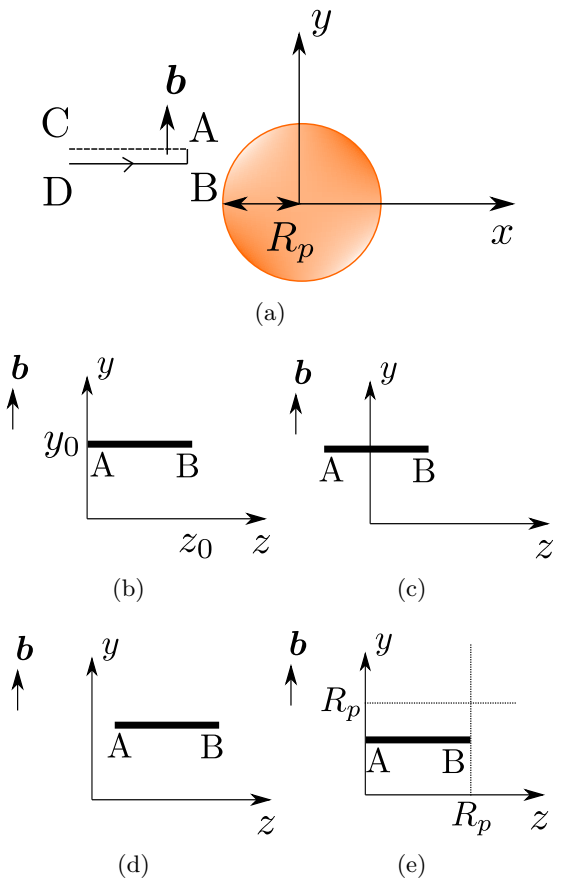

Figure 4.13: Interaction of an elongated dipole with a misfitting inclusion according to Humphreys und Hirsch (1970).

shown in figure 4.13(a): The Burgers vector of the loop is along the y-direction and the jog AB is in the plane $x = R_p$ and extends from $z = 0$ to $z = z_0$ at a height $y = y_0 = z_0$. For this scenario (figure 4.13(b)) the dipolar arm AC is repelled while the force on BD is zero. If the arm AC is located at $z < 0$ and BD at $z > 0$ (figure 4.13(c)), then both arms will be repelled, however, if the jog AB is very close to the inclusion then attraction force is stronger than repulsion. If AC and BD are on the same side, then one of them is attracted and the other is repelled (figure 4.13(d)). If

in the latter case, BD is attracted to the inclusion, it can lead to the total attraction of the interstitial. Last but not least, if AB extends from $z = 0$ to $z = R_p$, then if $y \leq R_p$, the dipole will be attracted, otherwise repelled (figure 4.13(e)).

The variation of the radius of the inclusion (figure 3.39) shows an increasing irreversibility in the dislocation density upon increasing the radius only when the inclusion has a misfit. Otherwise, the radius barely plays a role. The misfit stress according to equation 2.10 is proportional both to e_C^* and R_p, so by increasing these values, the stress around the inclusion becomes higher and additional planes will be included for cross-slip. The following finding is a compliment to the prominent Murakami model (see equation 1.3), where the only inclusion property included is the area of the inclusion ($\propto R_p$).

[010]-tensile axis orientation

The complex microstructure observed for the [010]-loading axis is similarly analyzed according to overlapping stresses. Since the loading orientation is symmetric w.r.t. all Burgers vectors, $\boldsymbol{b_1}$ is used as an example.

For a perfectly fitting inclusion with different material properties than the matrix, cross-slip maps for Burgers vector $\boldsymbol{b_1}$ are considered: A three-dimensional plot (figure 4.14(a)) and cross-sections normal to $\boldsymbol{b_1}$ (figures 4.14(c) and 4.14(e)) are shown, for which the coloring corresponds to the slip plane with maximum resolved shear stress. Although the Schmid factors are the same for glide systems 1 ($\boldsymbol{n_1}$) and 5 ($\boldsymbol{n_3}$), the field $\boldsymbol{\sigma^{el}}$ splits the domain into regions where either $\boldsymbol{n_1}$ or $\boldsymbol{n_3}$ are higher. No region with the plane $\boldsymbol{n_5}$ is observed. Despite the fact that $\boldsymbol{b_1}$ cross-sections show potential sectors, for which rectangular prismatic loops can form, the sign of these domains is the same and does not allow to close the loop (unlike figure 4.9). When the misfit stress ($e_C^* = 0.2\%$) is added on top of $\boldsymbol{\sigma^{el}}$, then the connected areas of both planes become larger on the surface of the cube (figure 4.14(b)). Also the introduction of plane $\boldsymbol{n_5}$ is observed, which depends, as explained before, on the magnitude of e_C^*.

The plateau seen in the dislocation density evolution during unloading (figure 3.40) is firstly seen during this work. It can be explained by the complex interplay between dislocations from all glide systems, the misfit stresses and the large cross-slip sectors which are seen in the maps above. The cross-slip sectors extend throughout the whole volume unlike the concentrated region in the $[19\bar{1}]$-tensile axis orientation, which is due to the fact that the Schmid factors are equal in this orientation. As a matter of fact all Burgers vectors are active such that each dislocation can follow a complex cross-slip path as in figure 4.14 if the activation stress is sufficiently high.

Additionally, the misfit stresses introduce a third plane, for which the Schmid factor is zero, leading to an even more complex interaction. Thus, the complex stable regions of dislocations that form in figure 3.41 which cause the dislocation density to remain constant while unloading can be rationalized by the nature of the stress field in the multislip loading scenario. This means that multislip orientations with the presence of an inclusion cause higher irreversibility and are more dangerous than single slip orientations.

4.2.2. Polycrystal behavior

The investigated polycrystal in section 3.2.2 shows an irreversibility in the dislocation microstructure in the vicinity of the inclusion (figure 3.44(a)). The growth of the irreversibility around the inclusion is observed in the plastic strain distribution around the inclusion. Similar plastic strain maps are shown in Chai (2006), Chai et al. (2012) which show high localized plastic activity near the inclusion.

An asymmetry during tension and compression is observed, which has its origin in the overlapping stresses of the misfit stress field and modulus-induced stress field. Depending on the grain orientation, tension loading stresses can cause for example a positive resolved shear stress in the same point, where misfit stresses result in a negative resolved shear stress causing stresses to cancel out but to add up during compression.

An analogous idea as before is used to analyze the inclusion properties (figure 4.15). Again the misfit strain is found here to play the most important role in the irreversibility of the dislocation density.

The behavior upon grain coarsening is shown in terms of the evolution of the dislocation density (figure 4.16). It can be seen that grains with larger diameter result in a much larger dislocation density than smaller grains for the same loading conditions. Several reasons can be attributed to this behavior: First, in smaller grains the probability of a grain containing two- or more cross-slip sectors (presented above for single crystals) is small. This means that due to the modulus-induced stress field most dislocations can only cross-slip to one plane until reaching the grain boundary. On the contrary, dislocations in large grains can pass through different cross-slip sectors and result in more complex interactions which lead to dislocation density increase and irreversibility. Another aspect is related to the short-ranged stresses around the inclusion due to the misfit $\propto \boldsymbol{r}^{-3}$ and difference in elastic constants $\propto \boldsymbol{r}^{-2}$ (Kirsch, 1898). As a consequence dislocations in small grains in the vicinity of the inclusion experience higher stresses than the rest of the

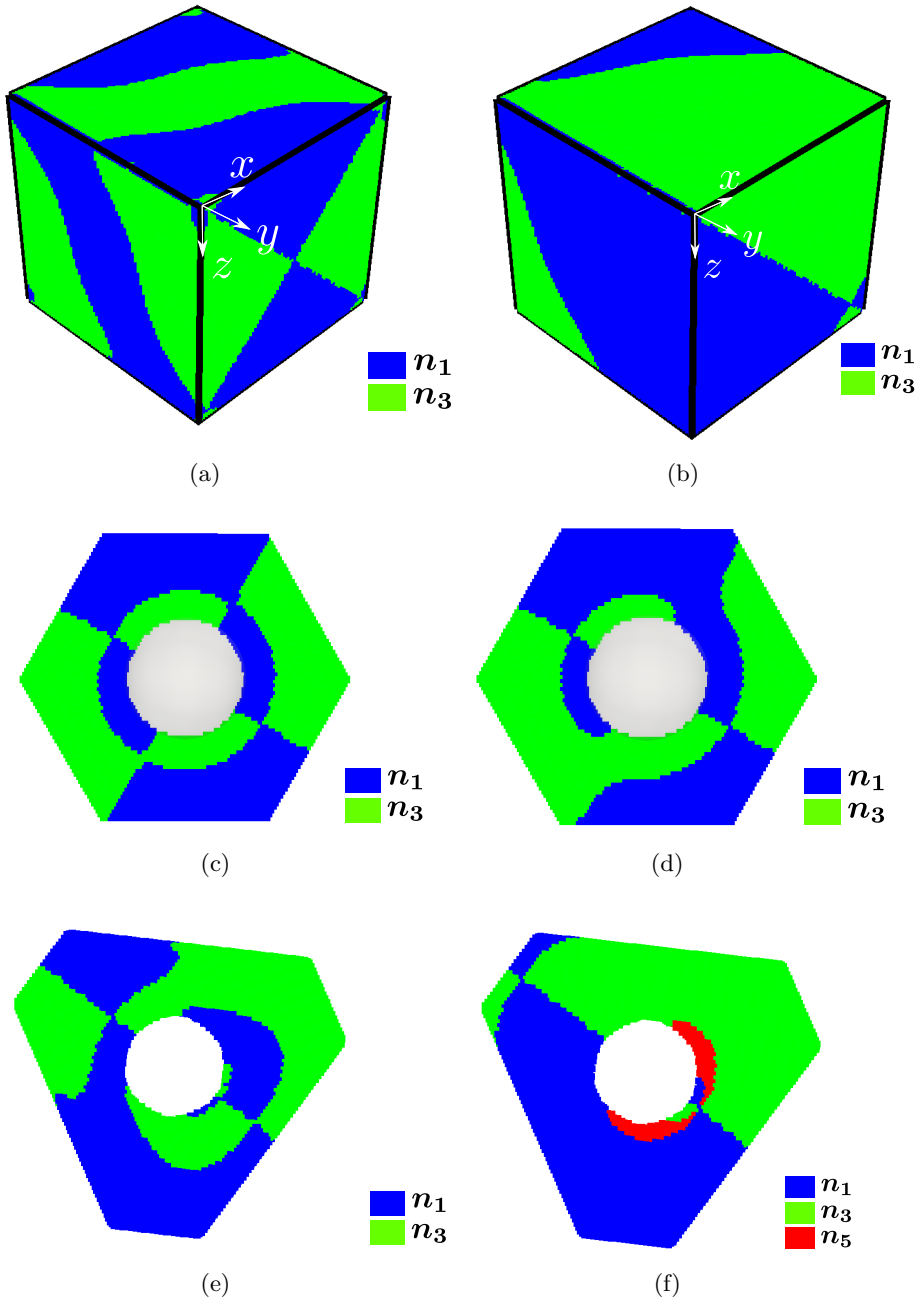

Figure 4.14: Visualization of the slip plane number with maximum resolved shear stress for Burgers vector $\boldsymbol{b_1}$: (a-b) Three dimensional visualization of the surfaces of the simulation domain for $e_C^* = 0$ and $e_C^* = 0.2\%$ respectively. (c-d) central cross-section perpendicular to $\boldsymbol{b_1}$ for $e_C^* = 0$ and $e_C^* = 0.2\%$ respectively. (e-f) cross-sections perpendicular to $\boldsymbol{b_1}$ $500\,a$ away from the center for $e_C^* = 0$ and $e_C^* = 0.2\%$ respectively.

polycrystal and get stuck at grain boundaries without any major interaction with

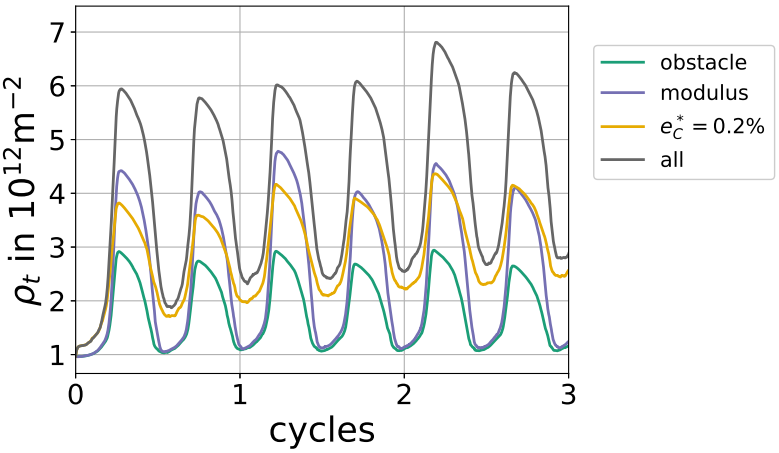

Figure 4.15: Dislocation density evolution for an inclusion with different properties. Obstacle: a perfectly fitting spherical obstacle. Modulus: a perfectly fitting inclusion with different material properties than the matrix. $e_C^* = 0.2\%$: inclusion with a misfit strain e_C^*. all: All the properties combined.

far away grains. On the other hand, dislocations in larger grains can move far away from the inclusion and react with other dislocations further away.

This means that the irreversible zone in polycrystals can be always found around the inclusion and can extend in larger grains throughout the whole volume. In other words, a grain refinement produces a smaller irreversibility which is localized around the inclusion. The formation of cell structures, described in the literature (Chai et al., 2012, Grad et al., 2012), is not possible due to computational restriction in system size and cycle number. However the observed increasing irreversibility is an early stage of a stable structure formation which may lead to a cell structure.

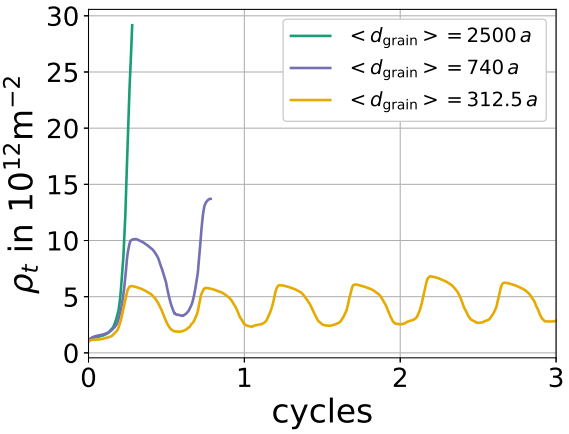

(a)

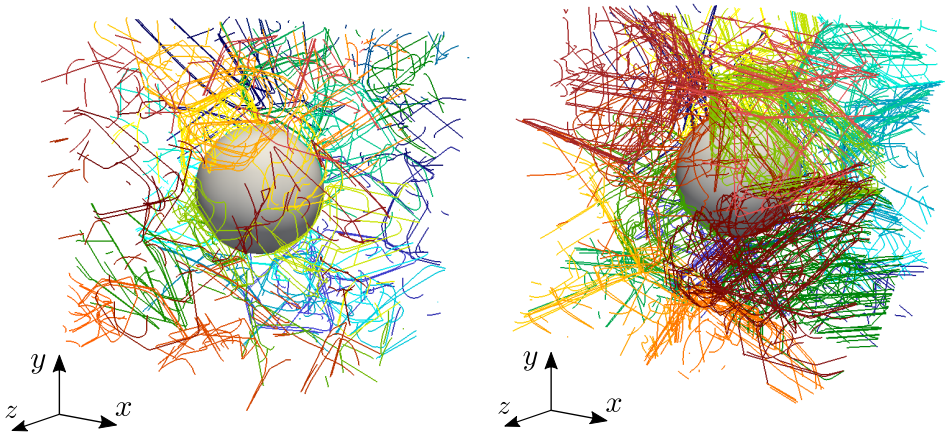

(b) (c)

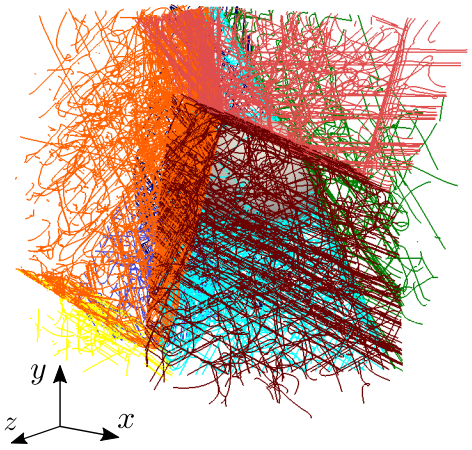

(d)

Figure 4.16: (a) Dislocation density evolution for polycrystals with different number of grains with average grain diameters $< d_{\text{grain}} >= 2500\,a$, $< d_{\text{grain}} >= 740\,a$ and $< d_{\text{grain}} >= 312.5\,a$. Microstructure snapshots of the polycrystal with (b) $< d_{\text{grain}} >= 312.5\,a$ during compression of the third cycle, (c) $< d_{\text{grain}} >= 740\,a$ during compression of the first cycle and (d) $< d_{\text{grain}} >= 2500\,a$ tension maximum of the first cycle. Dislocation coloring is according the grain number.

5. Summary and conclusion

In this work, DDD simulations of early stage low-amplitude fatigue were conducted for *fcc*- and *bcc* metals. For a deeper understanding of the underlying physical mechanisms during cyclic loading, analysis tools, based on a graph, were developed. The procedure enables the extraction of irreversible microstructural components, which are critical during fatigue, such as prismatic loops and generalized dislocation dipoles for further geometrical characterization. As an aim to describe the dislocation structure formation, several functions which measure spatial correlation and clustering were established. Thus, a statistical foundation, based on a mathematical quantification of the dislocation microstructure was set.

***Fcc* metals** The carried out investigations showed the significant role of the grain shape in controlling the degree of irreversibility of a system. It turns out that grain boundaries oriented for screw pile-ups enhance the proliferation of plastic slip and consequently irreversible dislocation activity. This means that the grain shape needs to be considered as an extra parameter when setting up model systems, especially since many micromechanical simulation models in the literature use cuboidal geometries. Another aspect is related to two-dimensional EBSD measurements, which lack the complete information of grain geometry. Thus, in order to understand damage development in certain grains, the three-dimensional information is required.

The grain orientation given by EBSD can be used to estimate Schmid factors, which are majorly used in the literature to determine dislocation activity in a grain. The current simulations of surface grains showed that slip system activity is controlled by both the Schmid factor and the orientation of the Burgers vector of a slip system with respect to the free surface: A slip system I is highly active provided a high Schmid factor and a large free surface component of its Burgers vector. The physical origin of this phenomenon is related to the high density of collinear reactions exhibited by slip systems II with a a high Schmid factor but small free surface component. The latter behavior enables slip systems I to reach the prescribed plastic strain faster than slip systems II resulting in a change of frequency in dislocation densities which causes a backstress on systems II obstructing their motion. Accordingly, an initial

multislip loading scenario can result in dislocation activity similar to double slip loading. This means that surface roughening, which is the cause of fatigue crack initiation in *fcc* metals, is aided by this phenomenon since dislocations with large surface components are highly active and vice versa. The findings are of importance for the analysis of polycrystalline samples. One of the key issues for fatigue damage is the identification of possible grains more susceptible to damage initiation.

Several crystal orientations were examined and were able to produce structural patterns which agree with experimental findings. In multislip loading conditions, either cellular or slip band structures with well-defined correlations emerged. Both arrangements were thoroughly analyzed and found to be controlled by extremely stable Lomer junctions that bring regular dislocations to cluster around them. A sensitivity of the microstructure with respect to a minimal crystal rotation showed that if such a rotation is to occur around the tensile axis, then the microstructure remains unaltered. However, if the crystal is to be rotated around another arbitrary axis, then the Schmid factors combined with Burgers vectors' orientation with respect to the free surface can result in a very distinctive microstructure. Relaxation simulations showed that the stability of the structures is assisted by pinned points such as those of FR-sources.

A study of the influence of plastic strain amplitudes extending from the persistent slip band threshold to the VHCF-regime showed that the nature and geometrical characteristics of irreversible defects are very similar. The main difference was seen in the evolution rate with a non-linear transition to the VHCF domain. A precise method to estimate the well-known irreversibility factor p from both the surface and the bulk was developed. With its help, it was found that even for VHCF amplitudes, where the dislocation density appears to be fully reversible, a small but gradual microstructural irreversibility was seen in the p factor. This observation is congruent with the suggested damage mechanism by Mughrabi where the accumulation of very small plastic slip over a large number of cycles leads to a surface roughening.

Outside the scope of this work, first attempts were made to extrapolate the rate of formation of irreversible defects based on the gathered statistical data and gained knowledge. The model relies on fitting the plastic strain evolution of single dislocations according to their geometrical location in the grain. Then probabilities for cross-slip, emission of a new dislocation and formation of dipoles are estimated and evaluated using a Monte Carlo method. First simulations showed good agreement with DDD, however only the tensile loading stage was modeled and has yet to be extended to unloading and compression as a future work.

***Bcc* metals** Type II metals containing non-metallic inclusions larger than the average grain size were modeled in this work using a *bcc* iron matrix and an oxide inclusion. The *bcc* dislocation model was adapted for computational efficiency using a phenomenological friction stress for screw dislocations. The inclusion was modeled as a spherical misfitting isotropic obstacle that has different material properties than the matrix. The latter properties were incorporated on the level of stress fields, where misfit stresses were analytical and modulus-induced stresses numerical.

The results showed that the interplay between the individual sectors of the stress fields plays a huge role in controlling the microstructural evolution. For instance the modulus-induced stress field determines the region of structure formation, whereas, depending on the magnitude, the misfit stress may introduce for a given Burgers vector a third cross-slip region and ensure the stability of the structure.

The influence of the inclusion radius was studied and shown to play a significant role only when the inclusion possessed a misfit strain. Therefore, the misfit should be considered as an extra parameter in modeling fatigue crack initiation at an inclusion. For instance, the prominent Murakami $\sqrt{area}$ model only considers the geometry of the inclusion.

The findings suggest that longer fatigue life can be achieved by reducing the inclusion misfit and radius. Also multislip orientations, for which the modulus-induced stress fields yield complex cross-slip domains, are adverse for plastic reversibility.

Appendix

A. Grain construction algorithm

A grain is defined by a centroid of position $\boldsymbol{x}_{\text{centroid}}$ and a number of planes, where a plane i has a normal vector $\boldsymbol{n_i}$ pointing to the outside and a distance d_{centroid_i} from the centroid. To construct the grain, first all possible plane intersections need to be computed followed by line intersections. So for planes i and j to have an intersection their normals need to be not parallel which is valid if the norm of the intersection line direction $||\boldsymbol{t_k}|| > 0$ ($\boldsymbol{t_k} = \boldsymbol{n_i} \times \boldsymbol{n_j}$). A point $\boldsymbol{P_k}$ belonging to intersection line k, which is shared by both planes can be calculated by using a third plane with normal vector $\boldsymbol{e_{t_k}}$. The three planes intersect each other in the point

$$\boldsymbol{P_k} = \frac{-d_{\text{centroid}_i}(\boldsymbol{n_j} \times \boldsymbol{t_k}) - d_{\text{centroid}_j}(\boldsymbol{t_k} \times \boldsymbol{n_i})}{\boldsymbol{n_i} \cdot (\boldsymbol{n_j} \times \boldsymbol{t_k})} \tag{A.1}$$

From the list of lines gathered, plane vertices are obtained by computing line intersections. The latter is achieved by reducing the problem to two dimensions by projecting the lines onto their plane. Therefore, the intersection point of lines i and j

$$\boldsymbol{P'} = \boldsymbol{P_i} + \lambda \boldsymbol{e_{t_i}} \tag{A.2}$$

where

$$\lambda = -\frac{-(\boldsymbol{P_i} - \boldsymbol{P_j}) \cdot \boldsymbol{t_i} + (\boldsymbol{e_{t_i}} \cdot \boldsymbol{e_{t_j}})(\boldsymbol{P_i} - \boldsymbol{P_j}) \cdot \boldsymbol{t_j}}{-1 + (\boldsymbol{e_{t_i}} \cdot \boldsymbol{e_{t_j}})^2} \tag{A.3}$$

The intersection point $\boldsymbol{P'}$ needs to be inside the grain. For this reason, the point is tested against all grain boundaries i

$$(d_{\text{centroid}_i}\boldsymbol{n_i} - (\boldsymbol{P'} - \boldsymbol{x}_{\text{centroid}})) \cdot \boldsymbol{n_i} < -\epsilon \tag{A.4}$$

where ϵ denotes a very small number negligible compared to unity. If the point lies inside of the grain, then the vertex is saved. A plane having less than 3 vertices is considered not active.

In order to create a free surface, a plane with a normal vector same as that of the free surface is set at a distance larger than the free surface of the total cuboidal domain. Such plane would obtain no vertices and would be considered as inactive.

B. Interface handling algorithm

B.1 Grain boundaries

Integrating the equation of motion at time step n yields a new nodal position $\boldsymbol{x}^{\boldsymbol{n+1}}$. Before assigning the new position, the node is tested against grain boundaries to ensure it remains inside the grain. For the sake of computational efficiency, the system is discretized initially into voxels which hold the information whether they intersect a grain boundary. In the following algorithm, only nodes that lie in such voxels are tested against the grain boundaries which they intersect. For a grain boundary i, $\boldsymbol{x}^{\boldsymbol{n+1}}$ lies outside if the condition in equation A.4 is fulfilled, hence, $\boldsymbol{x}^{\boldsymbol{n+1}}$ needs to be projected back into the grain. Different cases are considered depending on the actual position $\boldsymbol{x}^{\boldsymbol{n}}$:

- $\boldsymbol{x}^{\boldsymbol{n}}$ is inside the grain:
  - If $\boldsymbol{x}^{\boldsymbol{n}}$ is at a smaller distance than $d_{\mathrm{gbs}} = 3a$ from the grain boundary, then the original position $\boldsymbol{x}^{\boldsymbol{n+1}} = \boldsymbol{x}^{\boldsymbol{n}}$ is retained.
  - Otherwise, a direction vector $\boldsymbol{t} = \boldsymbol{x}^{\boldsymbol{n+1}} - \boldsymbol{x}^{\boldsymbol{n}}$ is calculated (if not prescribed) and the new position is projected according to

$$\boldsymbol{x}^{\boldsymbol{n+1}} = \boldsymbol{x}^{\boldsymbol{n}} - \frac{0.5 d_{\mathrm{gbs}} + (\boldsymbol{x}^{\boldsymbol{n}} - \boldsymbol{x}_{\mathrm{ref}_i}) \cdot \boldsymbol{n_i}}{\boldsymbol{n_i} \cdot \boldsymbol{t}} \boldsymbol{t} \tag{B.1}$$

    where $\boldsymbol{x}_{\mathrm{ref}_i}$ is a reference position on grain boundary i (see figure B.1).

- $\boldsymbol{x}^{\boldsymbol{n}}$ is on the grain boundary. If the direction vector $\boldsymbol{t}$ is not prescribed, it is set to $\boldsymbol{t} = (\boldsymbol{n_i} \times \boldsymbol{n}_{\mathrm{gp}}) \times \boldsymbol{n}_{\mathrm{gp}}$, where $\boldsymbol{n}_{\mathrm{gp}}$ is the glide plane normal. This means $\boldsymbol{t}$ lies in the glide plane and points to the grain inside. Accordingly, the projection follows

$$\boldsymbol{x}^{\boldsymbol{n+1}} = \boldsymbol{x}^{\boldsymbol{n}} - \frac{0.5 d_{\mathrm{gbs}}}{\boldsymbol{n_i} \cdot \boldsymbol{e_t}} \boldsymbol{e_t} \tag{B.2}$$

- $\boldsymbol{x^n}$ is outside the grain boundary. The glide vector $\boldsymbol{t}$ is calculated as in the latter case if not prescribed. The new nodal position is corrected according to equation B.1.

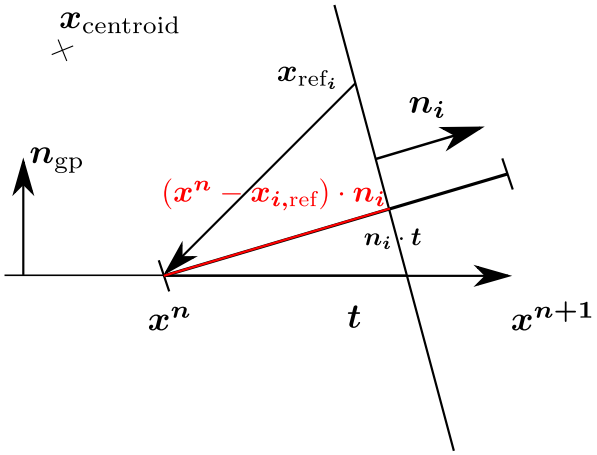

Figure B.1: Schematic visualization of the projection algorithm for the case that $\boldsymbol{x^n}$ is inside the grain and at a distance larger than d_{gbs}.

B.2 Spherical inhomogeneities

Given is a spherical inhomogeneity of radius R_p and located at $\boldsymbol{x}_{\text{center}}$. Similar to section B.1, to ensure dislocations do not cut the sphere, the algorithm projects new nodal positions predicted to lie inside of the sphere to the outside. Hence, it is distinguished whether the nodal position at time n:

- $\boldsymbol{x^n}$ is outside the sphere.
  - Then if $\boldsymbol{x^n}$ lies at a distance $R_p + d_{\text{sph}}$ from the sphere center ($d_{\text{sph}} = 3a$), the new position is retained.
  - Otherwise, the intersection point $\boldsymbol{x}_{\text{inter}}$ between $\boldsymbol{t} = \boldsymbol{x^{n+1}} - \boldsymbol{x^n}$ and the sphere which is closer to $\boldsymbol{x^n}$ is used to project out the new position:

$$\boldsymbol{x^{n+1}} = \boldsymbol{x}_{\text{inter}} + d_{\text{sph}} \boldsymbol{e_t} \tag{B.3}$$

- On the other hand, if $\boldsymbol{x^n}$ is inside of the sphere, then the following distinction is made:

– if a prescribed direction $\boldsymbol{t}$ is provided, then the intersection point $\boldsymbol{x}_{\text{inter}}$ is calculated between $\boldsymbol{x}^{\boldsymbol{n}}$ and a point which lies along $\boldsymbol{x}^{\boldsymbol{n}} + \lambda \boldsymbol{e}_{\boldsymbol{t}}$ with λ chosen such that the point is outside the sphere. Hence, the new position is calculated as in equation B.3.

– If no prescribed direction is given, then $\boldsymbol{t} = \boldsymbol{r} - \boldsymbol{r}_{\text{gp}}$ where $\boldsymbol{r} = \boldsymbol{x}^{\boldsymbol{n}} - \boldsymbol{x}_{\text{center}}$ is the vector connecting the current position with the sphere center and $\boldsymbol{r}_{\text{gp}} = (\boldsymbol{r} \cdot \boldsymbol{n}_{\text{gp}})\boldsymbol{n}_{\text{gp}}$ is the projection of $\boldsymbol{r}$ along $\boldsymbol{n}_{\text{gp}}$. Therefore the new position is projected using

$$\boldsymbol{x}^{\boldsymbol{n+1}} = \boldsymbol{x}_{\text{center}} + \boldsymbol{r}_{\text{gp}} + (d_{\text{out}} + d_{\text{sph}})\boldsymbol{e}_{\boldsymbol{t}} \tag{B.4}$$

where $d_{\text{out}} = \sqrt{R_p^2 - ||\boldsymbol{r}_{\text{gp}}||^2}$ (see figure B.2).

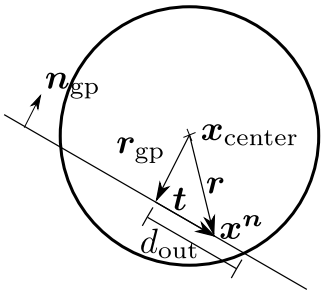

Figure B.2: Schematic visualization of the projection algorithm for the case that $\boldsymbol{x}^{\boldsymbol{n}}$ is inside the sphere without a given prescribed direction vector.

C. Validation of the inclusion stress field

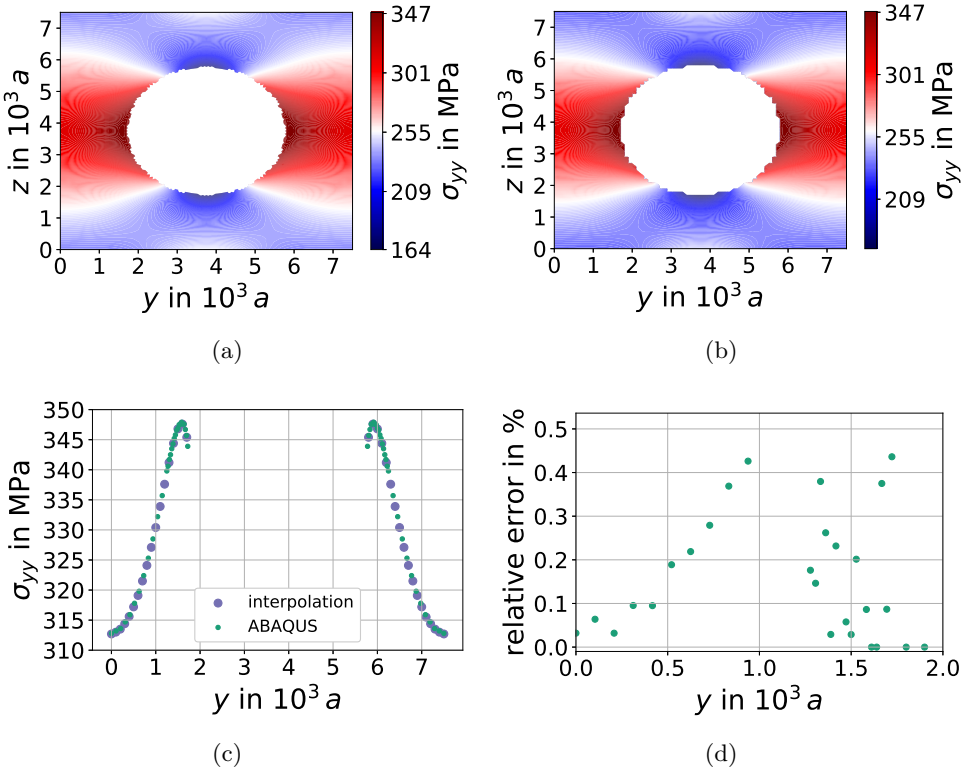

Figure C.1: Stress field interpolation from an irregular grid onto a regular one: Contour plots of a slice $x = 3750\,a$ (half the length in x-direction) of the (a) elastic stress field generated using `ABAQUS` and (b) interpolated stress field onto a regular grid. (c) Line plot along $z = 3750\,a$ from (a) and (b). The relative error between both cases is shown in (d).

D. Prismatic loops: interstitial and vacancy classification

The classification of prismatic loops according to vacancy- or interstitial types is illustrated in figure D.1. After finding all prismatic loops in the system, only prismatic loops of the 1st-order are considered. In the figure, the dotted segment with orange nodes belongs to a prismatic loop with centroid $\boldsymbol{\alpha}$ (blue node). If $\boldsymbol{n} \cdot (\boldsymbol{b} \times \boldsymbol{t}) < 0$, then the used convention is that the extra-half plane points in the glide plane normal direction $\boldsymbol{n}$. Then if $(\boldsymbol{n} \cdot \boldsymbol{p})\,(\boldsymbol{n} \cdot (\boldsymbol{b} \times \boldsymbol{t})) < 0$, the prismatic loop is of vacancy type (as in the figure), otherwise it is counted as interstitial. Here $\boldsymbol{p}$ is the vector pointing from $\boldsymbol{\alpha}$ to a segmental node.

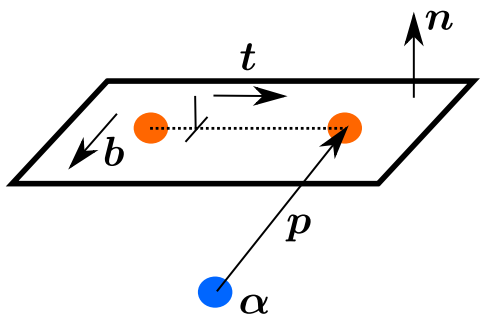

Figure D.1: Scheme to determine prismatic loop types.

Figure D.2 shows the evolution of first order prismatic loops in a [010] orientation (setup 1e) separated into vacancy and interstitial types. For the large amplitude, the curves corresponding to both types show an entanglement throughout the simulation. In the case of the small amplitude, up to 110 cycles both types are almost equal ($\approx$ 12 prismatic loops each), afterwards no increase in interstitial type prismatic loops is seen, whereas the vacancy type continues increasing to reach a maximum of 25 prismatic loops.

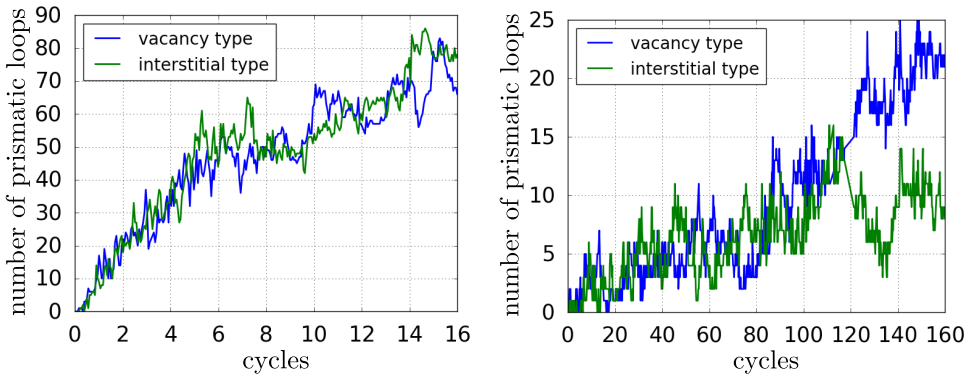

Figure D.2: Evolution of vacancy- and interstitial prismatic loops for setup 1e for (a) $\Delta\varepsilon_{\mathrm{pl}}/2 = 0.01\%$ and (b) $\Delta\varepsilon_{\mathrm{pl}}/2 = 0.001\%$ (El-Achkar und Weygand, 2019).

E. [210]-tensile axis

For a [210] double-slip orientation (Schmid factors in figure E.1), two different setups are realized:

- Setup 4a: the crystal orientation is rotated around the tensile axis such that glide system 4 has a non-significant component in the free surface direction.
- Setup 4b: both glide systems 4 and 9 have a non-vanishing equal free surface component.

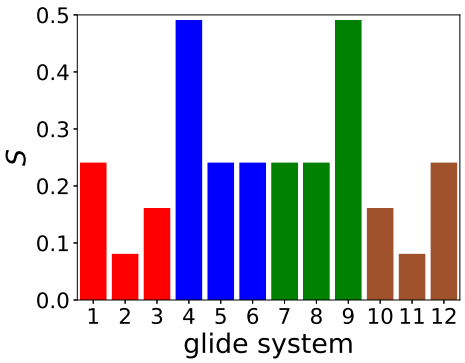

Figure E.1: Schmid factor distribution for a [210]-tensile axis orientation.

Figure E.2 shows the dislocation density evolution per glide system. It is obvious that in setup 4a that glide system 9 is highly active, whereas glide system 4 falls behind after 1 cycle. On the other hand, both glide systems are equally active in setup 4b.

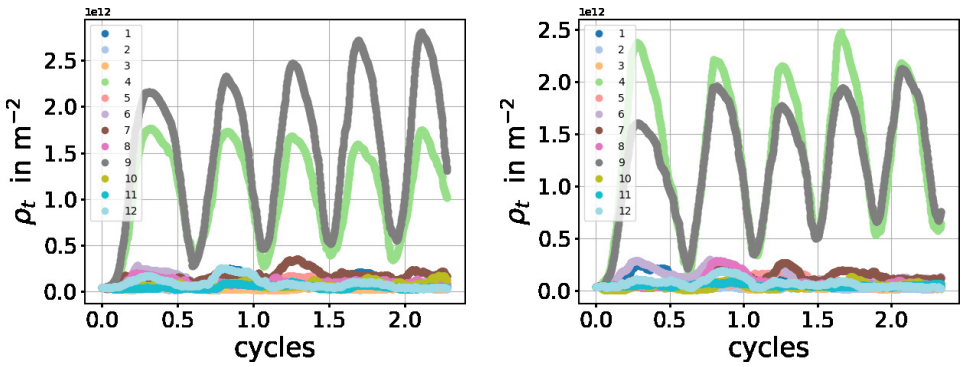

(a) (b)

Figure E.2: Dislocation density evolution per glide system for a [210]-tensile axis in setups (a) 4a and (b) 4b.

F. Sensitivity analysis of a rotation away from a [010]-tensile axis

Rotation around the tensile axis The dislocation density distribution is analyzed for different rotation angles 10°, 20°, 30° and 40° around the [010]-tensile axis. The surface components for Burgers vectors $\boldsymbol{b_2}$ (systems 7 and 11) and $\boldsymbol{b_3}$ (systems 5 and 8) for different rotation angles are given in table F.1. Figure F.1 shows that the increase in dislocation density distribution in Burgers vectors $\boldsymbol{b_3}$ and $\boldsymbol{b_4}$ (same surface component as $\boldsymbol{b_3}$) is proportional to the increase in the respective surface component. For a 10° rotation, the dislocation density in $\boldsymbol{b_3}$ and $\boldsymbol{b_4}$ is intermediate (almost half the activity compared to $\boldsymbol{b_2}$ and $\boldsymbol{b_5}$), whereas for a 40° rotation the density is almost equally distributed among $\boldsymbol{b_2}$, $\boldsymbol{b_3}$, $\boldsymbol{b_4}$ and $\boldsymbol{b_5}$.

Rotation around the z-axis A 10° rotation around the z-axis changes the Schmid factor distribution (figure F.2(a)) and yields a double slip condition of two highly active slip systems 2 and 11 (figure F.2(b)). The two systems belong to $\boldsymbol{b_5}$ and $\boldsymbol{b_2}$ respectively and favor no reactions between them. Although S is high for systems 5, 8, 1 and 12 ($\boldsymbol{b_3}$ and $\boldsymbol{b_4}$ respectively), the dislocation density is negligible in them. The latter has a drastic influence on the microstructural evolution (figures F.2(c)

Rotation angle	$\lvert \boldsymbol{e}_{\boldsymbol{b_2}} \cdot \boldsymbol{n}_{\mathrm{surf}} \rvert$	$\lvert \boldsymbol{e}_{\boldsymbol{b_3}} \cdot \boldsymbol{n}_{\mathrm{surf}} \rvert$
0° (setup 1e)	0.707	0
10°	0.696	0.122
20°	0.664	0.241
30°	0.612	0.353
40°	0.541	0.454
45° (setup 1f)	0.5	0.5

Table F.1: Chosen rotation angles of the crystal around the axis [010] and surface components of Burgers vectors $\boldsymbol{b_2}$ and $\boldsymbol{b_3}$. Burgers vectors $\boldsymbol{b_5}$ and $\boldsymbol{b_4}$ are omitted because they have the same surface components as $\boldsymbol{b_2}$ and $\boldsymbol{b_3}$ respectively, whereas $\boldsymbol{b_1}$ and $\boldsymbol{b_6}$ have a zero Schmid factor $S = 0$.

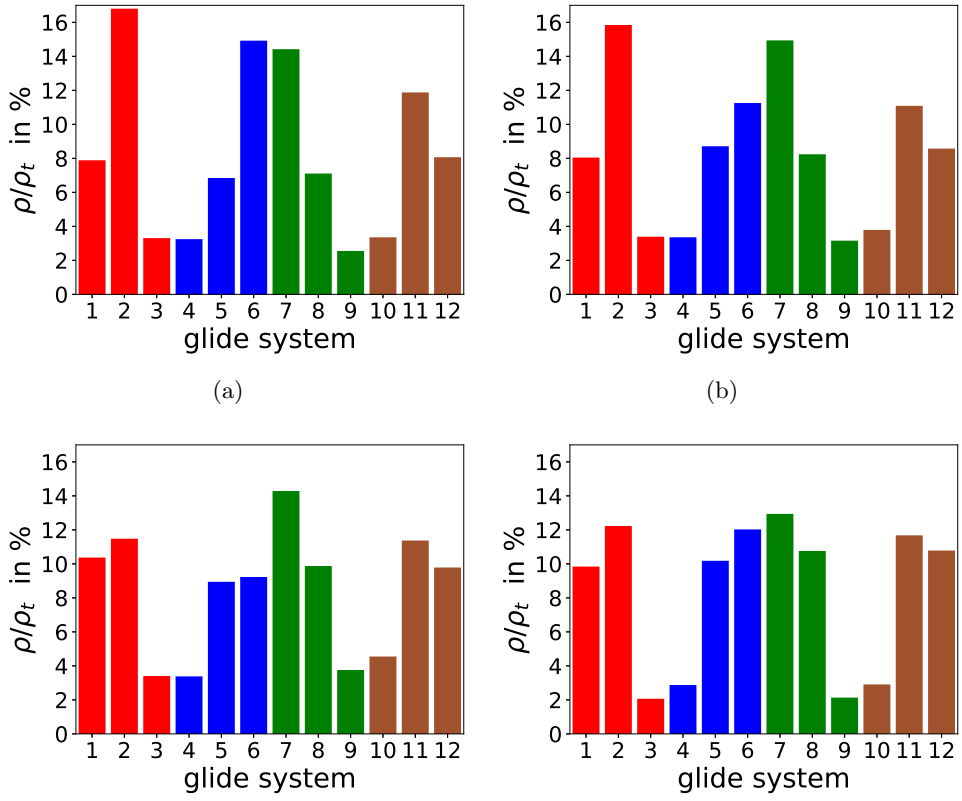

Figure F.1: Final distribution of the fraction of the dislocation density ρ per glide system w.r.t. the total dislocation density for a rotation around the tensile axis of (a) 10°, (b) 20°, (c) 30° and (d) 40°.

and F.2(d)). After 8 cycles a rather planar pattern is observed with a small number of Lomer junctions.

Rotation to a [2 12 1]-tensile axis To investigate additional sensitivity towards a 10° rotation away from [010] which yields only one system with the highest Schmid factor, a [2 12 1]-tensile axis is simulated. The orientation is chosen such, that system 7 ($\boldsymbol{b_2}$,$\boldsymbol{n_3}$) with the highest Schmid factor S has a 2.5 times smaller S' (equation 4.1) than glide system 6 ($\boldsymbol{b_5}$,$\boldsymbol{n_2}$), which has a slightly smaller S (figure F.3). The outcome of the simulation in terms of dislocation density distribution among glide systems (figure F.3(b)) shows that glide system 6 is the most populated followed by glide systems 7, 1 and 5. In contrast to the previous setups, the glide system with the highest Schmid factor remains relevant despite the small S'. Nevertheless, its role is less important than predicted by the S distribution, which means that the effect is present, but not enough to diminish its role.

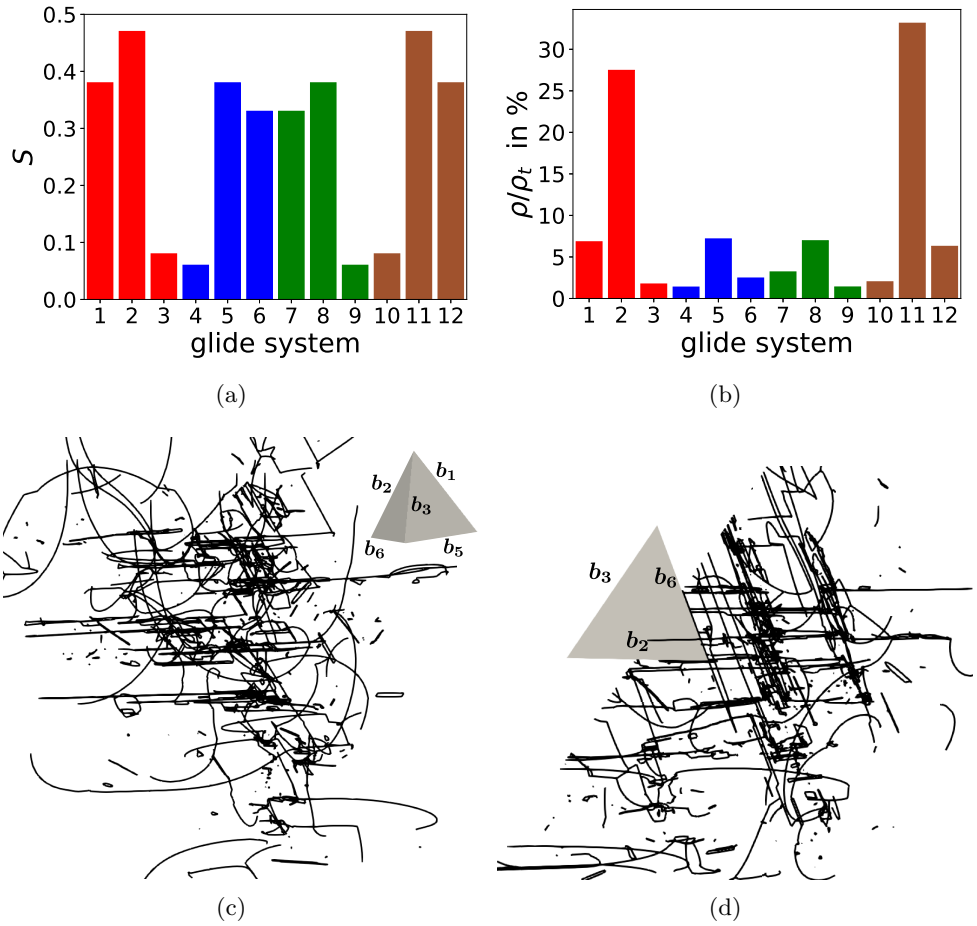

Figure F.2: (a) Schmid factor S distribution for a 10° rotation of the [010] crystal system (setup I) around the z-axis. (b) Final distribution of the fraction of the dislocation density ρ per glide system w.r.t. the total dislocation density. (c-d) Different views of the microstructure after 8 cycles (dislocation density minimum).

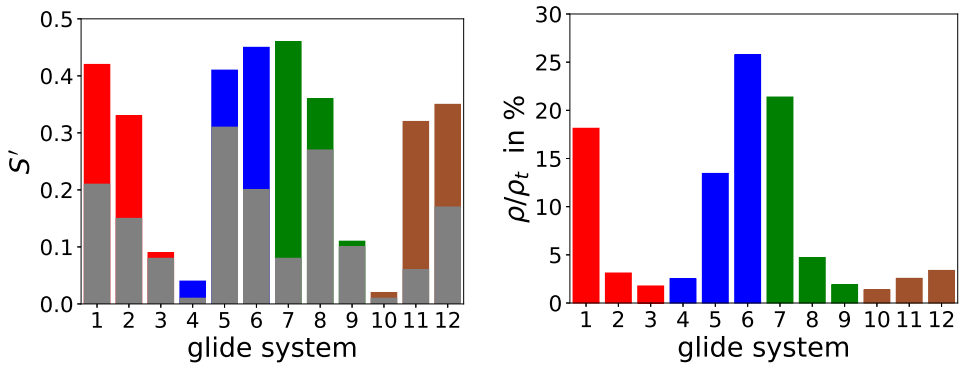

(a) (b)

Figure F.3: (a) Modified Schmid factor S' (in gray) on top of the Schmid factor for a [2 12 1] orientation 10° away from [010]. (b) Dislocation density distribution per glide system w.r.t. the total dislocation density.

G. [110]-tensile axis

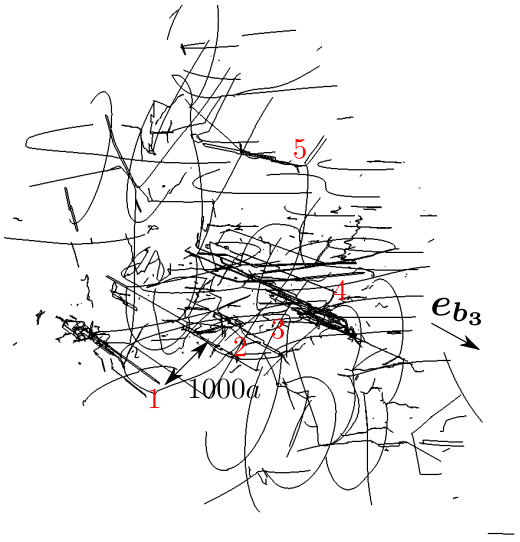

(a)

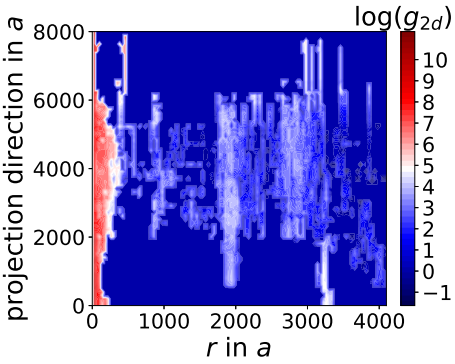

(b)

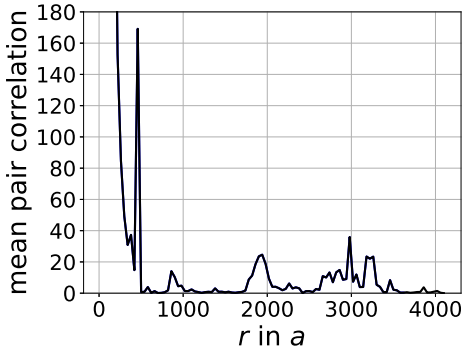

(c)

Figure G.1: (a) Dislocation microstructure of a different initial microstructure of setup 2a in a [110] orientation (section 3.1.2) showing a slip band pattern. (b) Contour plot of the correlation function g_{2d} and its mean along $\boldsymbol{b_3}$ in (c).

H. Macroscopic analysis measures

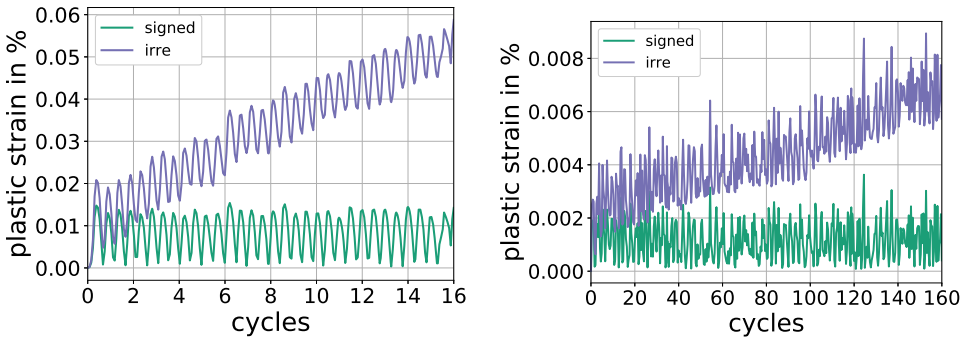

(a) (b)

Figure H.1: Evolution of the irreversible plastic strain (see section 2.2.5) and signed plastic strain for setup 1e for $\Delta\varepsilon_{\mathrm{pl}}/2 = 0.01\%$ and $\Delta\varepsilon_{\mathrm{pl}}/2 = 0.001\%$ in (a) and (b) respectively.

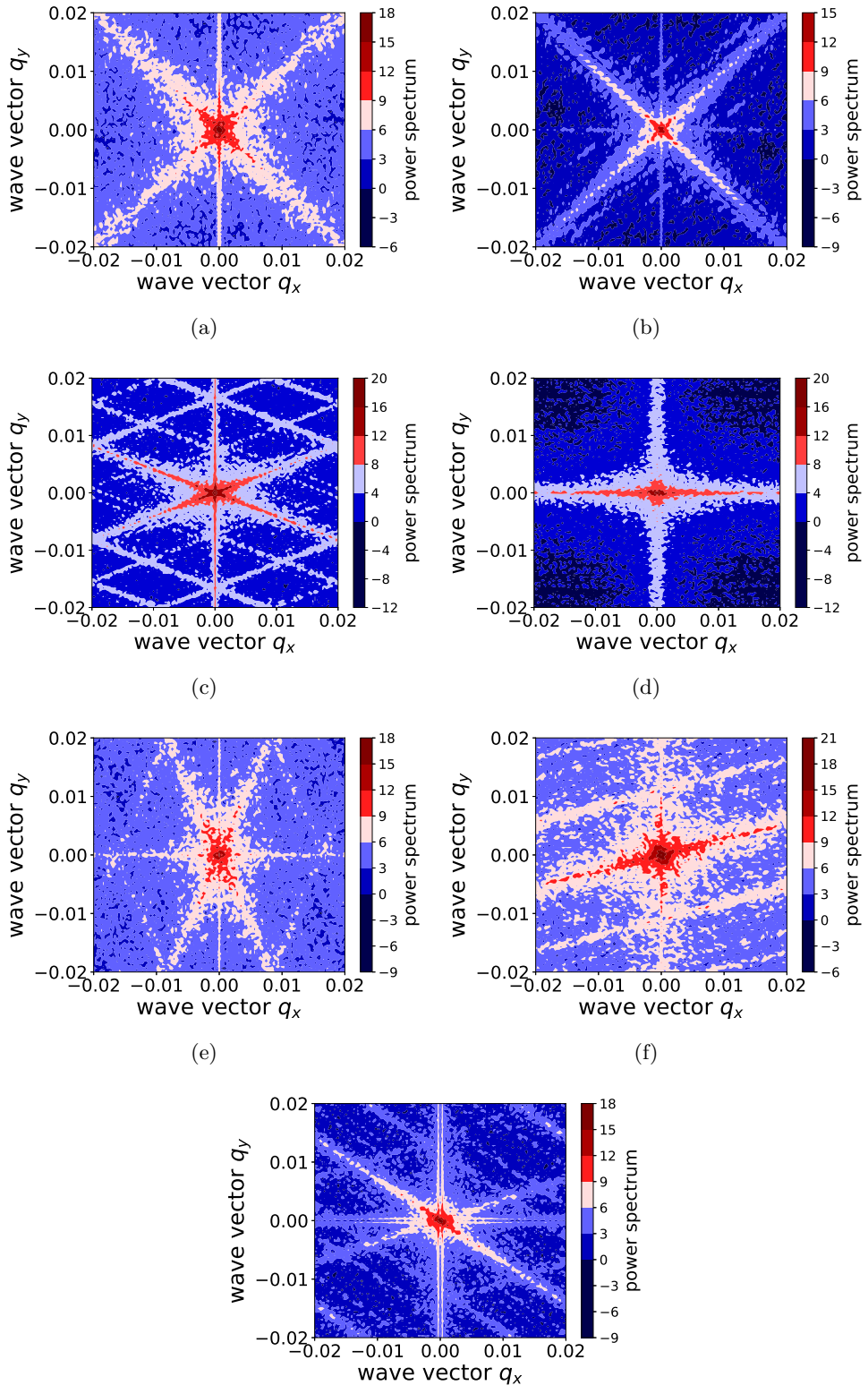

Figure H.2: Power spectral density of surface displacements for a [010] tensile axis orientation (setup 1e) in (a) $\Delta\varepsilon_{\mathrm{pl}}/2 = 0.01\%$ and (b) $\Delta\varepsilon_{\mathrm{pl}}/2 = 0.001\%$ after 16- and 160 cycles respectively, (c) setup 2a of [110] tensile axis after 1 cycle, (d) setup 2b of [110] tensile axis after 1 cycle, (e) for $\Delta\varepsilon_{\mathrm{pl}}/2 = 0.01\%$ in a [111] tensile axis orientation after 2.5 cycles, (f) setup 3e: $\Delta\varepsilon_{\mathrm{pl}}/2 = 0.084\%$ in a [982] tensile axis orientation (only glide system 9) after 3 cycles, (g) [112] tensile axis orientation after 1 cycle.

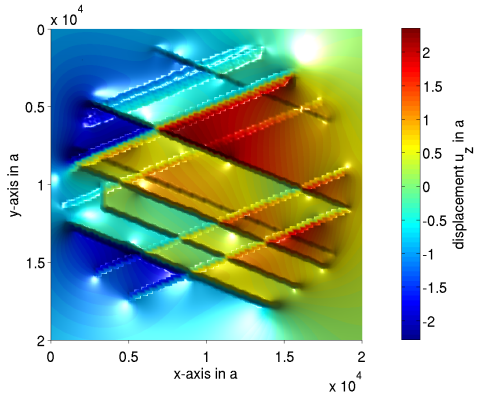

(a)

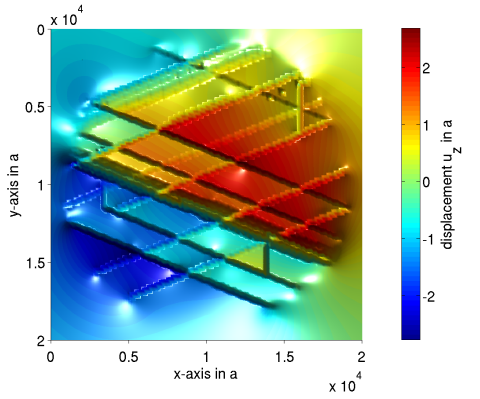

(b)

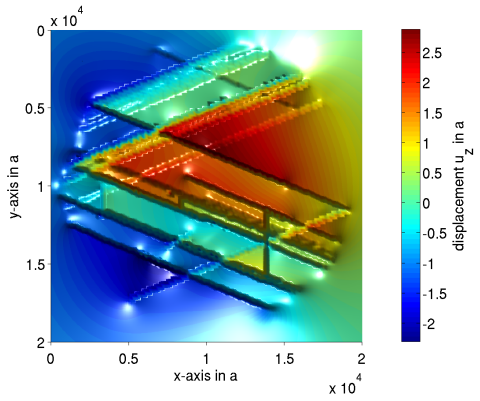

(c)

Figure H.3: Surface evolution in a [110] crystal orientation (setup 2a) for load maxima of cycles (a) 1, (b) 2 and (c) 6.

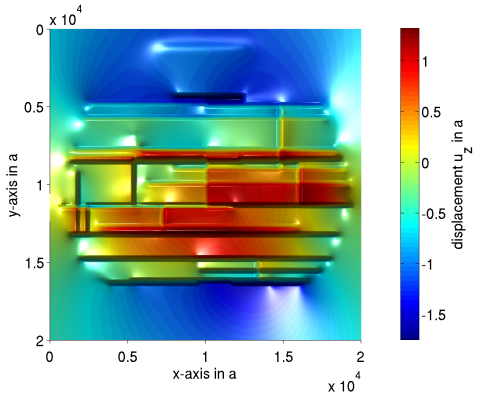

(a)

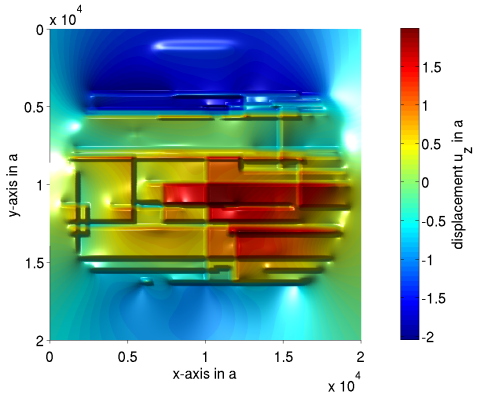

(b)

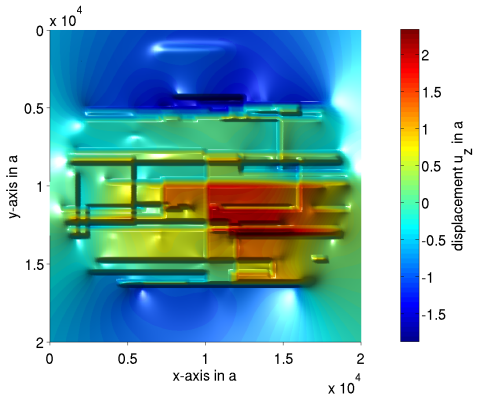

(c)

Figure H.4: Surface evolution in a [110] crystal orientation (setup 2b) for load maxima of cycles (a) 1, (b) 4 and (c) 6.

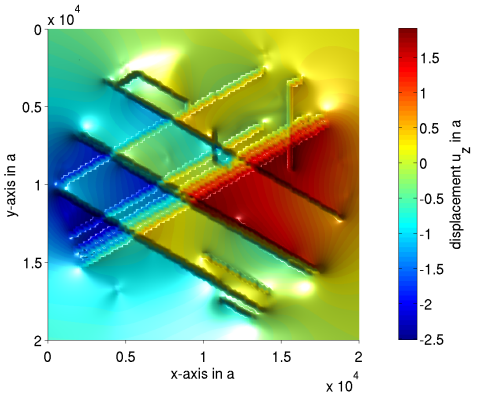

(a)

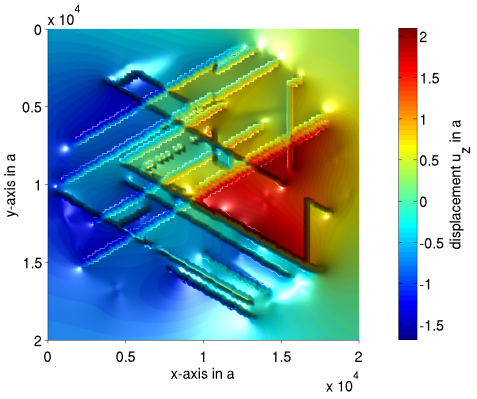

(b)

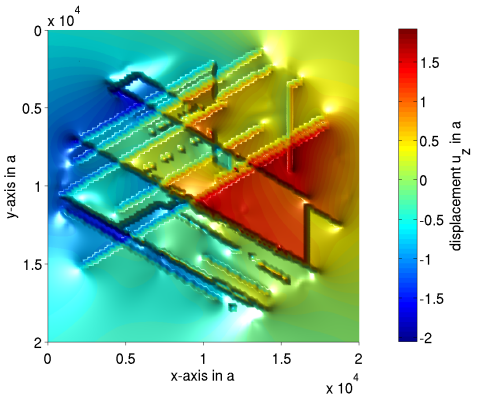

(c)

Figure H.5: Surface evolution in a [110] crystal orientation (setup 2c) for load maxima of cycles (a) 1, (b) 3 and (c) 5.

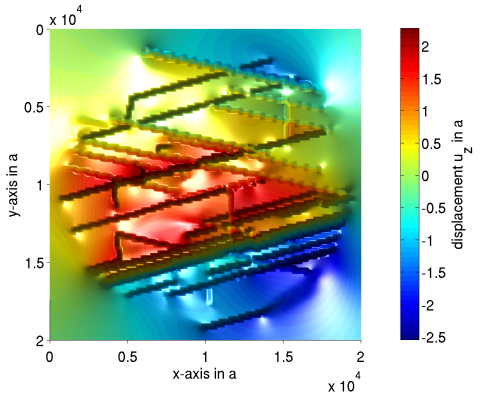

(a)

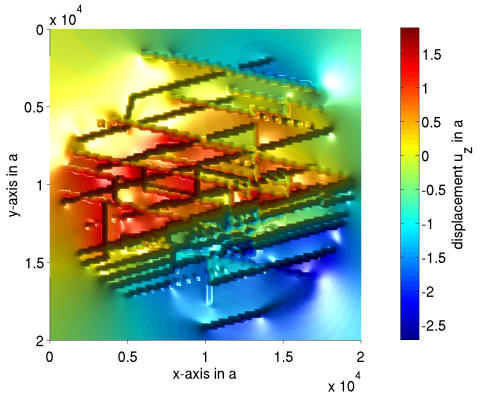

(b)

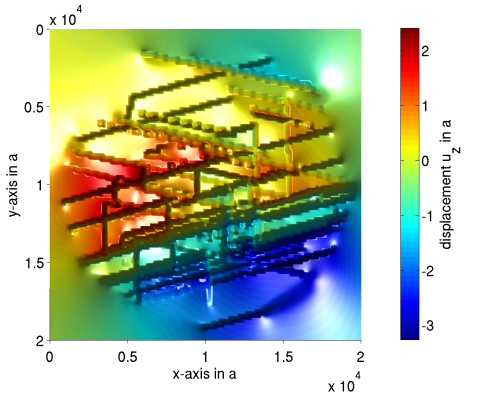

(c)

Figure H.6: Surface evolution for setup 3a in a [982] crystal orientation with all glide systems (microstructure in figure 3.29(a)) for load maxima of cycles (a) 1, (b) 3 and (c) 5.

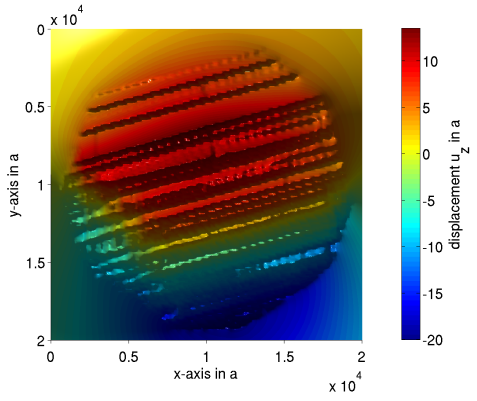

(a)

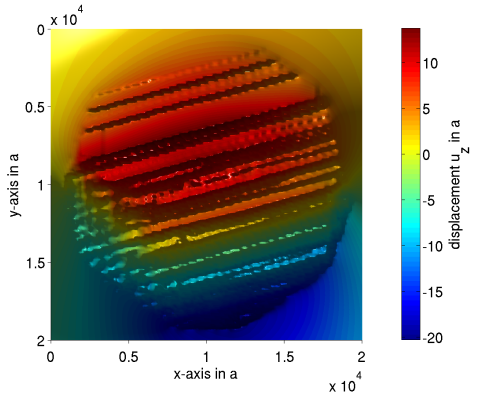

(b)

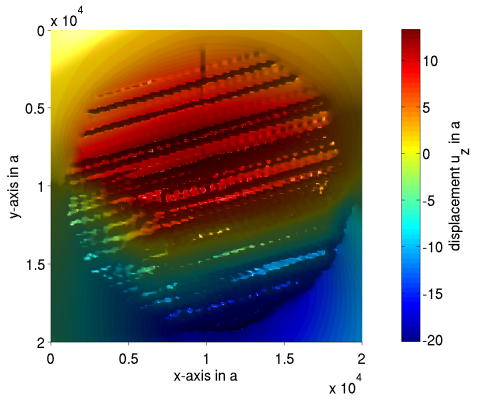

(c)

Figure H.7: Surface evolution for setup 3e in a [982] crystal orientation using only glide system 9 for load maxima of cycles (a) 1, (b) 2 and (c) 3.

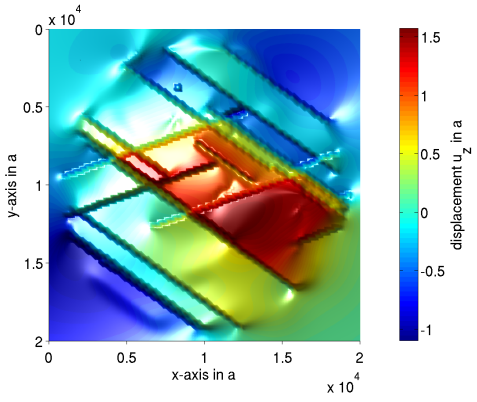

(a)

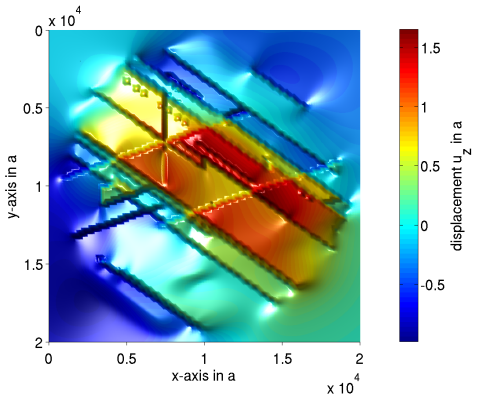

(b)

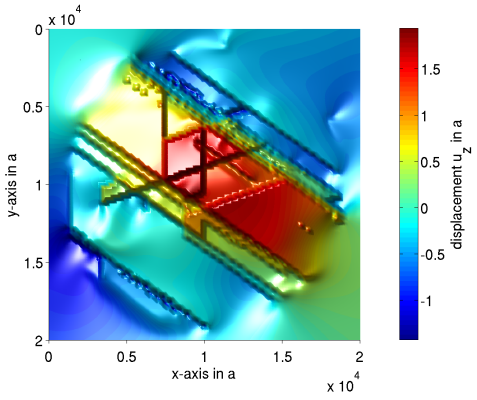

(c)

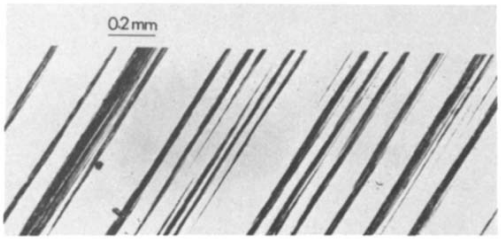

(d)

Figure H.8: Extrusion development in a [112] crystal orientation for load maxima of cycles (a) 1, (b) 2 and (c) 4. (d) [$\bar{1}$12] crystal surface after Jin und Winter (1984a).

I. Plastic strain tensor analysis

Consider the plastic strain tensor $\boldsymbol{\varepsilon_{pl}} = A_{\text{swept}}/(2V_{\text{av}})(\boldsymbol{b}\otimes\boldsymbol{n}+\boldsymbol{n}\otimes\boldsymbol{b})$ where A_{swept} is the swept area of a dislocation in an averaging volume V_{av}. For dislocations belonging to glide system 1 ($\boldsymbol{b_4} = a/2[110]$ and $\boldsymbol{n_1} = (1\bar{1}\bar{1})$), the plastic strain tensor reads

$$\begin{aligned}
\boldsymbol{\varepsilon_{pl}}(\boldsymbol{b_4},\boldsymbol{n_4}) &= \frac{a/2A_{\text{swept}}}{2V_{\text{av}}}\left[\begin{pmatrix}1\\1\\0\end{pmatrix}(1\,\bar{1}\,1)+\begin{pmatrix}1\\\bar{1}\\0\end{pmatrix}(1\,1\,0)\right]\\
&= \frac{a/2A_{\text{swept}}}{2V_{\text{av}}}\left[\begin{pmatrix}1&1&0\\\bar{1}&\bar{1}&0\\1&1&0\end{pmatrix}+\begin{pmatrix}1&\bar{1}&1\\1&\bar{1}&1\\0&0&0\end{pmatrix}\right]\\
&= \frac{a/2A_{\text{swept}}}{2V_{\text{av}}}\begin{pmatrix}2&0&1\\&\bar{2}&1\\\text{symm.}&&0\end{pmatrix}
\end{aligned}$$

Generally for $\boldsymbol{b_4}$ dislocations, the plastic strain tensor has the form

$$\boldsymbol{\varepsilon_{pl}}(\boldsymbol{b_4}) = \begin{pmatrix}\varepsilon_{\text{pl},xx}&0&\varepsilon_{\text{pl},xz}\\&\varepsilon_{\text{pl},yy}&\varepsilon_{\text{pl},yz}\\\text{symm.}&&0\end{pmatrix} \tag{I.1}$$

For dislocations of Burgers vector $\boldsymbol{b_5} = a/2[01\bar{1}]$, it has the form

$$\boldsymbol{\varepsilon_{pl}}(\boldsymbol{b_5}) = \begin{pmatrix}0&\varepsilon_{\text{pl},xy}&\varepsilon_{\text{pl},xz}\\&\varepsilon_{\text{pl},yy}&0\\\text{symm.}&&\varepsilon_{\text{pl},zz}\end{pmatrix} \tag{I.2}$$

Both Burgers vectors can relax the applied boundary condition in y-direction since they are symmetric w.r.t. the tensile axis. However, only $\boldsymbol{b_5}$ produces plastic strain in the free surface direction z which means that a free surface maximizes plastic strain relaxed in its direction enabling glide systems that possess such property. This implies that the extrusion/intrusion formation in surface grains (Essmann et al., 1981) is more favorable due to the presented mechanism.

J. Glide system numbering and combinations to form Lomer junctions

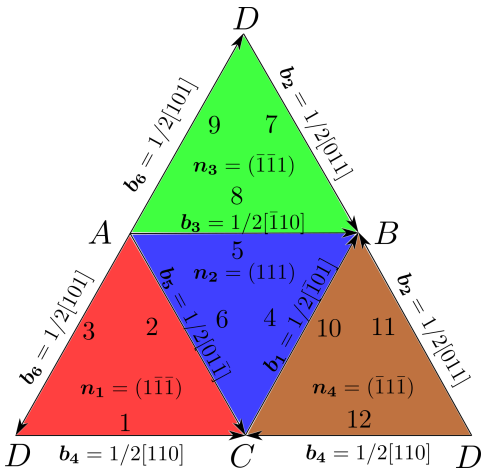

Figure J.1: *fcc* glide system numbering illustrated using a 2d-collapsed Thompson-tetrahedron.

In figure J.2 required combinations of glide systems to form a Lomer junction of a certain Burgers vector are given. For example to obtain a Lomer junction of Burgers vector $\boldsymbol{b_1}$, a reaction between glide systems 1 and 7 or glide systems 8 and 2 is needed.

Burgersvector of Lomer reaction	glide systems' combinations
$\boldsymbol{b_1}$	1 7 or 8 2
$\boldsymbol{b_2}$	3 5 or 4 1
$\boldsymbol{b_3}$	2 10 or 11 3
$\boldsymbol{b_4}$	6 9 or 7 4
$\boldsymbol{b_5}$	10 8 or 9 12
$\boldsymbol{b_6}$	5 11 or 12 6

Figure J.2: Required combinations of glide systems to form a Lomer junction in *fcc*.

Glide system	Normals vector	Burgers vector
1	$\boldsymbol{n_1} = (110)$	$\boldsymbol{b_1} = [1\bar{1}1]$
2	$\boldsymbol{n_1} = (110)$	$\boldsymbol{b_2} = [\bar{1}11]$
3	$\boldsymbol{n_2} = (101)$	$\boldsymbol{b_2} = [\bar{1}11]$
4	$\boldsymbol{n_2} = (101)$	$\boldsymbol{b_3} = [11\bar{1}]$
5	$\boldsymbol{n_3} = (011)$	$\boldsymbol{b_1} = [1\bar{1}1]$
6	$\boldsymbol{n_3} = (011)$	$\boldsymbol{b_3} = [11\bar{1}]$
7	$\boldsymbol{n_4} = (\bar{1}10)$	$\boldsymbol{b_3} = [11\bar{1}]$
8	$\boldsymbol{n_4} = (\bar{1}10)$	$\boldsymbol{b_4} = [111]$
9	$\boldsymbol{n_5} = (\bar{1}01)$	$\boldsymbol{b_1} = [1\bar{1}1]$
10	$\boldsymbol{n_5} = (\bar{1}01)$	$\boldsymbol{b_4} = [111]$
11	$\boldsymbol{n_6} = (0\bar{1}1)$	$\boldsymbol{b_2} = [\bar{1}11]$
12	$\boldsymbol{n_6} = (0\bar{1}1)$	$\boldsymbol{b_4} = [111]$

Table J.1: *bcc* glide systems' nomenclature.

K. Misorientation calculation

For each discretization voxel the infinitesimal rotation tensor $\boldsymbol{W}$ can be written as a rotation vector $\boldsymbol{\omega} = (-W_{23}, W_{13}, -W_{12})^{\mathrm{T}}$. Then a rotation matrix $\boldsymbol{R}$ can be calculated

$$\boldsymbol{R} = \cos(\alpha)\boldsymbol{I} + (1 - \cos(\alpha))(\boldsymbol{e}_{\boldsymbol{\omega}} \otimes \boldsymbol{e}_{\boldsymbol{\omega}}) + \sin(\alpha)\boldsymbol{e}_{\boldsymbol{\omega}} \tag{K.1}$$

where the angle $\alpha = ||\boldsymbol{\omega}||$.

Then the misorientation angle ω_{mis} can be estimated from

$$\omega_{\mathrm{mis}} = \arccos\left(\frac{1}{2}\mathrm{tr}\left(\boldsymbol{R}_{\mathrm{ref}}\boldsymbol{R}^{-1} - 1\right)\right) \tag{K.2}$$

where $\boldsymbol{R}_{\mathrm{ref}}$ is the rotation matrix of a reference voxel (Sutton et al., 1995).

L. Influence of the misfit strain

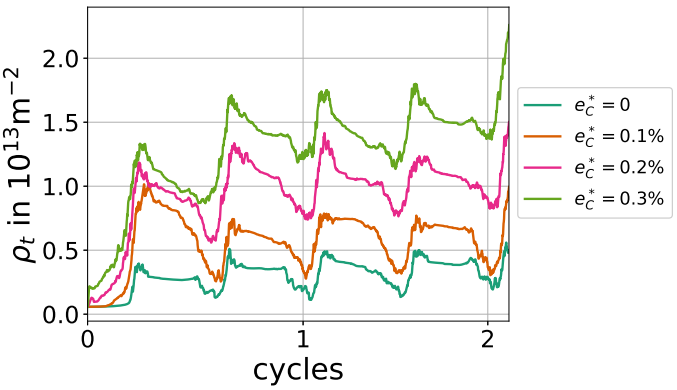

Figure L.1: Influence of the misfit strain on the dislocation density evolution for the $[19\bar{1}]$ setup from section 3.2.1 for $\Delta\varepsilon_{\mathrm{tot}}/2 = 0.12\%$.

M. Cyclic- vs. monotonic loading

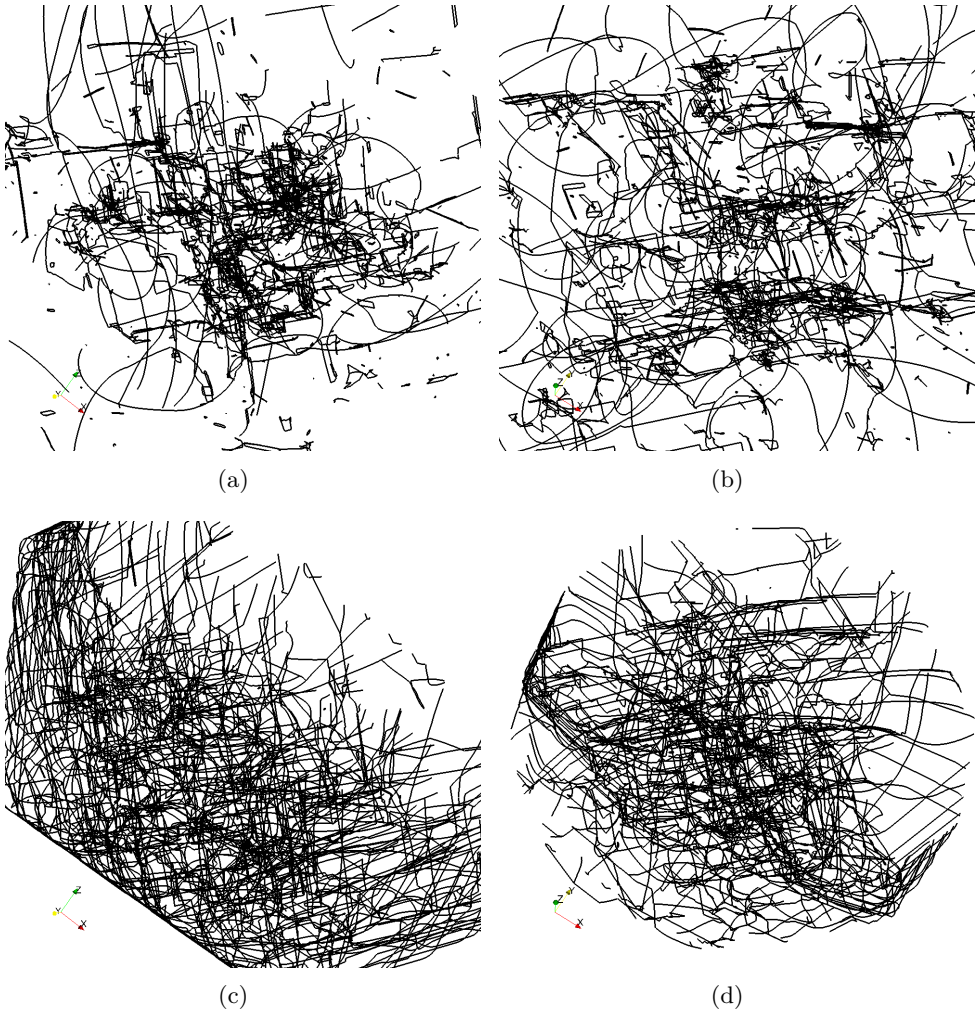

(a) (b) (c) (d)

Figure M.1: Two different perspectives of the microstructure of a [010] tensile axis (setup 1e) for (a-b) cyclic loading after 16 cycles ($\Delta\varepsilon_{\mathrm{pl}}/2 = 0.01\%$) and (b-c) monotonic tensile loading after 0.31% total strain ($\approx 0.19\%$ plastic strain) followed by a relaxation and FR-source elimination.

Bibliography

J. Antonopoulos, L. Brown, und A. Winter. Vacancy dipoles in fatigued copper. *The Philosophical Magazine: A Journal of Theoretical Experimental and Applied Physics*, 34(4):549–563, 1976.

A. Arsenlis, W. Cai, M. Tang, M. Rhee, T. Oppelstrup, G. Hommes, T. G. Pierce, und V. V. Bulatov. Enabling strain hardening simulations with dislocation dynamics. *Modelling and Simulation in Materials Science and Engineering*, 15(6):553, 2007.

E. Arzt. Size effects in materials due to microstructural and dimensional constraints: a comparative review. *Acta materialia*, 46(16):5611–5626, 1998.

M. Ashby und L. Johnson. On the generation of dislocations at misfitting particles in a ductile matrix. *Philosophical Magazine*, 20(167):1009–1022, 1969.

S. Basinski, Z. Basinski, und A. Howie. Early stages of fatigue in copper single crystals. *Philosophical Magazine*, 19(161):899–924, 1969.

Z. Basinski, A. Korbel, und S. Basinski. The temperature dependence of the saturation stress and dislocation substructure in fatigued copper single crystals. *Acta Metallurgica*, 28(2):191–207, 1980.

O. Basquin. The exponential law of endurance tests. *American Society for Testing and Materials Proceedings*, 10:625–630, 1910.

C. Bathias. There is no infinite fatigue life in metallic materials. *Fatigue and Fracture of Engineering Materials and Structures*, 22(7):559–566, 1999.

E. Bitzek und P. Gumbsch. Dynamic aspects of dislocation motion: atomistic simulations. *Materials Science and Engineering: A*, 400:40–44, 2005.

E. Bitzek, D. Weygand, und P. Gumbsch. Atomistic study of edge dislocations in fcc metals: drag and inertial effects. In *IUTAM Symposium on Mesoscopic Dynamics of Fracture Process and Materials Strength*, pages 45–57. Springer, Dordrecht, 2004.

C. Blochwitz, J. Brechbühl, und W. Tirschler. Analysis of activated slip systems in fatigue nickel polycrystals using the EBSD-technique in the scanning electron microscope. *Materials Science and Engineering: A*, 210(1-2):42–47, 1996.

T. Broom und R. Ham. The hardening of copper single crystals by fatigue. *Proceedings of the Royal Society of London. Series A*, 251(1265):186–199, 1959.

W. Cai und W. D. Nix. *Imperfections in Crystalline Solids*. Cambridge University Press, Cambridge, 2016.

G. Chai. The formation of subsurface non-defect fatigue crack origins. *International Journal of Fatigue*, 28(11):1533–1539, 2006.

G. Chai, N. Zhou, S. Ciurea, M. Andersson, und R. L. Peng. Local plasticity exhaustion in a very high cycle fatigue regime. *Scripta Materialia*, 66(10):769–772, 2012.

L. F. Coffin Jr. A study of the effects of cyclic thermal stresses on a ductile metal. *Transactions of the American Society of Mechanical Engineers, New York*, 76: 931–950, 1954.

T. H. Cormen. *Introduction to algorithms*. MIT press, Cambridge, Massachusetts, 2009.

C. Déprés, C. Robertson, und M. Fivel. Low-strain fatigue in AISI 316L steel surface grains: a three-dimensional discrete dislocation dynamics modelling of the early cycles I. dislocation microstructures and mechanical behaviour. *Philosophical Magazine*, 84(22):2257–2275, 2004.

C. Déprés, C. Robertson, und M. C. Fivel. Low-strain fatigue in 316L steel surface grains: a three dimension discrete dislocation dynamics modelling of the early cycles. Part 2: Persistent slip markings and micro-crack nucleation. *Philosophical Magazine*, 86(1):79–97, 2006.

C. Déprés, M. Fivel, und L. Tabourot. A dislocation-based model for low-amplitude fatigue behaviour of face-centred cubic single crystals. *Scripta Materialia*, 58(12): 1086–1089, 2008.

K. Differt, U. Esmann, und H. Mughrabi. A model of extrusions and intrusions in fatigued metals II. surface roughening by random irreversible slip. *Philosophical Magazine A*, 54(2):237–258, 1986.

C. Eberl. *Fatigue of Al Thin Films at Ultra High Frequencies*. PhD thesis, University of Stuttgart, Stuttgart, 2005.

T. El-Achkar und D. Weygand. Discrete dislocation dynamics study of dislocation microstructure during cyclic loading. In H.-J. Christ, editor, *Fatigue of Materials at Very High Numbers of Loading Cycles*. Springer Verlag, Wiesbaden, 2018.

T. El-Achkar und D. Weygand. Analysis of dislocation microstructure characteristics of surface grains under cyclic loading by discrete dislocation dynamics. *Modelling and Simulation in Materials Science and Engineering*, 27(5):055004, 2019.

C. Erel, G. Po, T. Crosby, und N. Ghoniem. Generation and interaction mechanisms of prismatic dislocation loops in fcc metals. *Computational Materials Science*, 140: 32–46, 2017.

J. D. Eshelby. The determination of the elastic field of an ellipsoidal inclusion, and related problems. *Proceedings of the Royal Society of London. Series A*, 241(1226): 376–396, 1957.

V. Esslinger, R. Kieselbach, R. Koller, und B. Weisse. The railway accident of Eschede–technical background. *Engineering Failure Analysis*, 11(4):515–535, 2004.

U. Essmann. Irreversibility of cyclic slip in persistent slip bands of fatigued pure fcc metals. *Philosophical Magazine A*, 45(1):171–190, 1982.

U. Essmann und H. Mughrabi. Annihilation of dislocations during tensile and cyclic deformation and limits of dislocation densities. *Philosophical Magazine A*, 40(6): 731–756, 1979.

U. Essmann, U. Gösele, und H. Mughrabi. A model of extrusions and intrusions in fatigued metals I. point-defect production and the growth of extrusions. *Philosophical Magazine A*, 44(2):405–426, 1981.

J. A. Ewing und J. Humfrey. Vi. The fracture of metals under repeated alternations of stress. *Philosophical Transactions of the Royal Society of London. Series A*, 200 (321-330):241–250, 1903.

J. A. Ewing und W. Rosenhain. Experiments in micro-metallurgy:-effects of strain. Preliminary notice. *Proceedings of the Royal Society of London*, 65(413-422):85–90, 1900.

C. Feltner. A debris mechanism of cyclic strain hardening for fcc metals. *Philosophical Magazine*, 12(120):1229–1248, 1965.

C. Feltner. The mechanism of prismatic dislocation loop formation in cyclically strained aluminium. *Philosophical Magazine*, 14(132):1219–1231, 1966.

M. Fivel, T. Gosling, und G. Canova. Implementing image stresses in a 3D dislocation simulation. *Modelling and Simulation in Materials Science and Engineering*, 4(6): 581, 1996.

J. Fourie und R. Murphy. Elongated dislocation loops and the stress-strain properties of copper single crystals. *Philosophical Magazine*, 7(82):1617–1631, 1962.

Y. Furuya. Specimen size effects on gigacycle fatigue properties of high-strength steel under ultrasonic fatigue testing. *Scripta Materialia*, 58(11):1014–1017, 2008.

J. Gilman. Influence of dislocation dipoles on physical properties. *Discussions of the Faraday Society*, 38:123–137, 1964.

B. Gong, Z. Wang, und Z. Wang. Cyclic deformation behavior and dislocation structures of [001] copper single crystals—I cyclic stress-strain response and surface feature. *Acta Materialia*, 45(4):1365–1377, 1997.

P. Grad, B. Reuscher, A. Brodyanski, M. Kopnarski, und E. Kerscher. Mechanism of fatigue crack initiation and propagation in the very high cycle fatigue regime of high-strength steels. *Scripta Materialia*, 67(10):838–841, 2012.

L. Greengard und V. Rokhlin. A fast algorithm for particle simulations. *Journal of Computational Physics*, 73(2):325–348, 1987.

J. Grosskreutz und P. Waldow. Substructure and fatigue fracture in aluminum. *Acta Metallurgica*, 11(7):717–724, 1963.

P. Hähner, K. Bay, und M. Zaiser. Fractal dislocation patterning during plastic deformation. *Physical Review Letters*, 81(12):2470, 1998a.

P. Hähner, B. Tippelt, und C. Holste. On the dislocation dynamics of persistent slip bands in cyclically deformed fcc metals. *Acta Materialia*, 46(14):5073–5084, 1998b.

J. P. Hirth und J. Lothe. *Theory of Dislocations*. John Wiley & Sons, New York, 1982.

U. Holzwarth und U. Essmann. The evolution of persistent slip bands in copper single crystals. *Applied Physics A*, 57(2):131–141, 1993.

Y. Hong und C. Sun. The nature and the mechanism of crack initiation and early growth for very-high-cycle fatigue of metallic materials–an overview. *Theoretical and Applied Fracture Mechanics*, 92:331–350, 2017.

Y. Hong, Z. Lei, C. Sun, und A. Zhao. Propensities of crack interior initiation and early growth for very-high-cycle fatigue of high strength steels. *International Journal of Fatigue*, 58:144–151, 2014.

Y. Hong, X. Liu, Z. Lei, und C. Sun. The formation mechanism of characteristic region at crack initiation for very-high-cycle fatigue of high-strength steels. *International Journal of Fatigue*, 89:108–118, 2016.

H. W. Höppel. Mechanical properties of ultrafine grained metals under cyclic and monotonic loads: an overview. In *Materials Science Forum*, volume 503, pages 259–266. Trans Tech Publ, Switzerland, 2006.

D. Hull und D. J. Bacon. *Introduction to Dislocations*. Butterworth-Heinemann, Oxford, fifth edition edition, 2001.

F. Humphreys und P. B. Hirsch. The deformation of single crystals of copper and copper-zinc alloys containing alumina particles-II. Microstructure and dislocation-particle interactions. *Proceedings of the Royal Society of London. Series A*, 318 (1532):73–92, 1970.

A. M. Hussein und J. A. El-Awady. Quantifying dislocation microstructure evolution and cyclic hardening in fatigued face-centered cubic single crystals. *Journal of the Mechanics and Physics of Solids*, 91:126–144, 2016a.

A. M. Hussein und J. A. El-Awady. Surface roughness evolution during early stages of mechanical cyclic loading. *International Journal of Fatigue*, 87:339–350, 2016b.

D. Jeddi und T. Palin-Luc. A review about the effects of structural and operational factors on the gigacycle fatigue of steels. *Fatigue & Fracture of Engineering Materials & Structures*, 41(5):969–990, 2018.

N. Jin und A. Winter. Cyclic deformation of copper single crystals oriented for double slip. *Acta Metallurgica*, 32(7):989–995, 1984a.

N. Jin und A. Winter. Dislocation structures in cyclically deformed [001] copper crystals. *Acta Metallurgica*, 32(8):1173–1176, 1984b.

I. Jolliffe. *Principal Component Analysis*. Springer Series in Statistics. Springer New York, 2013.

C. Kirsch. Die Theorie der Elastizität und die Bedürfnisse der Festigkeitslehre. *Zeitschrift des Vereines Deutscher Ingenieure*, 42:797–807, 1898.

F. Kroupa. Dislocation dipoles and dislocation loops. *Le Journal de Physique Colloques*, 27(C3):C3–154, 1966.

L. Kubin und G. Canova. The modelling of dislocation patterns. *Scripta Materialia*, 27(8):957–962, 1992.

L. Kubin, G. Canova, M. Condat, B. Devincre, V. Pontikis, und Y. Bréchet. Dislocation microstructures and plastic flow: a 3D simulation. In *Solid State Phenomena*, volume 23, pages 455–472. Trans Tech Publ, Switzerland, 1992.

L. Kubin, B. Devincre, und M. Tang. Mesoscopic modelling and simulation of plasticity in fcc and bcc crystals: Dislocation intersections and mobility. *Journal of Computer-Aided Materials Design*, 5(1):31–54, Jan 1998.

C. Laird, P. Charsley, und H. Mughrabi. Low energy dislocation structures produced by cyclic deformation. *Materials Science and Engineering*, 81:433–450, 1986.

C. Lemarchand, J. Chaboche, B. Devincre, und L. Kubin. Multiscale modelling of plastic deformation. *Le Journal de Physique IV*, 9(PR9):Pr9–271, 1999.

C. Lemarchand, B. Devincre, und L. Kubin. Homogenization method for a discrete-continuum simulation of dislocation dynamics. *Journal of the Mechanics and Physics of Solids*, 49(9):1969–1982, 2001.

P. Li, Z. Zhang, S. Li, und Z. Wang. Cyclic deformation and fatigue damage behaviors of oriented ag single crystal. *Philosophical Magazine*, 89(32):2903–2920, 2009.

F. Louchet und L. Kubin. Dislocation substructures in the anomalous slip plane of single crystal niobium strained at 50 K. *Acta Metallurgica*, 23(1):17–21, 1975.

P. Lukáš, M. Klesnil, und J. Krejčí. Dislocations and persistent slip bands in copper single crystals fatigued at low stress amplitude. *Physica Status Solidi (b)*, 27(2): 545–558, 1968.

P. Lukáš, M. Klesnil, und J. Polak. High cycle fatigue life of metals. *Materials Science and Engineering*, 15(2-3):239–245, 1974.

R. Madec, B. Devincre, und L. Kubin. Simulation of dislocation patterns in multislip. *Scripta Materialia*, 47(10):689–695, 2002.

R. Madec, B. Devincre, L. Kubin, T. Hoc, und D. Rodney. The role of collinear interaction in dislocation-induced hardening. *Science*, 301(5641):1879–1882, 2003.

J. Man, K. Obrtlik, C. Blochwitz, und J. Polak. Atomic force microscopy of surface relief in individual grains of fatigued 316L austenitic stainless steel. *Acta Materialia*, 50(15):3767–3780, 2002.

J. Man, P. Klapetek, O. Man, A. Weidner, K. Obrtlík, und J. Polák. Extrusions and intrusions in fatigued metals. part 2. AFM and EBSD study of the early growth of extrusions and intrusions in 316L steel fatigued at room temperature. *Philosophical Magazine*, 89(16):1337–1372, 2009.

S. S. Manson. *Behavior of materials under conditions of thermal stress*. National Advisory Committee for Aeronautics, Cleveland, Ohio, 1954.

C. Marichal, K. Srivastava, D. Weygand, S. Van Petegem, D. Grolimund, P. Gumbsch, und H. Van Swygenhoven. Origin of anomalous slip in tungsten. *Physical Review Letters*, 113(2):025501, 2014.

H. Matsui und H. Kimura. Anomalous {110} slip in high-purity molybdenum single crystals and its comparison with that in V(a) metals. *Materials Science and Engineering*, 24(2):247–256, 1976.

J. Morrow. Cyclic plastic strain energy and fatigue of metals. In *Internal friction, damping, and cyclic plasticity*, pages 45–87. ASTM International, West Conshohocken, PA, 1965.

N. Mott und F. N. Nabarro. An attempt to estimate the degree of precipitation hardening, with a simple model. *Proceedings of the Physical Society*, 52(1):86, 1940.

C. Motz, D. Weygand, J. Senger, und P. Gumbsch. Initial dislocation structures in 3-D discrete dislocation dynamics and their influence on microscale plasticity. *Acta Materialia*, 57(6):1744–1754, 2009.

H. Mughrabi. Microscopic mechanisms of metal fatigue. In *Strength of Metals and Alloys*, pages 1615–1638. Elsevier, 1979.

H. Mughrabi. Dislocation wall and cell structures and long-range internal stresses in deformed metal crystals. *Acta Metallurgica*, 31(9):1367–1379, 1983.

H. Mughrabi. On the life-controlling microstructural fatigue mechanisms in ductile metals and alloys in the gigacycle regime. *Fatigue and Fracture of Engineering Materials and Structures*, 22(7):633, 1999.

H. Mughrabi. Specific features and mechanisms of fatigue in the ultrahigh-cycle regime. *International Journal of Fatigue*, 28(11):1501–1508, 2006.

H. Mughrabi. Cyclic slip irreversibilities and the evolution of fatigue damage. *Metallurgical and Materials Transactions B*, 40(4):431–453, 2009.

H. Mughrabi. Fatigue, an everlasting materials problem-still en vogue. *Procedia Engineering*, 2(1):3–26, 2010.

H. Mughrabi, R. Wang, K. Differt, und U. Essmann. Fatigue crack initiation by cyclic slip irreversibilities in high-cycle fatigue. In *Fatigue Mechanisms: Advances in Quantitative Measurement of Physical Damage*. ASTM International, West Conshohocken, PA, 1983.

L. B. Munday, J. C. Crone, und J. Knap. Prismatic and helical dislocation loop generation from defects. *Acta Materialia*, 103:217–228, 2016.

Y. Murakami. Inclusion rating by statistics of extreme values and its application to fatigue strength prediction and quality control of materials. *Journal of Research-National Institute of Standards and Technology*, 99:345–345, 1994.

Y. Murakami, T. Toriyama, K. Tsubota, und K. Furumura. What happens to the fatigue limit of bearing steel without nonmetallic inclusions?: Fatigue strength of electron beam remelted super clean bearing steel. In *Bearing Steels: Into the 21st Century*, pages 87–105. ASTM International, West Conshohocken, PA, 1998.

Y. Murakami, T. Nomoto, T. Ueda, und Y. Murakami. On the mechanism of fatigue failure in the superlong life regime (N> 107 cycles). Part I: influence of hydrogen trapped by inclusions. *Fatigue & Fracture of Engineering Materials & Structures*, 23(11):893–902, 2000a.

Y. Murakami, T. Nomoto, T. Ueda, und Y. Murakami. On the mechanism of fatigue failure in the superlong life regime (N> 107 cycles). Part II: influence of hydrogen trapped by inclusions. *Fatigue & Fracture of Engineering Materials & Structures*, 23(11):903–910, 2000b.

Nishijima und Kanazawa. Stepwise S-N curve and fish-eye failure in gigacycle fatigue. *Fatigue & Fracture of Engineering Materials & Structures*, 22(7):601–607, 1999.

A. Plumtree und L. D. Pawlus. Substructural developments during strain cycling of wavy slip mode metals. In *Basic Questions in Fatigue: Volume I*, pages 81–97. ASTM International, West Conshohocken, PA, 1988.

J. Polák. The effect of intermediate annealing on the electrical resistivity and shear stress of fatigued copper. *Scripta Materialia*, 4(10):761–764, 1970.

J. Rickman und R. Lesar. Multipole expansion of dislocation interactions: application to discrete dislocations. *Physical Review B*, 65(14):144110, 2002.

C. Rycroft. Voro++: A three-dimensional Voronoi cell library in C++. Technical report, Lawrence Berkeley National Lab. (LBNL), Berkeley, CA (United States), 2009.

T. Sakai, M. Takeda, K. Shiozawa, Y. Ochi, M. Nakajima, T. Nakamura, und N. Oguma. Experimental reconfirmation of characteristic S-N property for high carbon chromium bearing steel in wide life region in rotating bending. *Journal of the Society of Materials Science, Japan*, 49(7):779–785, 2000.

M. Sauzay. Cubic elasticity and stress distribution at the free surface of polycrystals. *Acta Materialia*, 55(4):1193–1202, 2007.

M. Sauzay und J. Man. Influence of crystalline elasticity on the stress distribution at the free surface of an austenitic stainless steel polycrystal. Comparison with experiments. In *Materials Science Forum*, volume 567, pages 149–152. Trans Tech Publ, Switzerland, 2008.

M. Sauzay, P. Evrard, A. Steckmeyer, und E. Ferrié. Physically-based modeling of the cyclic macroscopic behaviour of metals. *Procedia Engineering*, 2(1):531–540, 2010.

K. Shiozawa und L. Lu. Very high-cycle fatigue behaviour of shot-peened high-carbon–chromium bearing steel. *Fatigue & Fracture of Engineering Materials & Structures*, 25(8-9):813–822, 2002.

K. Shiozawa, L. Lu, und S. Ishihara. S–N curve characteristics and subsurface crack initiation behaviour in ultra-long life fatigue of a high carbon-chromium bearing steel. *Fatigue & Fracture of Engineering Materials & Structures*, 24(12):781–790, 2001.

K. Shiozawa, Y. Morii, S. Nishino, und L. Lu. Subsurface crack initiation and propagation mechanism in high-strength steel in a very high cycle fatigue regime. *International Journal of Fatigue*, 28(11):1521–1532, 2006.

J. C. Simo und T. J. Hughes. *Computational Inelasticity*, volume 7. Springer Science & Business Media, New york, 2006.

K. Srivastava, R. Gröger, D. Weygand, und P. Gumbsch. Dislocation motion in tungsten: atomistic input to discrete dislocation simulations. *International Journal of Plasticity*, 47:126–142, 2013.

K. Srivastava, D. Weygand, und P. Gumbsch. Dislocation junctions as indicators of elementary slip planes in body-centered cubic metals. *Journal of Materials Science*, 49(20):7333–7337, 2014.

S. Stanzl-Tschegg, H. Mughrabi, und B. Schoenbauer. Life time and cyclic slip of copper in the vhcf regime. *International Journal of Fatigue*, 29(9-11):2050–2059, 2007.

R. I. Stephens, A. Fatemi, R. R. Stephens, und H. O. Fuchs. *Metal Fatigue in Engineering*. John Wiley & Sons, New York, 2000.

T. Straub. *Experimental Investigation of Crack Initiation in Face-Centered Cubic Materials in the High and Very High Cycle Fatigue Regime*. PhD thesis, KIT Scientific Publishing, Karlsruhe, 2016.

T. Straub, M. Berwind, T. Kennerknecht, Y. Lapusta, und C. Eberl. Small-scale multiaxial setup for damage detection into the very high cycle fatigue regime. *Experimental Mechanics*, 55(7):1285–1299, 2015.

M. Stricker, D. Weygand, und P. Gumbsch. Irreversibility of dislocation motion under cyclic loading due to strain gradients. *Scripta Materialia*, 129:69–73, 2017.

S. Suresh. *Fatigue of Materials*. Cambridge university press, Cambridge, 1998.

A. P. Sutton, R. W. Balluffi, und A. Sutton. *Interfaces in Crystalline Materials*. Clarendon Press Oxford, Oxford, 1995.

K. Tanaka und Y. Akiniwa. Fatigue crack propagation behaviour derived from S–N data in very high cycle regime. *Fatigue & Fracture of Engineering Materials & Structures*, 25(8-9):775–784, 2002.

K. Tanaka und T. Mura. A dislocation model for fatigue crack initiation. *Journal of Applied Mechanics*, 48(1):97–103, 1981.

N. Thompson, N. Wadsworth, und N. Louat. Xi. The origin of fatigue fracture in copper. *Philosophical Magazine*, 1(2):113–126, 1956.

E. Van der Giessen und A. Needleman. Discrete dislocation plasticity: a simple planar model. *Modelling and Simulation in Materials Science and Engineering*, 3 (5):689, 1995.

A. Vattré, B. Devincre, F. Feyel, R. Gatti, S. Groh, O. Jamond, und A. Roos. Modelling crystal plasticity by 3D dislocation dynamics and the finite element

method: the discrete-continuous model revisited. *Journal of the Mechanics and Physics of Solids*, 63:491–505, 2014.

V. Vitek. Core structure of screw dislocations in body-centred cubic metals: relation to symmetry and interatomic bonding. *Philosophical Magazine*, 84(3-5):415–428, 2004.

H. Wang und R. LeSar. O(N) algorithm for dislocation dynamics. *Philosophical Magazine A*, 71(1):149–164, 1995.

A. Weidner, D. Amberger, F. Pyczak, B. Schönbauer, S. Stanzl-Tschegg, und H. Mughrabi. Fatigue damage in copper polycrystals subjected to ultrahigh-cycle fatigue below the PSB threshold. *International Journal of Fatigue*, 32(6):872–878, 2010.

D. Weygand und P. Gumbsch. Study of dislocation reactions and rearrangements under different loading conditions. *Materials Science and Engineering: A*, 400: 158–161, 2005.

D. Weygand, L. Friedman, E. Van der Giessen, und A. Needleman. Discrete dislocation modeling in three-dimensional confined volumes. *Materials Science and Engineering: A*, 309:420–424, 2001.

D. Weygand, L. Friedman, E. Van der Giessen, und A. Needleman. Aspects of boundary-value problem solutions with three-dimensional dislocation dynamics. *Modelling and Simulation in Materials Science and Engineering*, 10(4):437, 2002.

L. Willertz. Ultrasonic fatigue. *International Metals Reviews*, 25(1):65–78, 1980.

H. Wilsdorf und J. Schmitz. The observation and interpretation of dislocation tangles in the easy glide range of aluminum. *Journal of Applied Physics*, 33(5):1750–1754, 1962.

A. Winter. The effect of work-hardening on the low strain amplitude fatigue of copper crystals. *Philosophical Magazine*, 31(2):411–417, 1975.

A. Winter. Dislocation structure in the interior of a fatigued copper polycrystal. *Acta Metallurgica*, 28(7):963–964, 1980.

A. Winter, O. Pedersen, und K. Rasmussen. Dislocation microstructures in fatigued copper polycrystals. *Acta Metallurgica*, 29(5):735–748, 1981.

A. Wöhler. *Über die Festigkeitsversuche mit Eisen und Stahl.* von Ernst und Korn, Berlin, 1870.

L. Xiao und Y. Umakoshi. Orientation dependence of cyclic deformation behavior and dislocation structure in Ti–5at.% Al single crystals. *Materials Science and Engineering: A*, 339(1):63–72, 2003.